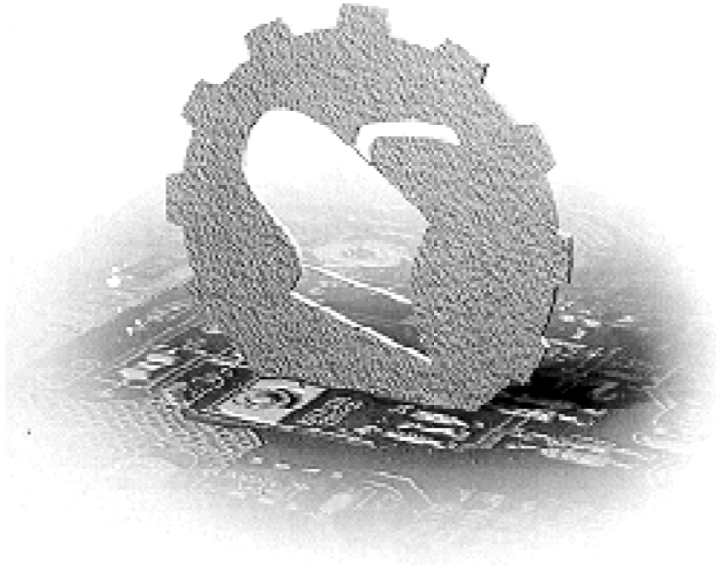


ISSN 0554-5587
UDK 631 (059)

ПОЉОПРИВРЕДНА ТЕХНИКА

AGRICULTURAL ENGINEERING

НАУЧНИ ЧАСОПИС
SCIENTIFIC JOURNAL



УНИВЕРЗИТЕТ У БЕОГРАДУ, ПОЉОПРИВРЕДНИ ФАКУЛТЕТ,
ИНСТИТУТ ЗА ПОЉОПРИВРЕДНУ ТЕХНИКУ
UNIVERSITY OF BELGRADE, FACULTY OF AGRICULTURE,
INSTITUTE OF AGRICULTURAL ENGINEERING



Година XXXVIII Број 3, 2013.
Year XXXVIII, No. 3, 2013.

Издавач (Publisher)

Универзитет у Београду, Пољопривредни факултет, Институт за пољопривредну технику,
Београд-Земун
University of Belgrade, Faculty of Agriculture, Institute of Agricultural Engineering, Belgrade-Zemun

Уредништво часописа (Editorial board)

Главни и одговорни уредник (Editor in Chief)

др Горан Тописировић, професор, Универзитет у Београду, Пољопривредни факултет

Уредници (National Editors)

др Ђукан Вукић, професор, Универзитет у Београду, Пољопривредни факултет
др Стева Божић, професор, Универзитет у Београду, Пољопривредни факултет
др Мирко Урошевић, професор, Универзитет у Београду, Пољопривредни факултет
др Мићо Ољача, професор, Универзитет у Београду, Пољопривредни факултет
др Анђелко Бајкин, професор, Универзитет у Новом Саду, Пољопривредни факултет
др Милан Мартинов, професор, Универзитет у Новом Саду, Факултет техничких наука
др Душан Радивојевић, професор, Универзитет у Београду, Пољопривредни факултет
др Драган Петровић, професор, Универзитет у Београду, Пољопривредни факултет
др Раде Радојевић, професор, Универзитет у Београду, Пољопривредни факултет
др Милован Живковић, професор, Универзитет у Београду, Пољопривредни факултет
др Зоран Милеуснић, професор, Универзитет у Београду, Пољопривредни факултет
др Рајко Миодраговић, доцент, Универзитет у Београду, Пољопривредни факултет
др Александра Димитријевић, доцент, Универзитет у Београду, Пољопривредни факултет
др Милош Пајић, доцент, Универзитет у Београду, Пољопривредни факултет
др Бранко Радичевић, доцент, Универзитет у Београду, Пољопривредни факултет
др Иван Златановић, доцент, Универзитет у Београду, Пољопривредни факултет
др Милан Вељић, професор, Универзитет у Београду, Машински факултет
др Драган Марковић, професор, Универзитет у Београду, Машински факултет
др Саша Бараћ, професор, Универзитет у Приштини, Пољопривредни факултет, Лешак
др Предраг Петровић, Институт "Кирило Савић", Београд
дипл. инг. Драган Милутиновић, ИМТ, Београд

Инострани уредници (International Editors)

Professor Peter Schulze Lammers, Ph.D., Institut für Landtechnik, Universität, Bonn, Germany

Professor László Magó, Ph.D., Szent Istvan University, Faculty of Mechanical Engineering, Gödöllő, Hungary

Professor Victor Ros, Ph.D., Technical University of Cluj-Napoca, Romania

Professor Sindir Kamil Okuyay, Ph.D., Ege University, Faculty of Agriculture, Bornova - Izmir, Turkey

Professor Stavros Vougioukas, Ph.D., Aristotle University of Thessaloniki

Professor Nicolay Mihailov, Ph.D., University of Rousse, Faculty of Electrical Engineering, Bulgaria

Professor Silvio Košutić, Ph.D., University of Zagreb, Faculty of Agriculture, Croatia

Professor Selim Škaljić, Ph.D., University of Sarajevo, Faculty of Agriculture, Bosnia and Herzegovina

Professor Dragi Tanevski, Ph.D., "Ss. Cyril and Methodius" University in Skopje, Faculty of Agriculture, Macedonia

Professor Zoran Dimitrovski, Ph.D., University "Goce Delčev", Faculty of Agriculture, Štip, Macedonia

Professor Sitaram D. Kulkarni, Ph.D., Agro Produce Processing Division, Central Institute of Agricultural Engineering, Bhopal, India

Контакт подаци уредништва (Contact)

11080 Београд-Земун, Немањина 6, тел. (011)2194-606, 2199-621, факс: 3163-317, 2193-659,
e-mail: gogi@agrif.bg.ac.rs, жиро рачун: 840-1872666-79.

11080 Belgrade-Zemun, str. Nemanjina No. 6, Tel. 2194-606, 2199-621, fax: 3163-317, 2193-659,
e-mail: gogi@agrif.bg.ac.rs, Account: 840-1872666-79

ПОЉОПРИВРЕДНА ТЕХНИКА

НАУЧНИ ЧАСОПИС

AGRICULTURAL ENGINEERING

SCIENTIFIC JOURNAL

УНИВЕРЗИТЕТ У БЕОГРАДУ, ПОЉОПРИВРЕДНИ ФАКУЛТЕТ,
ИНСТИТУТ ЗА ПОЉОПРИВРЕДНУ ТЕХНИКУ
UNIVERSITY OF BELGRADE, FACULTY OF AGRICULTURE,
INSTITUTE OF AGRICULTURAL ENGINEERING

WEB адреса

www.jageng.agrif.bg.ac.rs

Издавачки савет (*Editorial Council*)

Проф. др Властимир Новаковић, Проф. др Милан Тошић, Проф. др Петар Ненић,
Проф. др Марија Тодоровић, Проф. др Драгиша Раичевић, Проф. др Ђуро Ерцеговић,
Проф. др Ратко Николић, Проф. др Драгољуб Обрадовић, Проф. др Божидар Јачинац,
Проф. др Драган Рудић, Проф. др Милош Тешић

Техничка припрема (*Technical editor*)

Иван Спасојевић, Пољопривредни факултет, Београд

Лектура и коректура: (*Proofreader*)

Гордана Јовић

Превод: (*Translation*)

Весна Ивановић, Зорица Крејић, Миљенко Шкрлин

Штампа (*Printed by*)

"Академска издања" – Земун
Часопис излази четири пута годишње

Тираж (*Circulation*)

350 примерака

Претплата за 2014. годину износи 2000 динара за институције, 500 динара за појединце и 100 динара за студенте по сваком броју часописа.

Радови објављени у овом часопису индексирани су у базама (*Abstracting and Indexing*):

AGRIS i SCIndeks

Издавање часописа помогло (*Publication supported by*)

Министарство просвете и науке Републике Србије

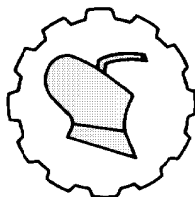
На основу мишљења Министарства за науку и технологију Републике Србије по решењу бр. 413-00-606/96-01 од 24. 12. 1996. године, часопис ПОЉОПРИВРЕДНА ТЕХНИКА је ослобођен плаћања пореза на промет робе на мало.

SADRŽAJ

OKSIDACIONI OTPOR PREMAZA NANETIH PLAZMA ELEKTROLITIČKOM OKSIDACIJOM NA LEGURAMA ALUMINIJUMA Yury Kuznetsov.....	1-9
OPTIMIZACIJA ELEKTRIČNIH PARAMETARA SILIKONSKIH HETERO-SPOJNIH SOLARNIH ČELIJA Veliyana Znelyazova, Krasimira Shtereva.....	11-18
UPOREDNA PROCENA PROIZVODNIH VARIJANTI UREĐAJA ZA PROIZVODNJU KONCENTROVANE STOČNE HRANE Prakash Prabhakar Ambalkar, Praveen Chandra Bargale, Jai Singh.....	19-26
MODEL EVAPORATIVNOG SISTEMA HLAĐENJA SKLADIŠNOG PROSTORA U TROPSKIM USLOVIMA Chinenye Ndukwu, Seth Manuwa, Olawale Olukunle, Babatunde Oluwalana.....	27-39
RAZVOJ KRIVIH SUŠE – POLOŽAJA – UČESTALOSTI U PARAMBIKULAM - ALIYAR BASENU, TAMIL NADU, INDIJA Muthiah Manikandan, Dhanapal Tamilmani.....	41-55
RAZVOJ VAZDUŠNOG RASPRSKIVAČA ZA ZAŠTITU CVEĆA U ZAŠTIĆENOM PROSTORU Sachin Vilas Wandkar, Shailendra Mohan Mathur, Babasaheb Sukhdeo Gholap, Pravin Prakash Jadhav.....	57-72
TEORIJSKO I EKSPERIMENTALNO ISTRAŽIVANJE JAČINE LEMLJENIH SPOJEVA (METAL METAL – METAL KERAMIKA) Vladimir Goncharenko.....	73-84
KINETIKA SUŠENJA TANKOG SLOJA LISTOVA KANE Dattatreya M. Kadam, Manoj Kumar Gupta, Vaijayanta M Kadam.....	85-100
STEPENI AERODINAMIKE I PROTOKA ČVRSTE MATERIJE U ODVODNIM KANALIMA ZA SUŠENJE KARDAMOMA (2. deo) Murugesan Balakrishnan, Velath Variyathodiyil Sreenarayanan, Ashutosh Singh, Gopu Raveendran Nair, Rangaraju Viswanathan, Grama Seetharama Iyengar, Vijaya Raghavan.....	101-110
ANALIZA KAPLJICA VODE: KLASIČNI I KVANTNI HIDRODINAMIČKI OKVIRI Daniele De Wrachien, Giulio Lorenzini, Stefano Mambretti, Marco Medici.....	111-122

CONTENTS

OXIDATION RESISTANCE OF THE COATINGS OBTAINED BY PLASMA ELECTROLYTIC OXIDATION ON ALUMINIUM ALLOYS Yury Kuznetsov.....	1-9
OPTIMIZATION OF THE ELECTRICAL PARAMETERS OF SILICON HETEROJUNCTION SOLAR CELLS Veliyana Znelyazova, Krasimira Shtereva.....	11-18
COMPARATIVE EVALUATION OF PRODUCTION VARIANTS OF ANIMAL FEED PLANT Prakash Prabhakar Ambalkar, Praveen Chandra Bargale, Jai Singh.....	19-26
A SIMPLE MODEL FOR EVAPORATIVE COOLING SYSTEM OF A STORAGE SPACE IN A TROPICAL CLIMATE Chinenye Ndukwu, Seth Manuwa, Olawale Olukunle, Babatunde Oluwalana.....	27-39
DEVELOPMENT of DROUGHT SEVERITY – AREAL EXTENT – FREQUENCY CURVES IN THE PARAMBIKULAM - ALIYAR BASIN, TAMIL NADU, INDIA Muthiah Manikandan, Dhanapal Tamilmani.....	41-55
DEVELOPMENT OF AIR ASSISTED SPRAYER FOR GREENHOUSE FLORICULTURE CROPS Sachin Vilas Wandkar, Shailendra Mohan Mathur, Babasaheb Sukhdeo Gholap, Pravin Prakash Jadhav.....	57-72
THEORETICAL AND EXPERIMENTAL RESEARCH OF STRENGTH OF SOLDERED JOINTS (METAL OF SHARE – METAL CERAMICS) Vladimir Goncharenko.....	73-84
THIN LAYER DRYING KINETICS OF HENNA LEAVES Dattatreya M. Kadam, Manoj Kumar Gupta, Vaijayanta M. Kadam.....	85-100
AERODYNAMIC AND SOLIDS CIRCULATION RATES IN SPOUTED BED DRYING OF CARDAMOM (Part 2) Murugesan Balakrishnan, Velath Variyathodiyil Sreenarayanan, Ashutosh Singh, Gopu Raveendran Nair, Rangaraju Viswanathan, Grama Seetharama Iyengar, Vijaya Raghavan.....	101-110
WATER DROPLETS ANALYSIS: THE CLASSICAL AND QUANTUM HYDRODYNAMIC FRAMEWORKS Daniele De Wrachien, Giulio Lorenzini, Stefano Mambretti, Marco Medici.....	111-122



UDK: 669.717:66.018:621.794.61:667.6

Originalni naučni rad
Original scientific paper

OXIDATION RESISTANCE OF THE COATINGS OBTAINED BY PLASMA ELECTROLYTIC OXIDATION ON ALUMINIUM ALLOYS

Yury Kuznetsov*

*Orel State Agrarian University,
Faculty of Agricultural Machinery and Power Supply,
Chair of Technology of Constructional Materials and Technical Service Organization,
Orel, Russian Federation*

Abstract: Plasma electrolytic oxidation (PEO) is one of the new methods of obtaining thin layer oxide ceramic coatings on machine elements of different purpose of use; that allows considerably increase their durability.

This paper outlines the results of experimental studies on corrosion resistance of oxide ceramic coatings formed by PEO on various aluminum alloys using KOH-H₃BO₃ electrolyte.

Corrosion tests of the samples were performed using the following two methods:

1. According to ASTM G44 “Standard Practice for Exposure of Metals and Alloys by Alternate Immersion in Neutral 3.5% Sodium Chloride Solution”,
2. Polarization tests.

Both tests of corrosion resistance of aluminum alloys clearly demonstrate that plasma electrolytic oxidation significantly improves corrosion resistance: depending on an alloy, corrosion rates of PEO coated samples are by the factor of 2.5-80 lower as compared with non-coated samples.

Key words: *oxide-ceramic coating, plasma-electrolytic oxidation, electrolyte, aluminum alloy, corrosion medium, pole curve.*

* Corresponding author. E-mail: kentury@rambler.ru, tkmiots@rambler.ru

INTRODUCTION

Plasma electrolytic oxidation (PEO) implies formation of coatings on the surface of conducting material in electrolyte in a high voltage mode to ensure local microplasma discharges traveling along the surface when the material is anodically polarized [1,2].

PEO is a multifactor-controlled process. The quality of PEO coating can be controlled by compositions of electrolyte and alloy, temperature of electrolyte, treatment time and voltage, anodic current density, and the ratio of cathode to anodic current density, etc. [3]. High quality coatings can be formed by suitable selection of deposition parameters.

This process has a lot of advantages over conventional methods, such as anodic treatment, electrophoresis, plasma and flame spraying, etc.

Among the major advantages of plasma electrolytic oxidation are: formation of oxide ceramic coatings with good physical and mechanical properties (such as hardness, wear and corrosion resistance, adhesion to metal substrate, fatigue resistance); minimization of production space and shorter technological process because no thorough preparation of item and structure surfaces is needed; safe to the environment.

MATERIALS AND METHODS

Al5251, Al1035, and Al2024 aluminum alloy plates (3 x 30 x 100 mm) (chemical composition is shown in Tab. 1.) with oxide ceramic coatings, as formed by PEO in electrolyte with the composition shown in Tab. 2, have been used as samples. Substrate plates were polished with #1200grit SiC abrasive paper before being coated by the PEO process. The oxidation was performed at the current density 10-30 $A \cdot dm^{-2}$ for 120 minutes on a home-made 40 kVA PEO station with a water-cooled bath made of stainless steel, which served as the counter electrode. General view of laboratory device for samples oxidation is presented in Fig. 1.

Table 1. Chemical Composition of Oxidized Alloys (% weight)

Alloys	Fe	Si	Mn	Cr	Ti	Cu	Mg	Zn
5251	0.5	0.4	0.1 - 0.5	0.15	0.15	0.15	1.7 - 2.4	0.15
1035	$\Sigma 0.7$		0.05	-	0.03	0.10	0.05	0.10
2024	0.5	0.5	0.3-0.9	0.1	0.15	3.8-4.9	1.2-2.8	0.25

Table 2. Electrolyte Composition for PEO Samples

Electrolyte Components	Concentration [g·l ⁻¹]
1. Sodium hydroxide, reagent grade, CAS 1310-73-2 (KOH)	5
2. Boric acid, reagent grade, CAS 10043-35-3 (H ₃ BO ₃)	20

pH of the electrolytes was measured by a YK-2005WA pH/CD meter (ASTM D1125 -95 (2009) Standard Test Methods for Electrical Conductivity and Resistivity of Water).



a.



b.

Figure 1. General view of developed device for PEO
a. electrolytic bath, b. power supply and control unit

Corrosion tests of the samples were performed using the following two methods:

1. According to ASTM G44 “Standard Practice for Exposure of Metals and Alloys by Alternate Immersion in Neutral 3.5% Sodium Chloride Solution”. This method is based on accelerated, as compared to a standard salt spray test according to ASTM B117, corrosion by cycles of sample immersion into a special electrolyte solution and consequent air drying [4].

For the performing of corrosion tests, a special test station consisting of a bath and an engine responsible for cyclic immersion and lifting of samples according to ASTM G44, was designed and constructed. Test samples were fixed vertically.

The salt solutions were prepared by dissolving 3.5 ± 0.1 weight parts of NaCl (reagent grade, CAS 7647-14-5) in 96.5 parts of water (distilled or deionized water, reagent grade, ASTM 1193, type IV). The volume of the electrolyte solution in the bath was regulated in such a manner that at least 32 ml of the electrolyte were taken per 1 cm^2 of the total surface area of a sample.

Total duration of tests was 240 hours, with the electrolyte temperature of 18-20°C. Samples have been immersed in the solution for 10 minutes and then dried on air for 50 minutes.

On completion of tests, samples were rinsed by a jet of tap water and then by distilled water. Solid corrosion products were removed from the surface by mechanical and chemical means which were not affecting evaluation of test results as per ASTM G44.

Corrosion parameters were assessed in terms of mass loss per unit of surface area ($\text{g}\cdot\text{m}^{-2}$) according to Eq. 1.

$$\Delta m = \frac{m_0 - m_1}{S_{no}} \quad (1)$$

where:

Δm [$\text{g}\cdot\text{m}^{-2}$] - mass loss per unit of surface area,

m_0 [g] - mass of the sample before tests,

m_1 [g] - mass of the sample after tests and removal of corrosion products,

S_{no} [m^2] - sample surface area.

Corrosion rate was determined according to Eq. 2.

$$K_{cor} = \frac{\Delta m}{t_{cor}}, \quad (2)$$

where:

K_{cor} [$\text{g}\cdot\text{m}^{-2}\cdot\text{year}^{-1}$] - corrosion rate,

t_{cor} [years] - test duration.

Experimental device presented in Fig. 2 is used for carrying out corrosion tests.

Samples were weighed on ViBRA AF-220E analytical balance.

2. Potentiodynamic polarization tests were performed on Autolab PGSTAT12

Potentiostat – Galvanostat controlled by General Purpose Electrochemical

System – GPES 4.9 software in a standard corrosion cell. Tests were performed according to ASTM G 59 Standard Test Method for Conducting Potentiodynamic Polarization Resistance.

The potentiodynamic polarization tests were carried out in 3.5 wt.% NaCl, and the solution was prepared using analytical grade reagents. A three-electrode cell with a specimen as a working electrode, saturated calomel electrode (SCE) as a reference electrode and stainless steel plate as a counter electrode was employed. Linear Sweep Voltammetry procedure was used for each specimen so that the sweeping rate was 1 mV/s and the scanning range was from about -250 mV to $+250 \text{ mV}$ vs. the open circuit potential. The tested area was 1 cm^2 , with the remaining surface masked by a lacquer. The Tafel Extension Method was used to measure corrosion current densities, corrosion potential and corrosion rates.

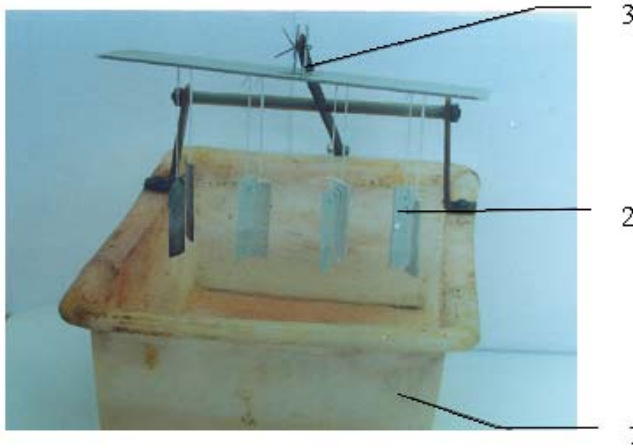


Figure 2. Experimental device for carrying out corrosion tests at intermittent immersion:
1. bath, 2. Samples, 3. balance

RESULTS AND DISCUSSION

Test results (Fig. 3, 4) confirm that corrosion parameters of micro-plasma treatment of aluminum alloys in $KOH-H_3BO_3$ electrolyte are directly depending on PEO mode and chemical composition of oxidized alloys. The higher current density, the higher is corrosion, which is attributed to higher porosity of coatings.

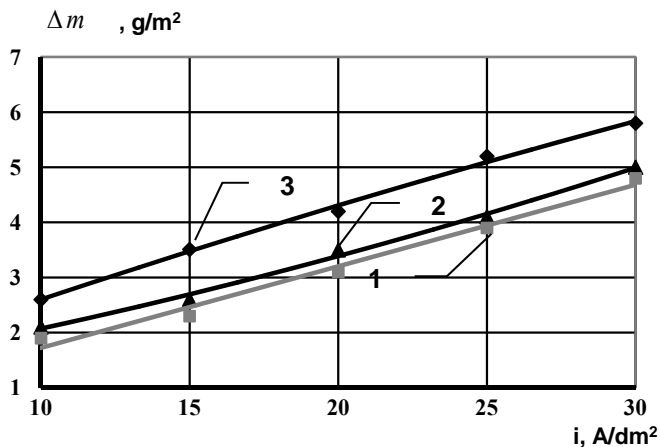


Figure 3. Mass loss Δm on current density i dependence
($t = 120$ min; $C_{KOH} = 5$ g·l⁻¹; $C_{H_3BO_3} = 25$ g·l⁻¹) in 3.5% NaCl corrosive medium.
Line 1 for Al5251 alloy, 2 for Al1035 alloy, 3 for Al2024 alloy

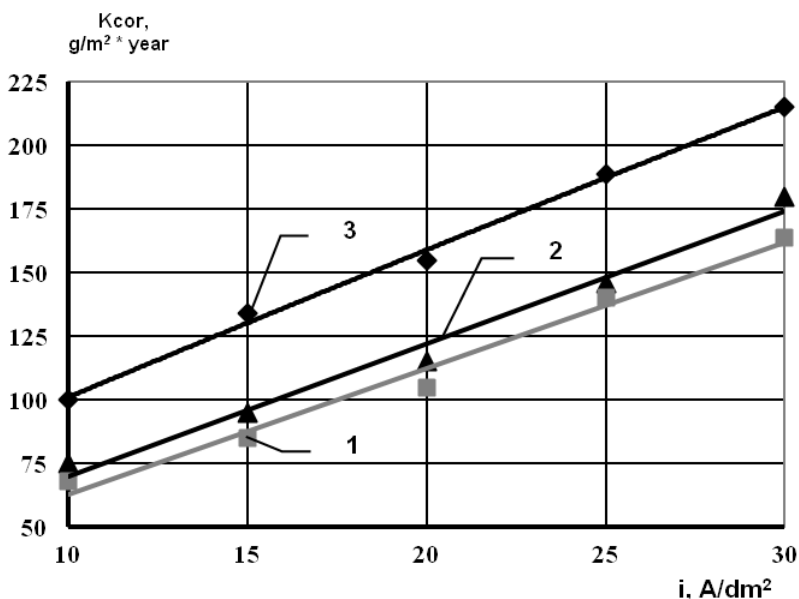


Figure 4. Corrosion rate K_{cor} vs. current density i dependence ($t = 120$ min; $CKOH = 5$ g·l⁻¹; $CH_3BO_3 = 25$ g·l⁻¹) in 3.5% NaCl corrosive medium. Line 1 for Al5251 alloy, 2 for Al1035 alloy, 3 for Al2024 alloy.

It deserves to be noted that pitting corrosion is observed for current densities of 10-20 A·dm⁻², while only corrosion spots are observed for 20-30 A·dm⁻². This should be attributed to corrosive medium penetrating through the pores to induce corrosion beneath the coating. Coatings are destroyed due to the presence of chlorine ions, since because of their small radius [5] they are capable of penetrating inside the coatings and destroy those. The interaction between the coating and corrosive medium results in adsorption of medium surfactants. Chlorine ions are capable of expelling oxygen out of crystalline Al₂O₃-containing coating, and the surface is therefore enriched with chlorine. Al2024 coatings are less corrosion resistant than those on Al5251 and Al1035. This is apparently due to the fact that the alloy contains copper which intensifies corrosion. Magnesium and silicon presence in oxidized alloys results in reduced number of through pores and reduced corrosion. This is attributed to formation of magnesium and silicon oxides with lower melting temperatures, as compared to aluminum oxide. Plasma electrolytic oxidation implies high temperatures, and magnesium and silicon oxides therefore more intensively melt and fill the pores, thereby improving protective properties.

Intensity of the study process can be judged by pH changes in the corrosive medium. Research results are shown in Fig. 5.

Sodium hydroxide is formed due to chemical interaction between the coating and corrosive medium, which results in higher pH of the medium.

Fig. 6 shows polarization curves of a non-coated sample and samples with ceramic coating of PEO.

The Tafel Extension Method was used to measure corrosion current densities, corrosion potential and corrosion speeds. Results are shown in Tab. 3 [6, 7].

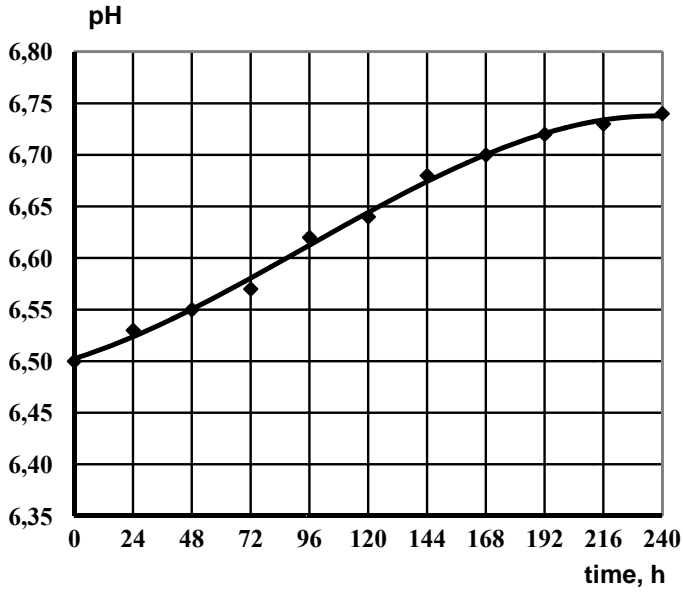


Figure 5. The change of pH in the course of corrosion tests

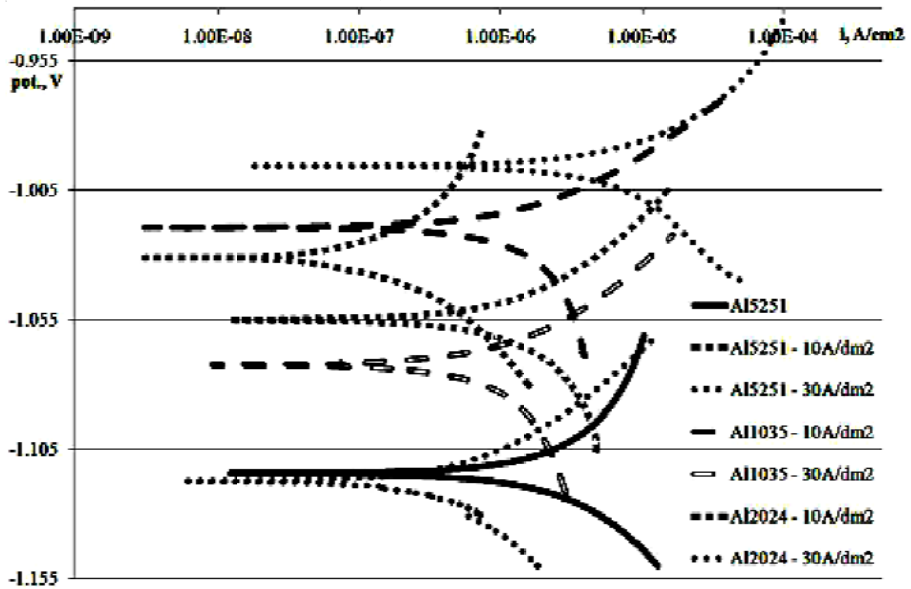


Figure 6. Polarization curves of a non-coated sample and samples with ceramic coating of PEO

Table 3. Corrosion measurement of alloys aluminum without and with PEO

	Unit	Al5251	Al1035		Al5251		Al2024	
		without PEO	10A·dm ⁻²	30A·dm ⁻²	10A·dm ⁻²	30A·dm ⁻²	10A·dm ⁻²	30A·dm ⁻²
Corrosion current densities	[μA·cm ⁻²]	15,99	2,66	1,68	0,93	0,98	3,77	4,30
Corrosion potential	[V]	-1,126	-1,015	-1,072	-1,042	-1,118	-1,055	-0,996
Polarization resistance	[kOhm]	0,145	2,059	0,355	0,4815	1,418	6,654	1,175
Corrosion speed	[μ/year]	230,0	2,9	3,0	9,5	14,8	48,5	89,1

CONCLUSION

Both tests of corrosion resistance of aluminum alloys clearly demonstrate that plasma electrolytic oxidation significantly improves corrosion resistance: depending on an alloy, corrosion rates of PEO coated samples are by the factor of 2.5-80 lower as compared with non-coated samples.

The higher current density, the higher is the porosity and the number of corroding cracks in the coating. Corrosion rate is linearly dependent on oxidation current density for all alloys studied. With the increasing content of non-oxidizable alloying ingredients (like copper in Al2024), coating contains more and more porous oxides with no protective properties. This is also associated with much lower corrosion resistance, as compared to dilute alloys.

BIBLIOGRAPHY

- [1] Malyshev, V.N., Zorin, K.M. 2007. Features of microarc oxidation coatings formation technology in slurry electrolytes. *Applied Surface Science* 254 (2007), p.p. 1511–1516.
- [2] Snizhko, L.O., Yerokhin, A.L., Pilkington, A., Gurevina, N.L., Misnyankin, D.O., Leyland, A., Matthews, A. 2004. Anodic processes in plasma electrolytic oxidation of aluminum in alkaline solutions. *Electrochimica Acta* 49 (2004), p.p. 2085–2095.
- [3] Krysmann, W., Kurze, P., Dittrich, H.G. 1984. Process characteristic and parameters of anodic oxidation by spark discharge. *Crystal. Res. Technol.* 19 (1984), p. 973.
- [4] *ASM Metal – Handbook*, volume 13 – Corrosion, manual, etc. I. ASM International. Handbook Committee, 1987, ISBN 0-87170-007-7.
- [5] Rosenfeld, I.L. 1970. *Korrozia i Zashita Metallov (Corrosion and Protection of Metals)* – M.: Metallurgia Publishing House, 1970, p. 237.
- [6] Kuznetsov, Y, Kossenko, A, Lugovskoy, A. 2011. Studies on corrosion resistance of coatings formed by plasma electrolytic oxidation on aluminum alloys. The optimization of the composition, structure and properties of metals, oxides, composites, nano and amorphous materials. *Tenth Israeli-Russian Bi-National Workshop 2011, Proceedings*. Jerusalem, Israel, 2011. (307), p.p. 297-303.

- [7] Kuznetsov, Y. Corrosion testings of coatings being obtained by plasma electrolytics-oxidation. *International Scientific Conference „Energy Efficiency and Agricultural Engineering“*. International Commission Of Agricultural Engineering (CIGR), European Society of Agricultural Engineers (EurAgEng), Association of Agricultural Engineering in Southeastern Europe (AAESEE), Bulgarian National Society of Agricultural Engineers (BAER). May 17-18, 2013, Ruse, Bulgaria. *Conference Proceedings*. ISSN 1311-9974, p.p. 554-559.

OKSIDACIONI OTPOR PREMAZA NANETIH PLAZMA ELEKTROLITIČKOM OKSIDACIJOM NA LEGURAMA ALUMINIJUMA

Yury Kuznetsov

*Državni Poljoprivredni Univerzitet Orel, Fakultet za poljoprivredne i pogonske mašine,
Katedra za tehnologiju konstruktivnih materijala i organizaciju tehničkog servisa,
Orel, Ruska Federacija*

Sažetak: Plazma elektrolitička oksidacija (PEO) je jedan od novih metoda za dobijanje oksidno keramičkih premaza u tankim slojevima na elementima mašina različite namene, što značajno produžava njihov vek trajanja.

U ovom radu su izneti rezultati eksperimentalnih istraživanja otpora na koroziju oksidno keramičkih premaza nanetih pomoću PEO na različite aluminijumske legure upotrebom elektrolita KOH-H₃BO₃.

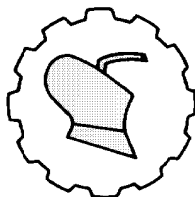
Testovi korozije na uzorcima su izvođeni upotrebom sledeće dve metode:

1. Prema ASTM G44 “Standardna praksa za izlaganje metala i legura alternativnim potapanjem u neutralni 3.5% rastvor natrijum hlorida”,
2. Testovi polarizacije.

Oba testa otpornosti na koroziju aluminijumskih legura jasno su pokazala da plazma elektrolitička oksidacija značajno poboljšava otpornost na koroziju: zavisno od legure, stepeni korozije PEO zaštićenih uzoraka su 2.5-80 puta niži u poređenju sa uzorcima bez premaza.

Ključne reči: *oksido-keramički premaz, plazma elektrolitička oksidacija, elektrolit, legura aluminijuma, korozivno sredstvo, polna kriva.*

Prijavljen: 13.06.2013.
Submitted:
Ispravljen: 17.06.2013.
Revised:
Prihvaćen: 18.07.2013.
Accepted:



UDK: 620.91

Originalni naučni rad
Original scientific paper

OPTIMIZATION OF THE ELECTRICAL PARAMETERS OF SILICON HETEROJUNCTION SOLAR CELLS

Veliyana Znelyazova, Krasimira Shtereva*

*University of Ruse, Faculty of Electrical Engineering and Automation,
Department of Electronics, Ruse, Bulgaria*

Abstract: We used the AFORS-HET simulation program for hetero-junction solar cells modeling to determine how the thickness and material properties of the n -, i -, and p -layers affect the electrical parameters and the device performance. Simulation studies have been carried out on hetero-junction (HJ) amorphous silicon (a-Si)/crystalline silicon (c-Si) solar cells and hetero-junction solar cells with intrinsic thin layer (HIT). The obtained maximum solar energy conversion efficiency is 22.68% for a-Si (n)/a-Si(i)/c-Si(p)/a-Si(p^+) solar cells with a back surface field (BSF) contact on a p -type silicon wafer. The open-circuit voltage (V_{OC}) (728.3 mV), short circuit current density (J_{SC}) (37.96 mA·cm⁻²), and the fill factor (FF) (82.06%) of the solar cells are improved by introducing thin layers of intrinsic and doped amorphous hydrogenated silicon, deposited on crystalline silicon, and by optimizing the thickness of the layers. Potential for achieving conversion efficiencies over 20% and current densities higher than 35 mA·cm⁻² are demonstrated.

Key words: modeling, simulation, hetero-junction solar cell, efficiency.

INTRODUCTION

During the last two decades the solar photovoltaic (PV) industry has shown an extraordinary growth, with an average growth rates exceeding 40% per year [1]. The global PV installed capacities of 102 GW at the end of 2012 are expected to exceed 1.5 TWp in 2030 [2,11].

* Corresponding author. E-mail: KShtereva@ecs.uni-ruse.bg

The wafer-based silicon technology maintains its leading position and the highest market share of around 80%, because of: (i) the technology maturity, which provides a reliable product with commercial module efficiencies ranging from 12 to 20%, and (ii) the existing manufacturing capacities [1,3].

The new generation thin film PV technologies have emerged as a response to the shortage of silicon feedstock and in order to reduce the material use per Wp. Their market share increased more than 3 times (from 6% to 16-20%) for the period from 2005 through 2010 [1]. The research efforts have been focused on the development of the solar cells based on hydrogenised amorphous silicon (a-Si:H), copper indium gallium diselenide (CIGS) and cadmium telluride (CdTe). Among the advantages of these technologies are the usage of less material, a monolithically integrated cell, lower cost and large area. However, the reported module efficiency (η) of a-Si (6÷10%), CdTe (10.9%) and CIGS (9.5%), are lower than those of crystalline silicon (c-Si) modules [3-5]. Silicon hetero-junction solar cells (SHJ) and hetero-junction solar cells with intrinsic thin layer (HIT), are a promising hybrid amorphous silicon (a-Si)/crystalline silicon (c-Si) technology developed by Sanyo. As a response to rapidly growing demand, the company increased the production capacity of HIT solar cells more than 3 times for the period from 2006 through 2010, to 600 MW [6]. The HIT solar cells became very attractive due to a unique conversion efficiency (higher than 22% in laboratory cells and 20% in commercially produced cells) combined with a low temperature device processing [7,12]. Compared to conventional diffused solar cells, HIT solar cells have a higher open-circuit voltage (V_{OC}) and a better temperature coefficient due to the reduced carrier recombination at the interface.

Numerical simulations are an important tool for gaining a better insight in material properties and processes in solar cells and hence, for the improvement of the devices. The large numbers of variables that influence the solar cell performance, such as the thickness of the layers and their physical parameters (density of states, a band gap, carrier concentration and mobilities) make it difficult, and economically ineffective to evaluate experimentally the effects of each variable on the cells characteristics. We have employed the numerical program, AFORS-HET v.2.4.1 to investigate the influence of the structure and the material parameters on the solar cell performance. Our previous research showed that an efficiency of 21.63% can be obtained by optimizing of the n -emitter layer thickness of the hetero-junction a-Si/c-Si solar cell [8].

In this paper, we present the numerical simulation study of hetero-junction cells (a-Si(n)/c-Si(p)), hetero-junction cells with intrinsic thin layer (a-Si(n)/a-Si(i)/c-Si(p)) and hetero-junction cells with intrinsic thin layer and back surface field (BSF) layer (a-Si(n)/a-Si(i)/c-Si(p)/a-Si(p^+)), using the software AFORS-HET. The simulations were used to optimize the thickness of the n -, i -, and p -layers and thereby to increase the solar cells efficiency.

MATERIAL AND NUMERICAL SIMULATION METHODOLOGY

Solar Cell Structures

Numerical simulation of a-Si/c-Si hetero-junction solar cells was carried out by AFORS-HET, version 2.4.1, computer software with the aim to investigate the effects of

the layers' thickness on the solar cell performance. In this work we investigated three types of hetero-junction solar cell structures, shown in Fig. 1. In Fig. 1(a) is shown a simple hetero-junction structure consisting of a transparent conducting ZnO layer used as a front contact, an n -type amorphous silicon layer deposited on a p -type crystalline silicon wafer and a metal back contact.

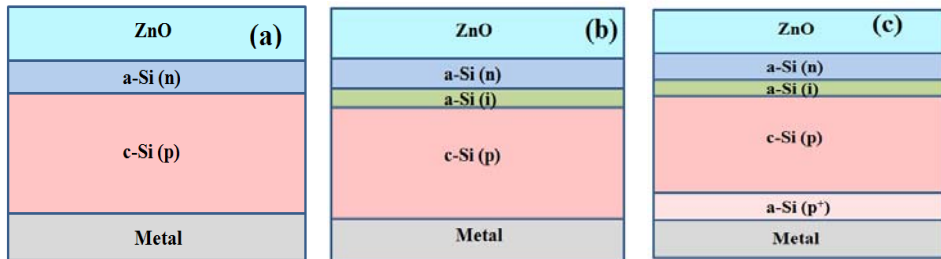


Figure 1. Structures of the simulated cells (a) a HJ a-Si(n)/c-Si(p) solar cell; (b) a HIT a-Si(n)/a-Si(i)/c-Si(p) solar cell, and (c) a HIT with BSF a-Si(n)/a-Si(i)/c-Si(p)/a-Si(p⁺) solar cell

The hetero-junction structure with an intrinsic layer is obtained when an intrinsic a-Si layer is inserted at the n/p interface (Fig. 1(b)). By inserting of this layer, the defects on the c-Si surface can be effectively passivated, and a high V_{oc} can be obtained. Fig. 1(c) represents a hetero-junction solar cell with a back surface field (BSF).

AFORS-HET is a numerical simulation tool, which can be used for modeling of homo-junction and hetero-junction photovoltaic devices. The software uses Shockley-Read-Hall recombination statistics to solve the one dimensional semiconductor equations for: (a) thermodynamic equilibrium (b) for steady-state conditions under an external applied voltage or current and/or illumination; (c) for small additional sinusoidal modulations of the external applied voltage/illumination; and (4) for transient conditions [13,14].

The simulations were performed under illumination at solar AM1.5 radiation with a power density of 1000W/m^2 . The flat band front and back contacts are chosen to ignore the contact potential influence. Band-to-band and Auger recombination are considered. The band gap was set to 1.7 eV for all the a-Si layers in the cell. In table 1 are listed parameters of the solar cells used for the simulations with the AFORS-HET such as, thickness, conduction and valence band density of states, doping concentrations and electron and hole mobilities.

The variable parameter for numerical simulations was the thickness of the n -, i -, or p -layers. The changes in V_{oc} , J_{sc} , FF and efficiency η were obtained and recorded.

RESULTS AND DISCUSSION

The optimum thickness of an n -type a-Si emitter layer was obtained at constant thicknesses of 3 nm, 300 μm and 5 nm of the a-Si (i), c-Si (p) and a-Si (p^+) layers respectively. Fig. 2 shows V_{oc} , J_{sc} , FF and the efficiency plotted as a function of the n -emitter (a-Si) layer thickness.

Maximum values of V_{oc} , J_{sc} and efficiency were obtained for a thickness of the n -type a-Si layer of 5 nm for all studied cells.

The open circuit voltage, short circuit current density, fill factor and efficiency as a function of the n -type a-Si layer thickness for a hetero-junction a-Si(n)/c-Si(p) solar cell are plotted in Fig.2(a). For thicknesses up to 12 nm V_{oc} remains constant (627.9 mV) and after that decreases to 626.4 mV.

Table 1. Material parameters used for the simulations with AFORS-HET

Parameter	Unit	c-Si(p)	a-Si(p)	a-Si(i)	a-Si(n)
Thickness	[nm]	variable	variable	variable	variable
Dielectric constant	-	11.9	11.9	11.9	11.9
Electron affinity	[eV]	4.05	3.9	3.9	3.9
Band gap	[eV]	1.12	1.72	1.72	1.72
Effective conduction band density	[cm^{-3}]	$2.8 \cdot 10^{19}$	10^{20}	10^{20}	10^{20}
Effective valence band density	[cm^{-3}]	$2.7 \cdot 10^{19}$	10^{20}	10^{20}	10^{20}
Electron mobility	[$cm^2 \cdot V^{-1} s^{-1}$]	1041	20	20	20
Hole mobility	[$cm^2 \cdot V^{-1} s^{-1}$]	413	5	5	5
Acceptor concentration	[cm^{-3}]	$1.5 \cdot 10^{16}$	$9 \cdot 10^{19}$	0	0
Donor concentration	[cm^{-3}]	0	0	1000	$5 \cdot 10^{19}$
Thermal velocity of electrons	[$cm \cdot s^{-1}$]	10^7	10^7	10^6	10^7
Thermal velocity of holes	[$cm \cdot s^{-1}$]	10^7	10^7	10^6	10^7
Layer density	[$g \cdot cm^{-3}$]	2.328	2.328	2.328	2.328
Auger recombination coefficient for electron	[$cm^6 s^{-1}$]	$2.2 \cdot 10^{-31}$	0	0	0
Auger recombination coefficient for hole	[$cm^6 s^{-1}$]	$9.3 \cdot 10^{-32}$	0	0	0
Direct band-to-band recombination coefficient	[$cm^3 s^{-1}$]	0	0	0	0

The increase of the layer thickness causes the decrease in J_{sc} ($35.6 \div 33.56 \text{ mA} \cdot \text{cm}^{-2}$) and consequently, the reduction of the cell efficiency from 18.52 to 17.3% due to the increase photons absorption in the thicker layer. The FF reduces from 82.88 to 82.32%.

For the HIT solar cell from Fig.1(b) the optimum n -layer thickness of 5 nm resulted in the highest V_{oc} , J_{sc} and efficiency of 629.4 mV, $36.01 \text{ mA} \cdot \text{cm}^{-2}$ and 18.69% respectively (Fig. 2(b)). As can be seen, the open circuit voltage decreases to 626.4 mV with increasing of the n -layer thickness above 13 nm. First, the fill factor raises slightly ($82.48 \div 82.58\%$ with the increasing n -layer thickness from 5 to 6 nm then decreases (82.04%) for the thickness range 6–13 nm.

Maximum V_{oc} of 723.8 mV, J_{sc} of $38.25 \text{ mA} \cdot \text{cm}^{-2}$ and a conversion efficiency of 21.34% were obtained for a HIT solar cell with a BSF layer, which consists of 5 nm a-Si(n), 3 nm a-Si(i), $300 \mu\text{m}$ c-Si(p) and 5 nm a-Si(p^+). V_{oc} , J_{sc} , FF and the efficiency dependence on the n -layer thickness is displayed in Fig. 2(c).

The obtained optimum thickness of the n -type a-Si layer of 5 nm for the simulated solar cell structures is in good agreement with the findings of other groups [9,10].

As in case of the n -type a-Si layer, the optimum thickness of 3 nm of the front i -type a-Si layer was found to be one and the same for all solar cells from Fig. 1. The simulations were performed at constant thicknesses of 5 nm, $300 \mu\text{m}$ and 5 nm of the a-Si (n), c-Si (p) and a-Si (p^+) layers respectively.

The optimum thickness of the *p*-type c-Si wafer varies, depending on the solar cell structure. Maximum conversion efficiency of 22.68% (*V*_{oc} of 728.3 mV, *J*_{sc} of 37.25 mA·cm⁻² and FF of 82.06%) were obtained for a HIT solar cell with a BSF layer and a wafer thickness of 250 μm.

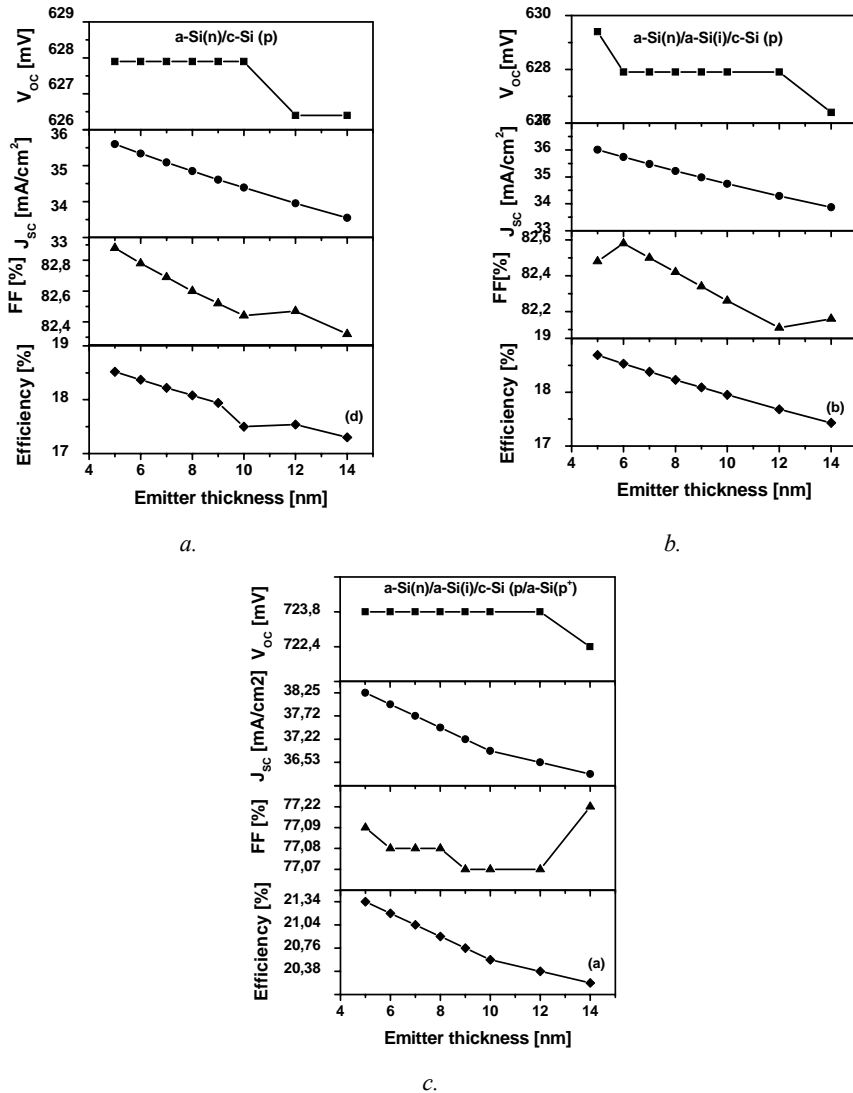


Figure 2. Dependence of V_{oc} , J_{sc} , FF and efficiency on the *n*-emitter layer thickness for: a. a HJ a-Si(n)/c-Si(p) solar cell; b. a HIT a-Si(n)/a-Si(i)/c-Si(p) solar cell; c. a HIT with BSF a-Si(n)/a-Si(i)/c-Si(p)/a-Si(p⁺) solar cell

The conversion efficiency as a function of the thickness of the *p*-type c-Si wafer for a HJ a-Si(n)/c-Si(p) solar cell, a HIT a-Si(n)/a-Si(i)/c-Si(p) solar cell, and a HIT with BSF

a-Si(n)/a-Si(i)/c-Si(p)/a-Si(p⁺) solar cell is plotted in Fig. 3(a). In Fig 3(b) are displayed plots of V_{OC} as a function of the thickness of the p -type c-Si wafer for three solar cell structures.

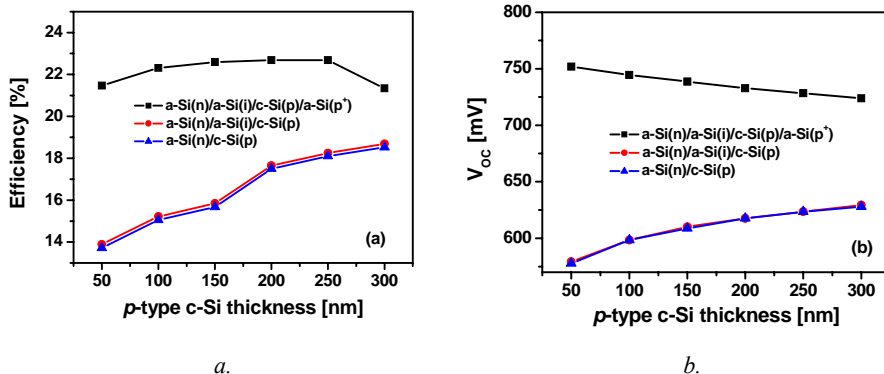


Figure 3. a. Conversion efficiency as a function of the thickness of the p -type c-Si wafer
b. Open circuit voltage V_{OC} as a function of the thickness of the p -type c-Si wafer

Although, the surface defects can be passivated by the deposition of a thin (3 nm) i -type layer on the front side of the c-Si wafer, it does not have a significant impact on the cell parameters (Fig. 3). On contrary, the deposition of a BSF layer strongly affected these parameters (Fig. 3). Some authors [10] attributed the influence of the p^+ -type BSF layer on the solar cell parameters to the formation of a barrier for the opposite polarity charge carriers.

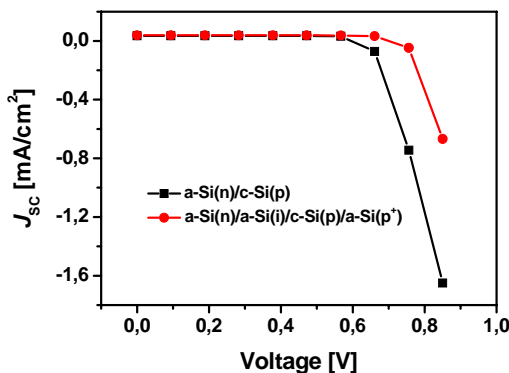


Figure 4. Current-voltage characteristics of a HJ a-Si(n)/c-Si(p) solar cell and a HIT a-Si(n)/a-Si(i)/c-Si(p)/a-Si(p⁺) solar cell with a BSF layer

A plot of the short circuit current density as a function of the applied voltage is shown in Fig. 4 for two solar cells with optimized thicknesses of the layers building the structure, a HJ a-Si(n)/c-Si(p) solar cell and a HIT a-Si(n)/a-Si(i)/c-Si(p)/a-Si(p⁺) solar cell with a BSF layer. It is obvious that the introduction of the p^+ -type BSF layer improves the solar cell characteristics, resulting in higher values of V_{oc} , J_{sc} , FF and the efficiency.

CONCLUSIONS

The AFORS-HET program was utilized for optimizing the thickness of the n -, i - and p -layers of a simple HJ solar cell (a-Si(n)/c-Si(p)), a HIT solar cell (a-Si(n)/a-Si(i)/c-Si(p)), and a HIT solar cell with BSF (a-Si(n)/a-Si(i)/c-Si(p)/a-Si(p^+)) toward the aim to improve the device performance and to obtain a high efficiency solar cell.

The obtained optimum thicknesses of the n -type a-Si layer (5 nm) and of the i -type a-Si layer (3 nm) were found to be one and the same for all studied solar cells. The optimum thickness of the p -type c-Si wafer varies, depending on the solar cell structure. Maximum conversion efficiency of 22.68% (V_{oc} of 728.3 mV, J_{sc} of 37.25 mA·cm⁻² and FF of 82.06%) were obtained for a HIT solar cell with a BSF layer and a wafer thickness of 250 μ m.

It was found that although the surface defects can be passivated by the deposition of a 3 nm i -type layer on the front side of the c-Si wafer, it does not have a significant impact on the cell parameters. On contrary, the deposition of a BSF layer strongly affected these parameters due to maybe, the formation of a barrier for the opposite polarity charge carriers. The introduction of the p^+ -type BSF layer improves the solar cell characteristics, resulting in higher values of V_{oc} , J_{sc} , FF and the efficiency.

BIBLIOGRAPHY

- [1] Jager-Waldau, A. 2011. Quo Vadis photovoltaics, *EPJ Photovoltaics*, 2, 20801, 1-10.
- [2] Delbos, S. 2012. Kesterite thin films for photovoltaics: a review. *EPJ Photovoltaics* 3, 35004, 1-13.
- [3] Green, M.A., Emery, K., Hishikawa, Y., Warta, W. 2009. Solar Cell Efficiency Tables (Version 33). *Progress in Photovoltaics: Research and Application*, 17, 85–94.
- [4] Radue, C., Dyk, E.E. 2007. Pre-deployment evaluation of amorphous silicon photovoltaic modules. *Solar Energy Materials & Solar Cells*, 91, 129–136.
- [5] Shah, A., Meier, J., Buechel, A., Kroll, U., Steinhauser, J., Meillaud, F., Schade, H., Dominé, D. 2006. Towards very low-cost mass production of thin-film silicon photovoltaic (PV) solar modules on glass. *Thin Solid Films*, 502, 292 – 299.
- [6] Tsunomura, Y., Yoshimine, Y., Taguchi, M., Baba, T., Kinoshita, T., Kanno, H., Sakata, H., Maruyama, E., Tanaka, M. 2009. Twenty-two percent efficiency HITsolar cell. *Solar Energy Materials & Solar Cells*, 93, 670–673.
- [7] Como, N. H., Acevedo, A. M. 2010. Simulation of hetero-junction silicon solar cells with AMPS-1D. *Solar Energy Materials & Solar Cells*, 94, 62–67.
- [8] Zhelyiyazova, V., Shtereva, K. 2013. Optimization of the Parameters of Solar Cells through Numerical Simulations, *Proceedings of 5th conference on Energy Efficiency and Agricultural Engineering*, 17-18 May 2013, Ruse, Bulgaria, 488-495.
- [9] Schmidt, M., Korte, L., Laades, A., Stangl, R., Schubert, Ch., Angermann, H., Conrad, E., Maydell, K. 2007. Physical aspects of a-Si:H/c-Si hetero-junction solar cells. *Thin Solid Films*, 515, 7475–7480.
- [10] Dwivedi, N., Kumar, S., Bisht, A., Patel, K., Sudhakar, S. 2013. Simulation approach for optimization of device structure and thickness of HIT solar cells to achieve ~27% efficiency. *Solar Energy*, 88, 31–41.
- [11] European Photovoltaic Industry Association, Global Market Outlook for Photovoltaics 2013-2017. 2013. Available through: <http://www.epia.org/news/publications/> [6 May 2013].

- [12] Levi, D., Iwaniczko, E., Page, M., Wang, Q., Branz, H., Wang, T. 2006. Silicon Heterojunction Solar Cell Characterization and Optimization Using *In Situ* and *Ex Situ* Spectroscopic Ellipsometry "Preprint". 2006. Conference Paper NREL/CP-520-39932. Available through: www.nrel.gov/docs/fy06osti/39932.pdf [14 April 2013].
- [13] Stangl, R., Geipel, T., Dubiel, M., Kriegel, M., El-Shater, Th., Lips, K. AFORS-HET 3.0: First Approach to a Two-Dimensional Simulation of Solar Cells. Available through: dubielnet.de/max/BachelorThesis/aforshtpaper.pdf [12 March 2013]
- [14] Froitzheim, A., R. Stangl, L. Elstner, M. Kriegel, W. Fuhs, AFORS-HET: A Computer-Program for the Simulation of Heterojunction Solar Cells to be Distributed for Public Use. Available through: www.helmholtz-berlin.de/media/media/...HET/...het/published1.pdf. [12 March 2013].

OPTIMIZACIJA ELEKTRIČNIH PARAMETARA SILIKONSKIH HETERO-SPOJNIH SOLARNIH ČELIJA

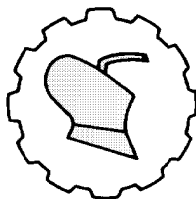
Veliyana Zneliyazova, Krasimira Shtereva

*Univerzitet Ruse, Fakultet za elektrotehniku i automatizaciju,
Institut za elektroniku, Ruse, Bugarska*

Sažetak: Program za simulaciju AFORS-HET za modeliranje hetero-spojnih solarnih ćelija upotrebljen je za određivanje uticaja debljine i karakteristika materijala n -, i -, i p -slojeva na električne parametre i karakteristike uređaja. Simulacije su izvođene na hetero-spojnim (HJ) solarnim ćelijama od amorfno silikona (a-Si)/kristalnog silikona (c-Si) i hetero-spojnim solarnim ćelijama sa intrinzičnim slojem (HIT). Postignuta je maksimalna efikasnost konverzije sunčeve energije od 22.68% za a-Si (n)/a-Si(i)/c-Si(p)/a-Si(p^+) solarne ćelije sa zadnjim površinskim (BSF) kontaktom na p -tipu silikonske obloge. Napon otvorenog kola od (V_{OC}) (728.3 mV), gustina struje kratkog kola (J_{SC}) ($37.96 \text{ mA} \cdot \text{cm}^{-2}$) i faktor punjenja (FF) (82.06%) solarnih ćelija su unapređeni uvođenjem tankih slojeva intrinzičnog i obogaćenog amorfno hidrogenizovanog silikona, deponovanog na kristalnom silikonu i optimizacijom debljine slojeva. Predstavljen je potencijal za postizanje efikasnosti konverzije veće od 20% i gustine struje veće od $35 \text{ mA} \cdot \text{cm}^{-2}$.

Ključne reči: modeliranje, simulacija, hetero-spojna solarna ćelija, efikasnost.

Prijavljen: 13.06.2013.
Submitted:
Ispravljen:
Revised:
Prihvaćen: 24.07.2013.
Accepted:



UDK: 631.3

Originalni naučni rad
Original scientific paper

COMPARATIVE EVALUATION OF PRODUCTION VARIANTS OF ANIMAL FEED PLANT

Prakash Prabhakar Ambalkar^{*}, Praveen Chandra Bargale, Jai Singh

*Central Institute of Agricultural Engineering, Technology Transfer Division,
Bhopal, MP, India*

Abstract: A pelletized feed production unit to cater the need of nutritionally balanced, optimally processed, cost and time effective availability of feed for livestock/aqua farming may be adapted as a potential business enterprise. The feed pellet manufacturing technology may be commercialized through modular design and development of feed production unit accordingly established at *CIAE*, Bhopal. The reason for wanting to achieve such an objective is to warrant investment made in establishment of feed manufacturing unit. The feed production economy is analyzed the justification of manufacturing of feed production volume by acceptance of profitable idea through determination of economic variables on production variant such as working capital (₹), breakeven point (month), payback period (*a*), benefit cost ratio and internal rate of return (*IRR* in per cent). Four different pelletized feed production variants were evaluated, variant No. 01 and 02 are specifically designed for multicultural feed requirement under mixed / integrated farming (livestock-crop-fish) combination and variant 03 and 04 for solely dairy feed requirements have been taken into consideration. All these 04 production variants have been presented as economically viable enterprise for appropriate selection on capacity utilization and marketability of the finished feed.

Key words: *livestock-aqua feed, feed production variants, capacity utilization, economic variability parameters, comparative evaluation and INR.*

^{*} Corresponding author. E-mail: ppa_65@yahoo.co.in

INTRODUCTION

Farmers now realized maintaining of quality animals with appropriate feeding is vital to meet increased domestic and export demand of livestock / aqua products. The proportion of crossbred / improved breeds of animals has necessitated higher demand for nutritionally balanced and optimally processed feed. The kind of quality feed availability at cost and time effective scale would be the pre-requisite for sustainability of livestock and aquaculture enterprises in the region.

Further, to ensure quality and time effective feed production, the primary goal is to be very particular into the production and marketability aspects. Hence, the primary objective of feed formulation, processing and production is to provide livestock breeds and fish in particular with quality feed having sufficient nutritional balance, efficacy, digestibility, palatability, acceptability, storability, handling and ease of transport [6].

In this regard, an aqua (multipurpose) feed production pilot plant has been established at Central Institute of Agricultural Engineering, Bhopal, India producing aqua, poultry and cattle processed feed. The scope of the *CIAE* livestock-aqua feed pilot plant had been further augmented in view of harnessing potential demand of multicultural activities (livestock-crop-fish) combination for production of feed for aquatic, avian / ovine and bovine farming [7].

Therefore, the plant is considered to be the best fit design for promotion and development of integrated farming (agriculture-animal husbandry-aquaculture-rural industries) activities. In this paper, under the comparative evaluation of feed plant variants, the variant No.01 is considered as *CIAE* livestock-aqua feed production unit [1].

However, other feed production variant, such as variant No. 02 or other may be opted on the basis of scale-up and downsizing of *CIAE*, Bhopal feed plant respectively for facilitating and encouraging multicultural (integrated agricultural-animal husbandry-aquaculture) activities. However, in many regions within the country and outside, wherein only dairy enterprise is feasible due to socio-economic impact [5], the exclusive establishment of dairy feed production unit is found to be better judgmental from sustainability and profitability view point for all stakeholders.

Consequent upon, exclusive installation of dairy feed production unit, elimination of some of the unit operation machinery and its accessories (viz. water container for steam, water supply arrangement for steam generation, steam generator, water softener, steam conditioner, steam valve and steam supply line, hot water jacket in paddle mixer conveyor unit, pellet crumbler unit and small configuration pellet dies for pellet diameter varies from 3-4 mm) would result in substantial cost reduction on dairy feed production. The basis for selection of particular feed production plant design is required to be finalized both on techno-economic feasibility scale as well as on socio and ecological parameters [4] if scale of benefit is to be visualized.

MATERIAL AND METHODS

It is based on demand forecasting analysis dairy and poultry, dairy and aquaculture as well as dairy, poultry and aquaculture (integrated farming) the feed production variant No.1 and No.2 may be installed and commissioned. Further, dairy alone is also one of

the activities, in which India has the distinction of evolving new technologies on one hand and successfully adapting the promising technologies on the other. Hence, dairy has enough potential to initiate feed production unit establishment at the cottage or small level of enterprise [2]. Therefore, solely for catering pelletized feed requirement for dairy enterprise variant No. 03 or 04 may be opted (Table 1).

Table 1. Various types of multipurpose/ sole feed production variants

S.No.	Type of feed production variant	Gross price (million, ₹)
01	CLAE multipurpose feed production plant	1.087
02	Scale-up multipurpose feed plant	2.5
03	Minimum economic size production unit solely for dairy	0.8
04	Scale-up economic size production unit solely for dairy	1.5

The following have been the assumptions (Tab. 2) considered for the economic viability analysis [3] of the four commercial feed production plant variants, may be proposed as adaptable business ventures Feed plant produces relatively homogeneous feed, hence its capacity can be measured in number of units of output per unit of time as feed produced in $q \cdot h^{-1}$ can be set as a standard example for design and development of variants of feed production plant.

Table 2. Assumptions of production variants under economic viability analysis

Sr No	Particulars of Assumptions	Variant 01	Variant 02	Variant 03	Variant 04
1	Initial Cost of feed plant (₹)	1.087.000	2.500.000	800.000	1.500.000
2	Estimated life of feed plant	12	14	12	14
3	Production capacity ($q \cdot h^{-1}$)	1	10	1	2
4	Operation of feed plant ($h \cdot d^{-1}$)	16	8	16	10
5	Annual plant operation days (d)	300	150	300	300
6	Direct labour cost (₹)	10.000	18.000	10.000	15.000
7	Cost on shed construction (₹)	150.000	250.000	150.000	200.000
8	Raw material cost (₹)	11.440	60.000	11.440	14.300
9	Miscellaneous LS charges (₹)	60.000	75.000	50.000	72.000
10	Price of feed (₹ $\cdot d^{-1}$)	1.000	1.000	1.000	1.000
11	Fixed cost on per q feed (₹)	94,3	59,2	101,9	90,9
12	Variable cost per q feed (₹)	744	755,8	744	738,2
13	Total cost on production /q (₹)	838,3	815	845,9	829,1
14	Contribution (₹)	256	244,2	256	261,8

RESULTS AND DISCUSSION

References in the Tab. 3, Tab. 4 and Fig. 1 have been produced on account of completion of economic analysis of capacity utilization and capital expenditure for different feed production variants by taking into consideration the parameters assumed under Tab. 2.

Table 3 Parameters of Financial Viability of Feed Plant

Variant Sr. No.	Initial Cost (₹ million)	Working Capital (₹ million /a)	Profitability Index (Benefit Cost Ratio)	Break Even Point (month)	Pay Back Period (a)	IRR (%)
1	1,087	1,0296	1,193	4,42	3,04	27,75
2	2,5	2,65	1,227	2,90	2,53	30,98
3	0,8	0,85	1,182	4,77	3,79	29,11
4	1,5	1,875	1,206	4,17	3,61	23,37

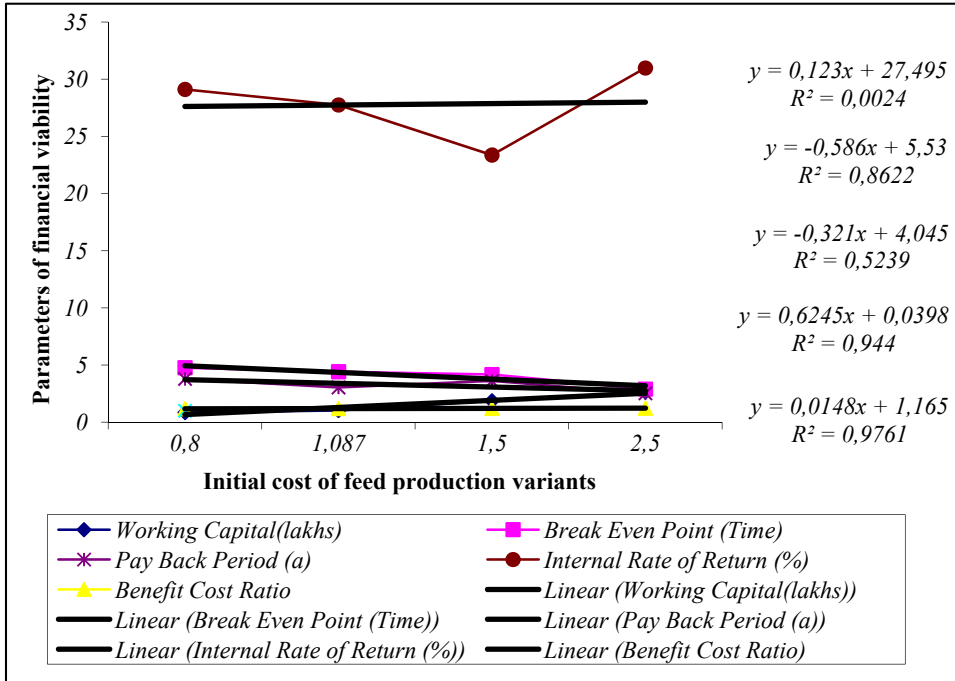


Fig. 1 Initial costs versus other economic parameters

Table 4 Relationship of Independent Vs Response (dependent) Variables

Sr. No.	Initial Investment Vs. economic parameters	Deviation	Coefficient of Correlation (r)	Regression Equations
1	Working Capital (Rs lakhs)	$R^2=0.9400$	0,970	$Y = 6.2454X + 0.398$
2	Profit amount (Rs, lakhs)	$R^2=0.9760$	0,814	$Y = 0.0140X + 1.165$
3	Break Even Point (Months)	$R^2=0.8600$	0,930	$Y = -0.5860X + 5.530$
4	Pay Back Period (Annum)	$R^2=0.5230$	0,724	$Y = -0.3210X + 4.045$
5	Internal Rate of Return (%)	$R^2=0.0024$	0,049	$Y = 0.1230X + 27.495$

Working Capital

The working capital requirement is the minimum amount of resources that a production unit cover effectively as cost necessary to operate the business. The working capital (Table -3, column II) includes the cost of raw material inventory for 03 months.

This has been the fixed amount that remains more or less permanently invested for ones as working capital in production unit. There has been excellent correlation of 0.94 exists with the initial cost of feed plant vs. working capital. It is higher the initial capital investment the greater would be the capacity to produce feed and ultimately more of the raw material and finished feed inventory would require to use into the plant operational system. However, for higher capacity plant the high working capital investment require assured market of quality processed feed. Many a times due to socio economic problems the total operational days of production unit may get drastically reduced.

Profitability Index (PI)

The profitability index (PI) or benefit cost ratio (BCR) (Eq. 1) is an alternative way of stating the net present value (NPV) help in choice of profitable feed plant variant pertaining to marketability. A shortcoming of BCRs is that, by definition, they ignore non-monetized impacts.

$$PI = \text{Present Value of Cash Inflows} / \text{of Cash Outflows} \quad (1)$$

A profitability index of 1.0 means one has achieved exactly one's set target of sustainability of enterprise i.e. rate of return greater than 1.0 means one has exceeded one's pre-set rate of return. It is most commonly used method for comparing economic alternatives. The objective is to determine whether the benefit (gained) in return to any cost (spent) is favorable.

The profitability index (Table 3 and column IV) varies from 1,193 (variant No.1), 1,227 (variant No. 2), 1,182 (variant No. 3) and 1,206 (variant No. 4). The profitability index reveals that variant 2 and variant 4 shows PI values more than 1,2 reflect that variants having maximum capacity utilization due to assured product utilization back-up farming practices would generate more income and benefit.

Break Even Points

Break-even is the point at which total revenue equals total costs (Eq. 2, 3 and 4). At levels of output below the break-even point the business will be making a loss vice versa a profit. Due to its simplicity a new business will often have to present a breakeven analysis to its bank in order to get a loan. However, its disadvantage is that, it assumes that everything produced is sold; often not all output will be sold.

$$\text{Contribution} = \text{Selling Price} - \text{Variable cost} \quad (2)$$

$$\text{Break Even Point (₹)} = (\text{Fixed Costs} \times \text{Sales}) / (\text{Contribution}) \quad (3)$$

$$\text{Break even Point Feed Sold (q)} = \text{Fixed Costs} / \text{Contribution per (q)} \quad (4)$$

It is from Tab. 3, the breakeven point of variant 02 (Table 3 column (V)) have the least value i.e. 2.90 indicates that opportunity exists for encouraging investment if forward, backward and sideway linkages are well facilitated (i.e. vertical and horizontal integration of feed production unit) to sustain in the production catchment.

Pay Back Period

Payback period is simple to compute (Eq. 5), provides some information on the risk of the investment and provides a crude measure of liquidity. It does not indicate any concrete decision criteria to understand whether an investment increases the feed production firm's value. However, as a drawback, it provides no measure of profitability.

$$\text{Pay Back Period} = \text{No. of preceding years before final recovery} + \frac{\text{Balance recoverable amount}}{\text{cash flow during the year of final recovery}} \quad (5)$$

The payback period (Table 3, column (VI)) payback period is least and second to the least i.e. 2.53 a and 3.04 a for variant 2 and variant 1 respectively, point out that sustainability and profitability of multicultural activities are always beneficial for on farm management of agriculture-aquaculture-animal husbandry-agro-industrial activities to encourage for sustainability for growing human population requirement.

Internal Rate of Return

The internal rate of return is a rate of return used in capital budgeting to measure and compare the profitability of investments. It is considered to be very important economic parameter for investment viability factor analysis for variant selection. It is that rate which equates the present value of the future cash inflows with the cost of the investment which produces them. *IRR* calculates (Eq. 6) an alternative cost of capital including an appropriate risk premium. It takes into account the time value of money. The cost of capital if less than *IRR* then project proposal may be considered as an alternative for investment decision.

$$\text{IRR} = \text{Lower rate of discount} + \frac{\text{Net present value at lower rate of discount}}{\text{Difference in present values at lower and higher discount rates}} \times (\text{Difference in two rates of discount}) \quad (6)$$

The internal rate of return *IRR* (table 3, column (VII)) is greatest and second to the greatest are 30.98 % and 29.11 % for variant 2 and 3 respectively, point out that strong linkage under production-supply chain, would ultimately ensure higher *IRR* shall foresee encouraging economic returns. As per (Fig. 1) initial investment has excellent correlation with working capital, profitability index and breakeven point. However, there has been moderate correlation exist with payback period and poor correlation observed with initial investment versus internal rate of return (*IRR*) for all the variants investigated under optional studies.

CONCLUSIONS

Out of above four feed production variants, variant No. 01 and No. 02 may be opted for integrated agriculture-aquaculture-animal husbandry activities. The variant no. 01 may be opted for limited demand of feed. On the other hand, if sufficient feed demand is

available for sustainable multicultural activities (such as dairy, goat , poultry enterprise inclusive of aquaculture farms) then production variant No. 2 has maximum economic returns i.e. least time for breakeven point, payback period and high percentage of internal rate of return (*IRR*) and top most profitability index. The government subsidy and local economic impact may also be considered as crucial deciding factors for variant No. 01 and variant No. 02. While variant 3 or 4 may be opted solely for feed production for dairy enterprise. Therefore, reliable information about economic viability may emerge on appropriate capacity utilization of feed production unit.

In case if investor wants to play under safe game-plan by avoiding risks and also confined with limited investment potential for augmentation of feed business then the best idea would be to choose production variant no. 3 though herein breakeven point and payback period are little longer but internal rate of return is high in comparison to other variant 1 and 4. Variant No. 02 has ultimately least of working capital requirement, early payback period, greater internal rate of return, better profitability index than that of variant no.3.

The idea floated on account of economic analysis through application of parameters viz. Working Capital, Profitability Index (*PI*), Break Even Point (*BEP*), Pay Back Period (*PBP*), Internal Rate of Return (*IRR*), may either be implemented or rejected under the specific choice of alternative available for production variants may it be integrated farming/ mixed farming or eventually organized dairy development in unit way or under the cluster approach. Herein, the ultimate objective is to grow more nutritious food for growing human population. In this direction, establishment of unit like multipurpose feed production variant or exclusive dairy feed production unit based on maximum capacity utilization of available resources would prove to be a boon to generate sufficient scope for sustainable and profitable returns under agrarian economy.

BIBLIOGRAPHY

- [1] Ambalkar, P.P., Singh, J., Bhandarkar, D.M. 2003. Techno-economic feasibility of feed plant in rural sector. 37th ISAE annual convention and symposium, January 29-31, 2003, MPUAT, Udaipur, India.
- [2] Banerjee, G.D., Banerjee, S. 2004. *Tea Industry – A Road Map Ahead*. Abhijeet Publications, Delhi, pp-37-54.
- [3] Koutsoyiannis, A,1979. *Modern Microeconomics*. The Macmillan Publication. London.
- [4] Olaloku, E.A. 1976. Milk production in West Africa: Objective and Research approaches. *Journal of the Association for the Advancement of Agricultural Sciences in Africa* 3(1). p.p. 5-13.
- [5] Pullan, N.B., Grindle, R.J. 1980. Productivity of white Fulani cattle on the Jos Plateau Nigeria. IV. Economic factors. *Tropical Animal Health and Production*. 12, p.p. 161-170.
- [6] Sarkar, S.K. 2002. *Freshwater Fish Culture - Volume 1- Integrated Fish Farming*. Daya Publication, p.p. 247-260.
- [7] Singh, J., Singh, G. 2001. *Aqua Feed Plant Broacher*, Central Institute of Agricultural Engineering, Nabibagh, Berasia Road, Bhopal,MP, India.

UPOREDNA PROCENA PROIZVODNIH VARIJANTI UREĐAJA ZA PROIZVODNJU KONCENTROVANE STOČNE HRANE

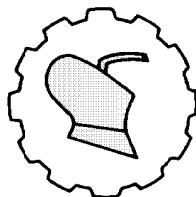
Prakash Prabhakar Ambalkar, Praveen Chandra Bargale, Jai Singh

*Centralni institut za poljoprivrednu tehniku, Odsek za transfer tehnologija,
Bhopal, MP, Indija*

Sažetak: Uređaj za proizvodnju peletirane hrane koja zadovoljava potrebe za balansiranom ishranom, optimalnim preradom, troškovima i efikasnim iskorišćenjem vremena pri ishrani životinja / riba može se prilagoditi za profitabilnu proizvodnju. Tehnologija proizvodnje peletiranog hraniva može da se komercijalizuje modularnom konstrukcijom i razvojem uređaja za proizvodnju hraniva prema onom koji je razvijen u Centralnom institutu za poljoprivrednu tehniku u Bhopal-u u Indiji. Razlog za postizanje ovog cilja je sigurna investicija u razvoj uređaja za proizvodnju hraniva. Analizirana je ekonomska opravdanost proizvodnje određene količine hraniva prihvatanjem profitabilne ideje kroz određivanje ekonomskih promenljivih uticaja na proizvodnu varijantu, kao što su radni kapital (₹), tačka rentabilnosti (meseć), period otplate (*a*), odnos prihoda i troškova i interna stopa prinosa (*IRR* u procentima). Proučavane su četiri različite varijante proizvodnje peletirane hrane. Varijante br. 01 i 02 su posebno predviđene za višekomponentnu hranu kod mešovitog / integrisanog stočarstva (životinja-biljka-riba), a kombinacija varijanti 03 i 04 samo za ishranu muznih krava. Sve 4 varijante su predstavljene kao ekonomski održiva preduzeća za odgovarajući izbor kapaciteta i konkurentnosti finalnog proizvoda.

Ključne reči: *stočna hrana, varijante proizvodnje hraniva, korišćenje kapaciteta, parametri ekonomske varijabilnosti, uporedna procena i INR.*

Prijavljen: 18.07.2013.
Submitted:
Ispravljen:
Revised:
Prihvaćen: 18.09.2013.
Accepted:



UDK: 536.7

Originalni naučni rad
Original scientific paper

A SIMPLE MODEL FOR EVAPORATIVE COOLING SYSTEM OF A STORAGE SPACE IN A TROPICAL CLIMATE

Chinenye Ndukwu^{1*}, Seth Manuwa², Olawale Olukunle², Babatunde Oluwalana³

¹*Michael Okpara University of Agriculture, College of Engineering and Engineering
Technology, Department of Agricultural and Bio Resources Engineering,
Umudike, Abia State, Nigeria*

²*Federal University of Technology Akure, School of Engineering and Engineering
Technology, Department of Agricultural Engineering, Akure, Ondo State, Nigeria*

³*Federal University of Technology Akure, School of Agriculture and Agricultural
Technology, Department of Food Science and Technology,
Akure, Ondo State, Nigeria*

Abstract: This paper deals with the development of a simple mathematical model for experimental validation of the performance of a small evaporative cooling system in a tropical climate. It also presented the coefficient of convective heat transfer of wide range of temperatures based on existing model. Extensive experiments have been performed during January to February 2013 for a small evaporative cooler designed for storage of fruits and vegetables. The model considered the thermal properties of the material of the cooling pad and assumed that the cooling pad is a plain porous wall bounded by two convective airs at different temperature at the two surfaces. The predicted and experimental value of various cooling efficiency at different range of inlet temperature has been determined. In addition the values of the coefficient of convective heat transfer for a wide range of temperatures is also presented.

Key words: *evaporative cooling, cooling pad, model equation, heat transfer*

* Corresponding author. Email: ndukwumcu@gmail.com

INTRODUCTION

The basic principle of evaporative cooling is cooling by evaporation. When water evaporates, it draws energy from its surroundings, which produces a considerable cooling effect. Evaporative cooling occurs when air, that is not too humid, passes over a wet surface (humidifier). The movement of the air can be passive i.e. when the air flows naturally through the pads or active with fans or blowers. The driving force for heat and mass transfer between air and water is the temperature and partial vapor pressure differences. Water is the working fluid in evaporative cooling thus it is environmentally friendly [1]. Due to the low humidity of the incoming air some of the water evaporates. This evaporation causes two favorable changes: a drop in the dry-bulb temperature and a rise in the relative humidity of the air. This non-saturated air cooled by heat and mass transfer is forced through enlarged liquid water surface area for evaporation by utilizing blowers or fans. Some of the sensible heat of the air is transferred to the water and becomes latent heat by evaporating some of the water. The latent heat follows the water vapor and diffuses into the air. In a DEC (direct evaporative cooling), the heat and mass transferred between air and water decreases the air dry bulb temperature (DBT) and increases its humidity, keeping the enthalpy constant (adiabatic cooling) in an ideal process. However, 100% saturation is impossible for direct evaporative coolers due to two reasons [2]. Firstly, most of the pads are loosely packed or with cells, therefore the process air can easily escape between the pads without sufficient contact with the water. After water evaporates, it enters the air as water vapor and conveys the heat absorbed during evaporation back to the air in the form of latent heat. The effectiveness of this system is defined as the rate between the real decrease of the DBT and the maximum theoretical decrease that the DBT could have if the cooling were 100% efficient and the outlet air were [1]. Practically, wet porous materials or pads provide a large water surface in which the air moisture contact is achieved and the pad is wetted by dripping water onto the upper edge of vertically mounted pads. According to [1] experimental studies are reliable and convincing; but they are usually costly and too tasking. In addition, the experiment results were obtained under various testing conditions which are affected by the environmental conditions with given inlet parameters and the results may be different when testing conditions is changed. Modeling analysis of evaporative cooling system is essential to explain the heat and mass transfer process in evaporative cooling and to predict the process outputs at various conditions. Over the years a number of models have been developed to describe direct evaporative cooling systems, not supported with a heat exchanger. [3, 4, 5, 6]

Most of these models ignore the thermal properties of the cooling pad material which will definitely affect the temperature drop inside the cooling chamber no matter how small. The models consider the heat and mass transfer that occur at the surface of the pad but in actual fact the cooling pad is a plain porous wall with thickness. Also the heat and mass transfer is not only on the surface but across the thickness with the air at the outer surface at different temperature from the air at the inner surface. The paper presents a simple model for direct evaporative cooling, incorporating the thermal properties and the thickness of the material of the pad in the heat and mass transfer process in a tropical environment. It also presents wide range of heat transfer coefficient at the tested conditions.

MATERIAL AND METHODS

Basic Mathematical Model

Model assumptions

1. The system is one dimensional.
2. The system is adiabatic.
3. The inside and the outside temperature of the air is different.
4. The two surfaces of the cooling pad are at different temperatures.
5. The cooling pad is surrounded by air at the two surfaces.
6. The heat transfer coefficient is different for the ambient air and the air bounding the cooling pad on the inside the cooler.
7. The cooling pad is a plain porous wall bounded by two convective fluids (air) at different temperatures.
8. The surface of the pad is completely wet.
9. The pad and the cold air inside are at the same temperature.
10. The water inlet and outlet temperature is the same.
11. The cooling pad is rigid.

Basic model equation

On the assumption that the cooling pad is a plain porous wall bounded by two convective fluids (air) outside the pad surface and inside the cooler, each at different temperature, the elementary sensible heat flux in terms of overall temperature and thermal properties of the pad for Fig. 1 is given by:

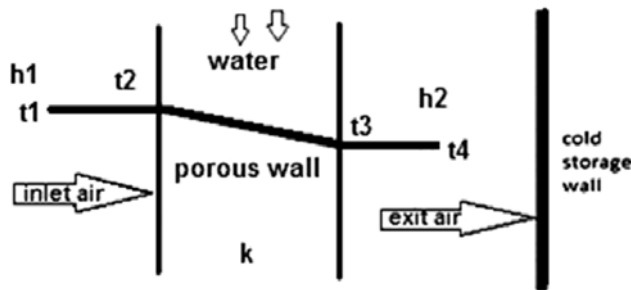


Figure 1. Scheme of the heat transfer process across the porous evaporative cooling pad

$$dq = h_1(T_1 - T_2)dA \tag{1}$$

where:

- q [W·m⁻²] - heat flux,
- h_1 [W·m⁻²·K⁻¹] - convective heat transfer coefficient of the outside air,
- T_1 [°C] - outside air temperature,
- T_2 [°C] - inlet temperature to the porous pad,
- A [m²] - surface area of the pad.

$$dq = \left(\frac{T_2 - T_3}{x_{23}} \right) dA \quad (2)$$

where:

- x_{23} [m] - thickness of the porous pad,
 k_{23} [$\text{W}\cdot\text{m}^{-1}\cdot\text{K}^{-1}$] - thermal conductivity of the pad material,
 T_2 [$^{\circ}\text{C}$] - inlet air temperature into the porous pad,
 T_3 [$^{\circ}\text{C}$] - exit air temperature from the porous pad,
 A [m^2] - surface area of the pad.

$$dq = h_2 A (T_3 - T_4) dA \quad (3)$$

where:

- h_2 [$\text{W}\cdot\text{m}^{-2}\cdot\text{K}^{-1}$] - convective heat transfer coefficient of the inside air,
 T_3 [$^{\circ}\text{C}$] - exit air temperature from the porous pad,
 T_4 [$^{\circ}\text{C}$] - inside air temperature of the evaporative space.

The heat balance for the three equations gave:

$$dq = \left(\frac{T_1 - T_4}{\frac{1}{h_1} + \frac{x_{23}}{k_{23}} + \frac{1}{h_2}} \right) dA \quad (4)$$

[7] gave the mass flow rate of re-circulating water evaporating into air from a surface in terms of the mass transfer coefficient for evaporative cooler as:

$$\dot{\omega} + \left(\frac{\delta \dot{\omega}}{\delta A} \right) dA = \dot{\omega} + h_D (\omega_s - \omega) dA \quad (5)$$

where:

- $\dot{\omega}$ [$\text{kg}\cdot\text{h}^{-1}$] - mass flow rate of water,
 h_D [$\text{kg}\cdot\text{m}^2\cdot\text{s}^{-1}$] - convective mass transfer coefficient,
 ω [$\text{kg}\cdot\text{kg}^{-1}$] - humidity ratio,
 ω_s [$\text{kg}\cdot\text{kg}^{-1}$] - moist air specific humidity.

He gave the simplified solution as:

$$d\dot{\omega} = h_D (\omega_s - \omega) dA \quad (6)$$

Based on equation 6 [6] stated that the water mass flow rate does not remain constant due to the process of evaporation. Simultaneous heat and mass transfer takes place at the air–water interface. [5] analyzed the interface of air – liquid of direct evaporative cooling system, by energy conservation and gave the heat passing through the air -water interface as:

$$dq = m_a c_{pu} dT \quad (7)$$

where:

- m_a [$\text{kg}\cdot\text{h}^{-1}$] - mass flow rate of air,

C_{pu} [kJ·kg⁻¹·K⁻¹] - humid specific heat.

Were C_{pu} is given by:

$$c_{pu} = c_{pa} + w c_{pw} \tag{8}$$

where:

c_{pa} [kJ·kg⁻¹·K⁻¹] - specific heat of dry air,

c_{pw} [kJ·kg⁻¹·K⁻¹] - specific heat of vapor.

Since the quantity of heat loss by draft air and the cooling pad is equal to heat passing through air- water interface. The overall energy balance on the process fluid and the cooling pad will be:

$$\left(\frac{T_1 - T_4}{\frac{1}{h_1} + \frac{x_{23}}{k_{23}} + \frac{1}{h_2}} \right) dA = m_a c_{pu} dT \tag{9}$$

The above equation can be integrated resulting in:

$$\frac{1}{m_a c_{pu} \left(\frac{1}{h_1} + \frac{x_{23}}{k_{23}} + \frac{1}{h_2} \right)} \int_0^A dA = \int_{T_1}^{T_4} \frac{dT}{T_1 - T_4} \tag{10}$$

The integration will yield:

$$- \left[\frac{A}{m_a c_{pu} \left(\frac{1}{h_1} + \frac{x_{23}}{k_{23}} + \frac{1}{h_2} \right)} \right] = in \left[1 - \frac{T_1 - T_4}{T_1 - T_w} \right] \tag{11}$$

$(T_I - T_4 / T_I - T_w)$ is the evaporative efficiency or effectiveness and is represented by \mathcal{E} .

With the hypothesis that air and vapor are perfect gases, [5] gave the enthalpy change as:

$$h_g - h = C_{pu}(T_s - T) + h_{vs}(w_s - w) \tag{12}$$

were:

h_{vs} [kJ·kg⁻¹] - vapour enthalpy of water at the surface temperature.

Assuming that $h_{vs} \approx h_{ivs}$ the above equation becomes:

$$h_g - h = C_{pu}(T_s - T) + h_{is}(w_s - w) \tag{13}$$

were:

h_{is} [kJ·kg⁻¹] - specific enthalpy of water at the surface temperature of the cooling pad,

h_g [kJ·kg⁻¹] - specific enthalpy of saturated water vapour.

However in the presence of difference in enthalpy the term $h_{ls}(w_s-w)$ is neglected [8] therefore the change in enthalpy for the direct evaporative cooler can be written as:

$$\Delta H = c_{pu}\Delta T \quad (14)$$

were:

ΔH [kJ·kg⁻¹] - change in enthalpy,
 ΔT [°C] - temperature difference.

Therefore:

$$\frac{\Delta H}{\Delta T} = c_{pu} \quad (15)$$

$$A = w \times L \quad (16)$$

were:

W [m] - width of the pad,
 L [m] - length of the pad.

Therefore:

$$- \left[\frac{wL}{\frac{\Delta H m_a}{\Delta T} \left(\frac{1}{h_1} + \frac{x_{23}}{k_{23}} + \frac{1}{h_2} \right)} \right] = in[1 - \varepsilon] \quad (17)$$

$$\varepsilon = 1 - \exp \left\{ - \left[\frac{wL}{\frac{\Delta H m_a}{\Delta T} \left(\frac{1}{h_1} + \frac{x_{23}}{k_{23}} + \frac{1}{h_2} \right)} \right] \right\} \quad (18)$$

The convective heat transfer is calculated from the Nusselt number as follows:

$$N_U = \frac{hl}{k} \quad (19)$$

Where k is the thermal conductivity of air, l is the characteristic length and is given by [5] as:

$$l = \frac{\ell}{A} \quad (20)$$

where:

ℓ [m³] - volume occupied by the pad.

[9] gave a correlation to determine the heat transfer coefficient for a rigid evaporative media as:

$$N_u = 0.1 \left(\frac{l}{x} \right)^{0.12} R_e^{0.8} P_r^{\frac{1}{3}} \quad (21)$$

where:

x [m] - thickness of the pad,

R_e [-] - Reynolds number,

N_u [-] - Nusselt number,

P_r [-] - Prandtl number.

$$R_e = \frac{vl}{\nu} \quad (22)$$

where:

v [$\text{m}\cdot\text{s}^{-1}$] - air speed,

ν [$\text{m}^2\cdot\text{s}^{-1}$] - kinematic viscosity.

Also, the Prandtl number P_r is given by:

$$P_r = \frac{\nu}{\alpha} \quad (23)$$

Where α [$\text{m}^2\cdot\text{s}^{-1}$] is the thermal diffusivity which is given by:

$$\alpha = \frac{k}{\rho c_{pa}} \quad (24)$$

where:

ρ [$\text{kg}\cdot\text{m}^{-3}$] - density of air.

The mass flow rate was generated from the continuity equation as follows:

$$m_a = \rho A_1 v \quad (25)$$

where A_1 is the area of the pad covered by each of the three fan since the pad is divided into three compartments.

Experimental Tests

An experimental test was conducted with palm fruit fiber as the cooling pad material at inlet air velocities of $4.0 \text{ m}\cdot\text{s}^{-1}$ and exit speed of $1.6 \text{ m}\cdot\text{s}^{-1}$. The characteristic length of the pad is 0.3 with a height of 1 m. The pad was divided into three equal area with each mounted with an axial fan delivering $0.5 \text{ kg}\cdot\text{s}^{-1}$ of air at a pad face velocity of $1.6 \text{ m}\cdot\text{s}^{-1}$. The test facility figure 2 was located under an open shade built under a whistling pine tree. This is to reduce direct action of the sun and expose the cooler to natural air. The test was carried out in January and February of 2013; this period presented the extremes of the temperature within the year. At this period, there was rain for 8 days, which presented very high ambient relative humidity of 80 %. In addition, the period presented extreme low humidity of 28 % and very high temperature of 45°C . The palm fruit fiber was loaded into the pad holder at a thickness of 30 mm and a parking density of $20 - 22 \text{ kg}\cdot\text{m}^{-3}$. The upper water tank delivers water at a rate of $10 \text{ cm}^3\cdot\text{s}^{-1}$. The water flows

through the pad by gravity into the bottom tank and re-circulates back with the water pump. The cooler is loaded with 2 kg of pumpkin (cucurbita) and amaranthus. A thermocouple (omega data logger, HH1147) ($\pm 0.1^\circ\text{C}$) was positioned through the hot wire terminals inserted into the cooling chamber. One of the terminals was covered with cotton wool soaked inside the water to measure the wet bulb temperature [10]. The air speed of the fan was determined with vane microprocessor (AM-4826) digital anemometer ($\pm 0.1 \text{ m}\cdot\text{s}^{-1}$). Two ABS temperature and humidity clock ($\pm 0.1^\circ\text{C}$ and 1.0 %) was positioned inside the shade and another outdoor where there is no shade to record the temperature and humidity of the ambient. Two analogue thermometers were inserted inside the two tanks to measure the water temperature. The data were logged every two hours. The relative humidity and the enthalpy of the cooler were obtained from the psychrometric chart. In addition, the wet bulb temperature and the enthalpy of inside the shade and the ambient were calculated also from the psychrometric chart.

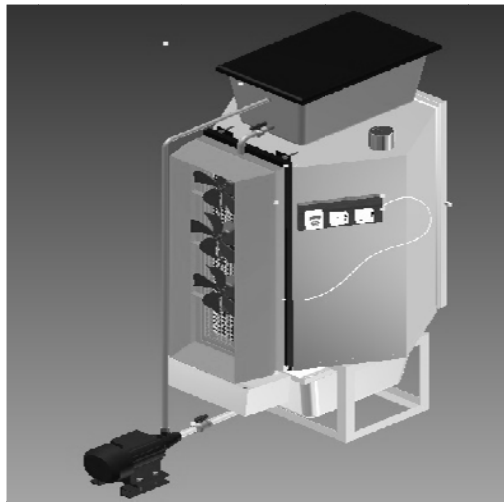


Figure 2. Evaporative cooling system test rig

Performance Evaluation

The cooling efficiency defined by Equation 25 is a widely used index for evaluating the performance of direct evaporative cooling systems [11, 12]. They were used as follows:

$$\text{cooling efficiency}(\%) = \frac{T_{db} - T_s}{T_{db} - T_w} \quad (26)$$

where:

T_{db} [$^\circ\text{C}$]- dry bulb temperature of the outside air,

T_s [$^\circ\text{C}$]- dry bulb temperature of the inside air,

T_w [$^\circ\text{C}$]- wet bulb temperature of the outside air.

RESULTS AND DISCUSSION

Model validation

The mathematical model was validated using data generated from an existing active evaporative cooler Figure 2. The model validation was done at a constant draft air mass flow rate of $0.5 \text{ kg}\cdot\text{s}^{-1}$ and exiting air speed of $1.6 \text{ m}\cdot\text{s}^{-1}$ at a constant pad thickness of 30 mm and water flow rate of $10 \text{ cm}^3\cdot\text{s}^{-1}$ for the first day the ambient temperature ranged from 29.9-34.8°C with a relative humidity of 34-51% while it ranged from 26.1-34°C for the second day with a relative humidity of 38 -69%. Also at the third day the ambient temperature ranged from 27.8-34°C while the relative humidity ranged from 44-73%. At these prevailing environmental condition the cooler maintained a temperature range of 23.2-24.8°C with a relative humidity of 90.4 -94.8% on the first day while on the second day it provided a cooler temperature of 23.2-24.6°C with a relative humidity of 93.6-96.8%. On the third day the ambient condition provided a cooler temperature of 23.8-25.2°C with a relative humidity of 85.6-96.8%. The evaluation parameters (Table 1) were fitted into Eq. 18 to calculate the predicted cooling efficiency while the experimental efficiency was calculated with Eq. 27.

Also air properties determined from psychometric chart were fitted into Eq. 19-23 to calculate the coefficient of heat transfer for the two air conditions. Thermal conductivity of palm fiber was $0.057 \text{ W}\cdot\text{m}^{-20}\text{K}^{-1}$ [13]. The predicted and experimental cooling efficiency is presented in Fig. 3- 5.

Table 1. Evaluation parameters

Evaluation Parameters								
day one			day two			day three		
Time [hr]	ΔH^* [kJ/kg]	ΔT^* [°C]	Time [hr]	ΔH [kJ/kg]	ΔT [°C]	Time [hr]	ΔH [kJ/kg]	ΔT [°C]
10	2.05	4.0	10	2.90	6.0	9	1.54	2.9
12	0.40	6.5	11	6.58	6.7	11	2.37	4.8
14	5.05	9.7	12	4.99	8.2	13	2.04	7.4
16	0.18	8.2	13	5.08	9.0	15	2.12	9.7
18	4.51	7.7	16	3.42	10.0	17	6.74	8.7

* ΔH - change in enthalpy, ΔT - change in temperature.

In order to be certain there is difference in the predicted and experimental efficiency; analysis of variance was performed on the results of the three days of test. The *F* – value shows that there was no significant difference at the 5% level. The average mean efficiency difference on the first day for cooling efficiency and the predicted efficiency was 0.8% while the second day gave average mean difference of 3.45%. Also the third day gave an average mean difference of 3.72%. These values are very close to the experimental values as shown in Fig. 6.

This shows that the model have close to 96 – 99.2% accuracy. Figures 2 and 5 showed that the model performed relatively poorly at 16 hrs for the two days period compared to the rest of the period.

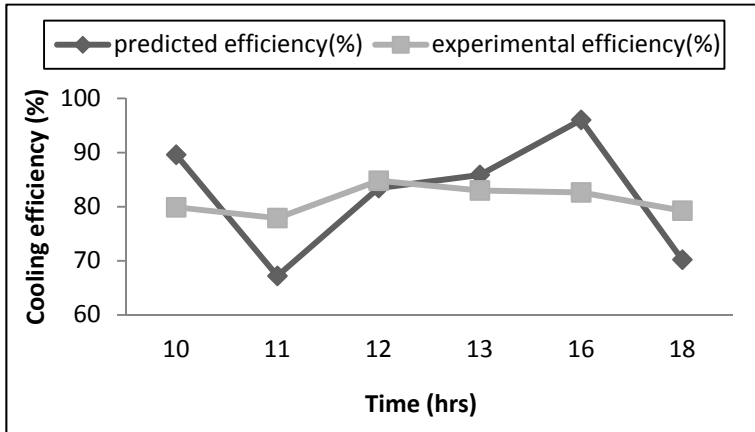


Figure 3. Hourly predicted and experimental cooling efficiency (%) for day one

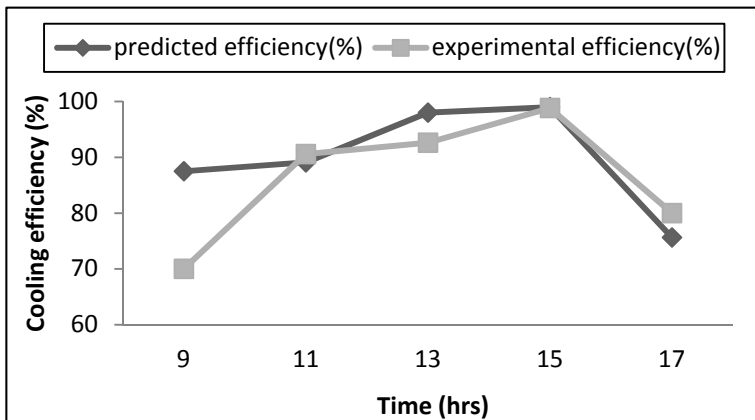


Figure 4. Hourly predicted and experimental cooling efficiency (%) for day two

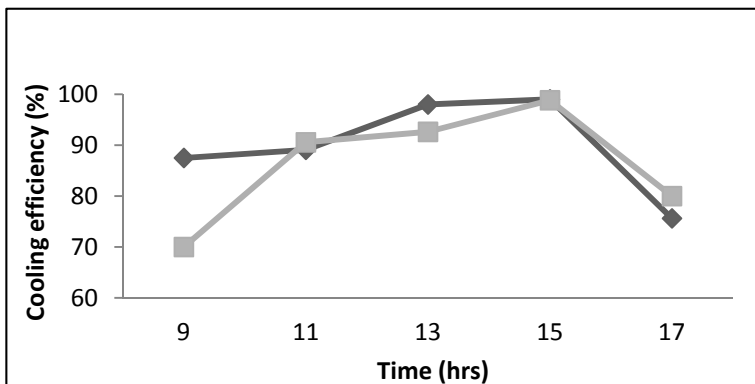


Figure 5. Hourly predicted and experimental cooling efficiency (%) for day three

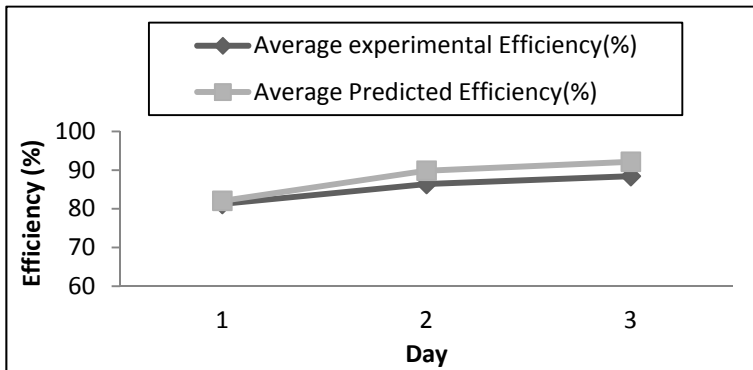


Figure 6. Average daily experimental and predicted efficiency

The best fit equation for the experimental and predicted value is given by:

$$pre(\varepsilon) = -2.745\exp(\varepsilon)^2 + 16.03\exp(\varepsilon) + 68.76 \quad (27)$$

where:

ε [%] - cooling efficiency.

The above equation has R^2 value of 100%.

The value of the Reynolds number at the inlet shows that the air is turbulent ($Re > 5000$) which is typical of force convection. Though the air enters into the cooling pad as a turbulent flow but it emerges as a laminar flow inside the cooling chamber ($Re < 5000$) as shown in Table 1. This shows that the cells of the cooling pad absorb some of the energy from the air.

CONCLUSION

The equation for predicting the cooling efficiency of a direct evaporative cooler for storage has been presented and validated. The model considered the thermal conductivity and thickness of the cooling pad material. The model has 96 – 99.2% accuracy. The plotting of the cooling efficiency relationship with time showed an exponential behavior. The results showed that the cooling efficiency of the systems gradually improves as the day goes by and peaks in the afternoon when the ambient temperature is highest in a tropical environment like Africa. At this period much cooling is required to maintain the cooler within the storage temperature, therefore the high efficiency. In the evening the ambient temperature decreases as shown from fig 3 - 5 and consequently the cooling efficiency decreases. The information presented could be useful in the design of evaporative cooling for other purposes.

REFERENCES

- [1] Xuan, Y.M., Xiao, F., Niu, X.F., Huang, X., Wang, S.W. 2012. Research and application of evaporative cooling in China: A review (I). *Renewable and Sustainable Energy Reviews* Volume 16, Issue 5, p.p. 3535-3546.
- [2] Di, Y.H., Liu, J.P., Huang, X. 2010. *Climate demarcating for application of evaporative cooling air conditioning HVAC*, 40 (2) pp. 108–111.
- [3] Al-Helal, I., Short, T.H. 2003. A CFD study of naturally and ventilated greenhouses in extreme arid climates. ASAE Paper no. 99-5011 in *Cooling Fan-ventilated Greenhouses: a Modelling Study. Biosystems Engineering* 84 (3), p.p. 315–329.
- [4] Liao, C., Chiu, K. 2002. Wind Tunnel Modeling the System Performance of Alternative Evaporative Cooling Pads in Taiwan Region. *Building and Environment*, No. 37, p.p. 177-187.
- [5] Camargo, J.R., Ebinuma, C.D., Cardoso, S. 2003. A mathematical model for direct evaporative cooling air conditioning system. *Engenharia Térmica*, No. 4, p.p. 30-34.
- [6] Qiang, T.W., Shen, H.G., Feng, J.M., Liang, R.J. 2006. Application of direct evaporative cooling air conditioning in moderate and high humid area of China. *Refrigeration and Air-conditioning*, 27 (3), pp. 21–25.
- [7] Qureshi, B.A., Zubair, M.A. 2006. Comprehensive design and rating study of evaporative coolers and condensers. Part I. Performance evaluation. *International Journal of Refrigeration* 29, p.p. 645–658.
- [8] El-dessouky, H.T., Ettouney, H.M., Bouhamra, W. 2000. A novel air conditioning system membrane air drying and evaporative cooling. *Trans IChemE*, Vol. 78, Part A, pp 999- 1009.
- [9] Dowdy, J.A., Karabash, N.S. 1987. Experimental Determination of Heat and Mass Transfer Coefficients in rigid Impregnated Cellulose Evaporative Media. *ASHRAE Transactions*, part 2, v. 93., p.p. 382-395.
- [10] Anyanwu, E.E. 2004. Design and measured performance of a porous evaporative cooler for preservation of fruits and vegetables. *Energy conversion and management* 45, p.p. 2187–2195.
- [11] Jain, D. 2007. Development and testing of two-stage evaporative cooler. *Building and Environment*, 42, p.p. 2549–2554.
- [12] Ndukwu, M. C. 2011. Development of Clay Evaporative Cooler for Fruits and Vegetables Preservation. *Agricultural Engineering International: CIGR Journal*, 13(1), p.p. 1-8.
- [13] Krishpersad, M. 2012. Renewable building thermal insulation-oil palm fiber. *International journal of engineering and technology* 2, p.p. 475-479.
- [14] Ditchfield, C., Tadini, C.C., Singh, R.K., Toledo, R.T. 2006. Velocity and temperature profile, heat transfer coefficient and residence time distribution of temperature dependent Herschel bulky fluid in tubular heat exchanger. *Journal of food engineering* 79, p.p. 632 -638.

MODEL EVAPORATIVNOG SISTEMA HLAĐENJA SKLADIŠNOG PROSTORA U TROPSKIM USLOVIMA

Chinenye Ndukwu^{*1}, Seth Manuwa², Olawale Olukunle², Babatunde Oluwalana³

¹Poljoprivredni univerzitet Michael Okpara, Fakultet za inženjering i inženjersku tehnologiju, Institut za inženjering u poljoprivredi i bio-resursima, Umudike, Abia State, Nigeria

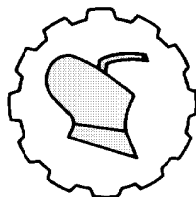
²Federalni tehnološki univerzitet Akure, Fakultet za inženjering i inženjersku tehnologiju, Institut za inženjering u poljoprivredi, Akure, Ondo State, Nigeria

³Federalni tehnološki univerzitet Akure, Fakultet za poljoprivredu i poljoprivrednu tehnologiju, Institut za hranu i prehrambenu tehnologiju, Akure, Ondo State, Nigeria

Sažetak: Ovaj rad se bavi razvojem jednostavnog matematičkog modela za eksperimentalnu ocenu performansi malog evaporativnog rashladnog sistema u tropskim klimatskim uslovima. Predstavljen je i koeficijent konvektivnog prenosa toplote velikog opsega temperature na osnovu postojećeg modela. Obimni eksperimenti su izvođeni tokom januara i februara 2013 sa malim evaporativnim uređajem za hlađenje skladišta za voće i povrće. Model je uzeo u razmatranje termičke osobine materijala rashladnog sloja i pretpostavio da je rashladni sloj ravan porozni zid ograničen sa dva konvektivna sloja vazduha na različitim temperaturama na obe granične površine. Određene su izračunate i eksperimentalne vrednosti različitih efikasnosti hlađenja pri različitim opsezima ulaznih temperature. Uz to, predstavljene su i vrednosti koeficijenata konvektivnog prenosa toplote za veliki opseg temperatura.

Ključne reči: evaporativno hlađenje, rashladni sloj, jednačina modela, prenos toplote

Prijavljen: 02.07.2013.
Submitted:
Ispravljen: 20.09.2013.
Revised:
Prihvaćen: 21.09.2013.
Accepted:



UDK: 574.4

*Originalni naučni rad
Original scientific paper*

DEVELOPMENT OF DROUGHT SEVERITY – AREAL EXTENT – FREQUENCY CURVES IN THE PARAMBIKULAM - ALIYAR BASIN, TAMIL NADU, INDIA

Muthiah Manikandan*, Dhanapal Tamilmani

*Tamil Nadu Agricultural University, Agricultural Engineering College & Research
Institute, Department of Soil & Water Conservation Engineering,
Coimbatore, Tamil Nadu, India*

Abstract: Assessment and characterization of regional droughts provide useful information for sustainable water resources planning and management. In the present study, the Standardized Precipitation Index (*SPI*) a most widely used rainfall based drought index was applied to investigate the temporal characteristics, areal extent and frequency of meteorological drought in the Parambikulam-Aliyar basin, Tamil Nadu. For this purpose, the basin was divided into 97 grid-cells of 5×5 km with each grid correspondence to approximately 1.03% of total area. Gridded monthly rainfall was developed by spatial interpolation technique with the help of GIS capabilities at each grid point using monthly rainfall data for the period of 40 years (1972-2011) from 28 rain gauge stations. Regional representative of *SPI* values calculated from spatially averaged mean areal rainfall were used to characterize the temporal variation of drought. Drought severity-areal extent-frequency (*SAF*) curves were constructed using gridded *SPI* values to assess the drought severity and areal extent with respect to return period so as to describe and characterize the spatial and recurrence patterns of drought. The analysis of *SPI* suggests that the basin suffered severe droughts in the 1970s, 1980s and 2000s. The *SAF* curves developed in this study can be used for the development of a drought preparedness plan in the region and planning sustainable water resource management within the basin.

Key words: *extreme value type I distribution, GIS, rainfall, SAF curves, SPI, weighted cumulative annual drought severity*

* Corresponding author. E-mail: muthiahmanikandan29@gmail.com

This research work was financially supported by the Council of Scientific and Industrial Research (CSIR), Human Resource Development Group (Extra Mural Research Division), New Delhi under research fellowship program.

INTRODUCTION

Drought is a disastrous natural phenomenon that has significant impact on socio-economical, agricultural, and environmental spheres. Drought occurs in virtually all climatic zones, such as high as well as low rainfall areas and is mostly related to the reduction in the amount of rainfall received over an extended period of time, such as a season or a year [1]. In general, drought gives an impression of water scarcity resulted due to insufficient rainfall, high evapo-transpiration, and over-exploitation of water resources or combination of these parameters [2]. Drought impacts both surface and groundwater resources and can lead to reduced water supply, deteriorated water quality, crop failure, reduced range productivity, diminished power generation, disturbed riparian habitats, and suspended recreation activities, as well as affect a host of economic and social activities. Drought differs from other natural hazards in that its onset and end are difficult to determine. It develops slowly, and its impacts may remain for years after termination of the event. Timely determination of the level of drought will assist the decision making process to reduce the impacts of droughts. These types of information may be obtained through drought monitoring.

The definition of drought has been important for drought monitoring and analysis. Drought has been categorized into meteorological (lack of precipitation), hydrological (drying of surface water storage), agricultural (lack of root zone soil moisture), and socio-economic (lack of water supply for socioeconomic purposes) ones. The first three categories are referred as environmental indicators and the last category is considered as a water resources indicator [3]. This study focuses on the meteorological drought which is defined as deficit of rainfall over a region within a certain time interval.

Droughts are usually assessed and monitored by drought indices. A drought index is typically a single value used for indicating the severity of a drought and is far more useful than raw data in understanding the drought conditions over an area. The most commonly used meteorological drought indices are: 1) Rainfall deciles; 2) the Palmer Drought Severity Index (*PDSI*); 3) Percent of Normal; 4) *Z*-index; and 5) the Standardized Precipitation Index (*SPI*). The *SPI* was used in this study because *SPI* quantifies the rainfall deficit for multiple time scales and reflects the impact of drought on the availability of different types of water resources. For example, soil moisture is highly affected by the short term rainfall anomalies, whereas stream-flow, groundwater and reservoir storage slowly respond to longer-term rainfall anomalies.

As droughts are regional in nature and commonly cover large areas and extend for long time periods, it is important to study such events within a regional context. Information on regional drought characteristics provides critical values for different water based activities, and should be included in strategic short and long-term plans for adequate water resource management. The properties of regional droughts can be studied by analyzing the spatial pattern of at-site (point) droughts or one can study regional drought characteristics like the area covered by drought and total rainfall deficit over the drought area. A method to estimate severity-area-frequency curves has been used in this study to estimate the return periods of annual regional droughts [4].

Drought is a frequent phenomenon in India and drought areas are mainly confined to the Peninsular and Western parts of the country and there are only few pockets in the central, eastern, northern and southern parts. Out of 329 Million ha of total geographical area in India about 107 Million ha of lands are subjected to different degrees of water

stress and drought conditions [5]. More than 100 districts spread over 13 states of India have been identified as drought prone districts, out of these, about 8 districts occur in the Tamil Nadu [6]. The western regions of Tamil Nadu (Coimbatore and Tiruppur districts) have suffered with severe droughts at many times in the past. Due to the growth of population and expansion of agricultural, energy and industrial sectors, the demand for water has increased manifold and even water scarcity has been occurring almost every year. Other factors, such as climate change and contamination of water supplies, have further contributed to the water scarcity. In recent years, floods and droughts have been experienced with higher peaks and severity levels. Assessment of droughts is of primary importance for water resources planning and management. This requires understanding historical droughts in the region as well as different concepts of droughts that will be helpful to investigate different drought properties. The present study was carried out in the Parambikulam-Aliyar basin spread over drought prone districts of Coimbatore and Tiruppur, Tamil Nadu. The main objective of this study is to analyze the temporal variation of droughts and construct the Drought Severity–Areal Extent – Frequency curves for spatial analyze of regional drought.

MATERIAL AND METHODS

Study area and data used: Parambikulam-Aliyar basin (referred as PAP basin) is located in the south western part of the Peninsular India covering areas in Kerala and Tamil Nadu States (Fig. 1). Parambikulam Aliyar river basin is the only basin in Tamil Nadu having west flowing rivers. Bharathapuzha river or Ponnani river and Chalakudi river are the two important major rivers are originating in Tamil Nadu State at South Western part of Coimbatore district in the Anamalai hill ranges of Western Ghats. Parambikulam – Aliyar basin is drained by west flowing rivers viz. Valayar, Koduvadiaru, Uppar, Aliyar and Palar (tributaries of Bharathapuzha river) and Parambikulam, Solaiyar and Nirar (tributaries of Chalakudi river). They are grouped into 4 sub basins such as Valaiyar sub basin, Aliyar sub basin, Palar sub basin, and Solaiyar sub basin and spread over an area of 2,388,72 km². One third of the basin area (822,73 km²) is covered with hills and dense forest cover. This basin is bounded in north and east by Cauvery basin, south and west by Kerala State. This basin area lies (except the ayacut area) within the coordinates of North latitude between 10° 10' 00" to 10°57'20" and East longitudes 76°43'00" to 77° 12'30". Parambikulam-Aliyar river basin has an undulating topography with maximum contour elevation in the plain is 300m and the maximum spot height in the plain is 385m above MSL. The temperature slowly rises to its maximum in summer up to May and afterwards shows a gradual decline. The maximum temperature ranges from 36°C to 41°C and the minimum temperature varies from 14°C to 31°C. The major crops grown in the catchment are Paddy, Coconut, Groundnut, Vegetables, Cotton, Tapioca, Maize and Sugarcane. Northern parts of the basin include Thondamuthur, Madukkarai, Sultanpet and Kinathukadavu block; Central parts include Pollachi North, Pollachi South, Anamalai and Udumalipet block; Southern parts include Valparai and some parts of Anamalai block.

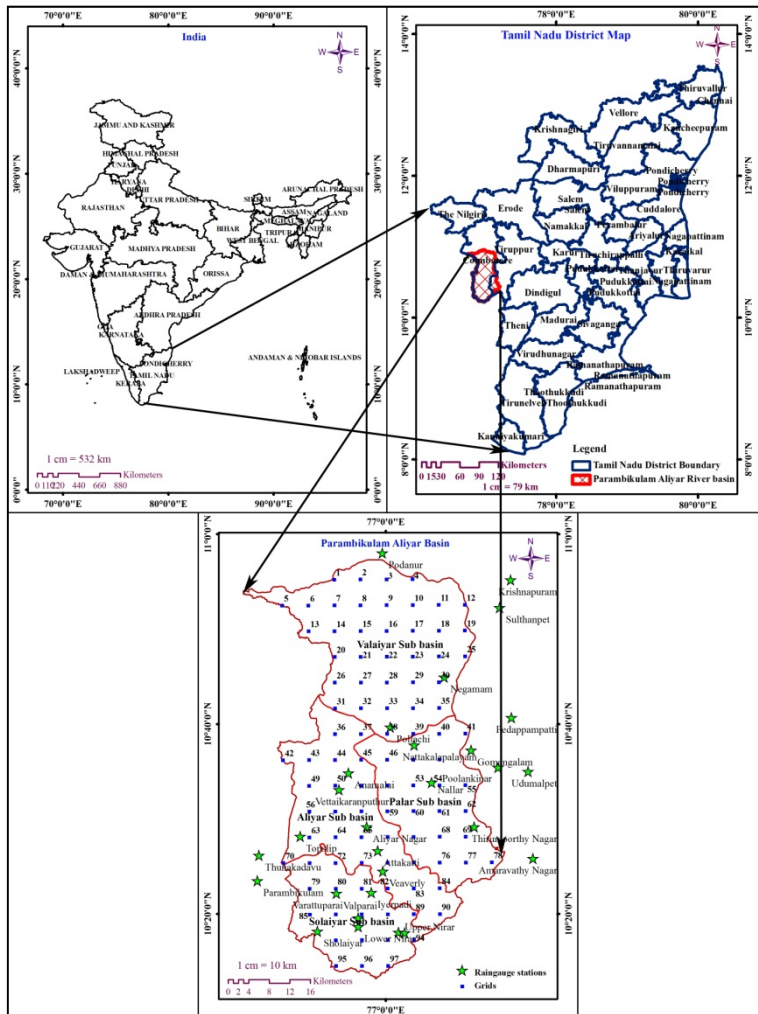


Figure 1. Location of study area and rain gauges in the PAP basin

The investigation used the rainfall as meteorological drought indicator. The monthly rainfall data for the period of 40 years (1972-2011) of 28 rain-gauge stations located in the *PAP* basin was collected from the office of Groundwater division, Public Works Department, Coimbatore. Distribution of these meteorological stations is shown in Fig. 1. The *PAP* basin has a large geographic variation. More rainfall can be observed in the southern parts of the basin. When it comes to the middle and northern parts of the basin, the rainfall decreases. The prolonged and significant decrease on monthly and annual rainfall resulted in irrigation cutbacks, over exploitation of groundwater and significant losses of crop yields. The Parambikulam-Aliyar river basin was considered as a study area because the basin experienced severe, extreme and prolonged droughts during 1970s, 1980s, 1990s and 2000s. During these periods the monthly and annual

precipitation and inflows to the reservoir was significantly below normal. Since the basin is affected by short term, medium term and long term drought frequently, it is necessary for the water resources managers to investigate drought in the basin.

The methodology comprised of the generation of gridded rainfall using spatial interpolation technique, development of mean monthly areal rainfall and gridded rainfall at multiple time scale, calculation of *SPI* values using mean areal rainfall for temporal drought analysis, calculation of gridded *SPI* values using gridded rainfall for construction of Drought Severity-Areal Extent-Frequency curves.

Spatial interpolation of rainfall: Spatial interpolation techniques estimate the value of the surface at locations where no observed data exists, based on the known data values (observations). A number of spatial interpolation methods such as inverse distance weighting (*IDW*), Splines and kriging are available for spatial analysis of any variables and some researchers have used these techniques for drought studies [7, 8, 9]. In this study, *IDW* approach which gives better results than Thiessen polygon method [5] was used for spatial interpolation of rainfall and drought characteristics over the PAP basin.

Total area of *PAP* basin was divided into 97 grids with each grid (5×5 km) approximately correspondence to 1.03% of total area (2425 km²) (Fig. 1). The monthly rainfall data for 40 years (1972-2011) was interpolated by ArcGIS 9.3 using *IDW* method and gridded monthly rainfall was created at various time scales (i.e. 3-, 6-, 12-, and 24- month). Mean monthly areal rainfall of *PAP* basin was estimated by averaging gridded rainfall for the various time scales. The procedure, followed for the calculation of gridded *SPI* values, is referred interpolate-calculate, because first rainfall is spatially interpolated and, then, the *SPI* time series are calculated [10].

Use of the Standardized Precipitation Index (*SPI*) for Drought Analysis: The Standardized Precipitation Index (*SPI*) as a drought assessment tool was developed at Colorado State University, U.S. to quantify the rainfall deficit, and has been used to monitor drought conditions [11]. A drought event occurs at the time when the value of *SPI* is continuously negative and the event ends when the *SPI* becomes positive. The *SPI* may be calculated at multiple timescales (3-, 6-, 12-, and 24- months). The use of multiple timescales allows the effects of a rainfall deficit on different water resource components (groundwater, reservoir storage, soil moisture, stream-flow) to be assessed. Tab. 1 provides a drought classification based on *SPI*. Numerous studies have been conducted to analysis the meteorological droughts using *SPI* [8, 9, 12, 13, 14, 15, 16].

Table 1. Drought classification by *SPI* or *SDI* value and corresponding probabilities

<i>Sl.No.</i>	<i>Drought Category</i>		<i>SPI</i>	<i>Probability (Per cent)</i>
1	<i>D1</i>	<i>Mild drought</i>	0 to -0.99	34.1
2	<i>D2</i>	<i>Moderate drought</i>	-1.00 to -1.49	9.2
3	<i>D3</i>	<i>Severe drought</i>	-1.50 to -1.99	4.4
4	<i>D4</i>	<i>Extreme drought</i>	≤ -2.00	2.3

Calculation of *SPI*: The *SPI* for any location is calculated, based on the long-term rainfall record for a desired period. This is performed separately for each month and for each grid in space. The long-term record is fitted to a probability distribution, which is then transformed to a normal distribution so that the mean *SPI* for the location is zero and standard deviation of unity [11].

The gamma distribution is defined by its probability density function is:

$$g(x) = \frac{1}{\beta^\alpha \Gamma(\alpha)} x^{\alpha-1} e^{-x/\beta} \text{ for } x > 0 \quad (1)$$

where:

$\alpha > 0$ [-] - shape factor,
 $\beta > 0$ [-] - scale factor,
 $x > 0$ [mm] - amount of rainfall.

$\Gamma(\alpha)$ is the gamma function which is defined as

$$\Gamma(\alpha) = \int_0^\infty y^{\alpha-1} e^{-y} dy \quad (2)$$

Fitting the distribution to the data requires that α and β be estimated. Edwards and McKee (1997) [17] suggested a method for estimating these parameters using the approximation of Thom (1958) [18] for maximum likelihood as follows:

$$\hat{\alpha} = \frac{1}{4A} \left(1 + \sqrt{1 + \frac{4A}{3}} \right) \quad (3)$$

$$\hat{\beta} = \frac{\bar{x}}{\hat{\alpha}} \quad (4)$$

Where:

$$A = \ln(\bar{x}) - \frac{\sum_{i=1}^n \ln(x)}{n} \quad (5)$$

for n observations.

The resulting parameters are then used to find the cumulative probability of an observed rainfall event for the given month or any other time scale.

$$G(x) = \int_0^x g(x) dx = \frac{1}{\hat{\beta}^{\hat{\alpha}} \Gamma(\hat{\alpha})} \int_0^x x^{\hat{\alpha}-1} e^{-x/\hat{\beta}} dx \quad (6)$$

Substituting t for $x/\hat{\beta}$ reduces the above equation to incomplete gamma function:

$$G(x) = \frac{1}{\Gamma(\hat{\alpha})} \int_0^x t^{\hat{\alpha}-1} e^{-t} dt \quad (7)$$

Since the gamma function is undefined for $x = 0$ and a precipitation distribution may contain zeros, the cumulative probability becomes:

$$H(x) = q + (1 - q)G(x) \quad (8)$$

where q is the probability of zero precipitation. If m is the number of zeros in a rainfall time series, q can be estimated by m/n . In this analysis, a small amount of rainfall was substituted for zero rainfall for each grid. This substitution does not affect the distribution of precipitation.

The cumulative probability, $H(x)$, is then transformed to the standard normal random variable Z with a mean of zero and a variance of one, which is the value of SPI [12, 17].

For $0 < H(x) \leq 0.5$

$$Z = SPI = - \left(t - \frac{c_0 + c_1 t + c_2 t^2}{1 + d_1 t + d_2 t^2 + d_3 t^3} \right) \quad (9)$$

Where

$$t = \sqrt{\ln \left[\frac{1}{(H(x))^2} \right]} \quad (10)$$

For $0.5 < H(x) < 1$

$$Z = SPI = + \left(t - \frac{c_0 + c_1 t + c_2 t^2}{1 + d_1 t + d_2 t^2 + d_3 t^3} \right) \quad (11)$$

Where

$$t = \sqrt{\ln \left[\frac{1}{(1 - H(x))^2} \right]} \quad (12)$$

$$\begin{array}{lll} c_0=2.515517 & c_1=0.802853 & c_2=0.010328 \\ d_1=1.432788 & d_2=0.189269 & d_3=0.001308 \end{array}$$

Construction of drought Severity-Areal Extent-Frequency (*SAF*) curves:

Regional drought analysis is useful for declaring the drought condition or determining the drought severity during a particular year. A regional drought is assumed when a significant fraction of the total area of the region is under drought conditions or, in other words, when the sum of the areas affected by local drought reaches a selected areal threshold so that it is very important to assess the drought for the entire region. Frequency of drought occurrence cannot fully cover the study of droughts, unless it is quantitatively related to other aspects such as severity and areal extent of droughts. This led to the development of drought severity-area-frequency (*SAF*) curves. *SAF* curves are one of the most useful methods to assess drought in a region, which was proposed by Henriques and Santos (1999) [19] and the same procedure was adopted by Kim et al., 2002; Loukas and Vasiliades, 2004; Mishra and Desai, 2005; Zhang et al., 2012 [7, 10, 5, 20]. In this study annual *SAF* curves were developed based on weighted cumulative drought severity at multiple time scales.

The weighted annual cumulative *SAF* curves were developed according to the following procedure: (1) The monthly *SPI* values for each grid for every year were calculated at multiple time scales of 3-, 6-, 12-, and 24-months; (2) The annual weighted cumulative drought severity in each grid was estimated by multiplying the annual sum of *SPI* in monthly dry spells (negative *SPI* values) for a particular time scale by the probability of drought occurrence for each year; (3) The probability of annual drought occurrence for each year and in each grid was estimated by dividing the number of months that have a negative *SPI* value for the particular time scale by 12; (4) The drought severity associated with the areal extents (in terms of percentage of total area) taking different areal thresholds into account was obtained; (5) To find out the best

distribution for the frequency analysis, drought severity was tested using different probability distributions; (6) Frequency analysis was performed using selected probability distribution for each drought areal extent percentage to associate the drought severity with return periods; (7) Weighted annual cumulative *SAF* curves were developed for the particular time scale and repeated the analysis for different time scale. In this analysis each drought event can be allotted uniformly for a particular year, avoid intermittence, and the duration of dry spells within a particular year is implicitly taken into account.

Analysis of drought frequency: The frequency analysis is commonly used in hydrology and meteorology to assess the return period of particular events. Frequency analysis is performed using the selected probability distribution for annual average drought severity at different return periods. In this study, the annual cumulative drought severity has negative values. To be applied before fitting to an available distribution, the negative values of average annual drought severity were transformed to positive values in order to represent the extreme condition and to analyze the associated risk of droughts using the exceedance probability. Various theoretical probability distributions were statistically tested before fitting the observed drought severity. The commonly used probability distributions viz. Normal, Lognormal, Gamma, and Extreme Value Type I were used to evaluate the best fit probability distribution for *SPI*₁₂ annual drought severity and tested by non parametric Kolmogorov–Smirnov (*K-S*) test and parametric Chi-Square tests at 5 per cent and 1 per cent significance levels.

The annual cumulative drought severity X_T to be estimated for a given return period (T) may be represented as the mean μ plus the departure ΔX_T of the variate from mean.

$$X_T = \mu + \Delta X_T \quad (13)$$

The departure may be taken as equal to the product of the standard deviation σ and a frequency factor K_T ; that is, $\Delta X_T = K_T \sigma$. The departure ΔX_T and the frequency factor K_T are functions of the return period and type of probability distribution to be used in the analysis [21]. The expected annual drought severity at various return periods 5, 10, 25, 50, 75 and 100 years were worked out by the best fit probability distribution.

RESULTS AND DISCUSSION

Analysis of rainfall: Gridded rainfall was developed using spatial interpolation technique in *GIS* environment and mean areal rainfall was calculated from the spatially averaged gridded rainfall. The mean annual areal rainfall over the whole *PAP* basin was about 1410.04 mm and it was distributed unevenly in space and time. The mean annual precipitation varied from about 511 mm at the northern plain areas to more than 4328 mm at the southern mountain areas. The average cumulative areal rainfall was compared with normal cumulative areal rainfall over the study period for identifying the worst rainfall deficit years (Fig. 2). From this analysis, it was found that the *PAP* basin experienced rainfall deficits during the periods of 1970s, 1980s and 2000s. During these three periods the monthly and annual precipitation was considerably below normal. Especially, the year 1982, 1976 and 2002 are the first, second and third driest years, respectively. The prolonged and remarkable decrease of monthly and annual

precipitation has a significant impact on water resources of the basin. Severe and extremely dry conditions lead to decrease in supplying the irrigation water, overexploitation of groundwater and dramatic losses of crop yields.

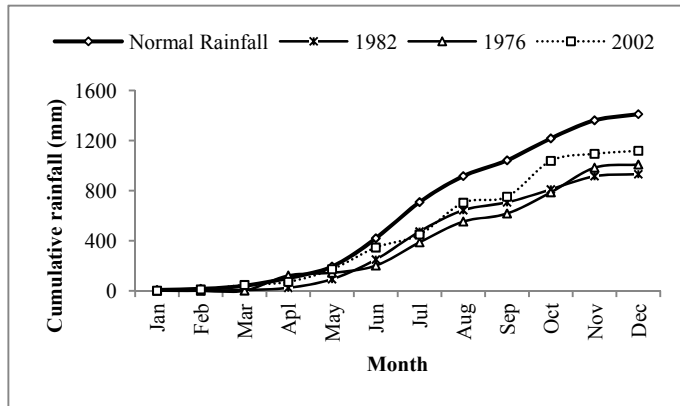


Figure 2. The cumulative areal rainfall for selected rainfall deficit years and periods

Temporal variation of droughts in the PAP basin: The temporal characteristics of droughts in *PAP* basin were analyzed based on the regional representative of *SPI* value to assess the regional drought. The *SPI* values were computed for each month of the year of study period at 3-, 6-, 12- and 24-month time scales for each grid in the *PAP* basin. The *SPI* values on shorter time scale describes drought events affecting agricultural practices, while on the longer ones it is more suitable for water resources management purpose. The regional representative of *SPI* calculated from mean areal rainfall for the *PAP* basin for the time series of 3-, 6-, 12- and 24-month *SPI* (Fig. 3a-d) showed that the region experienced frequent moderate, severe and extreme droughts (i.e. $SPI < -1$) over the period of study. Visual inspection of 3-, 6-, 12- and 24-month *SPI* time series indicated that droughts were quite frequent during the 1970s, 1980s and 2000s. Another notable point observed from the figure that as the time scale increases, drought frequency decreases but its duration increases. At shorter time scales (SPI_3 and SPI_6), drought becomes more frequent but ends for shorter periods. On longer time scales (SPI_{12} and SPI_{24}), drought becomes less frequent but lasts longer.

Occurrence of drought categories: Occurrence of drought categories (from mild to extreme drought) in the *PAP* basin was investigated for each time scale based on the percentage occurrence of each event (within each category) with respect to the total number of observations over the basin in the same category and time scale. Tab. 2 presents the percentage of occurrence of drought categories at 3-, 6-, 12- and 24-month in the *PAP* basin. The numbers are obtained by taking the ratio of drought occurrences in each time scale to the total length of data record in the same time scale and drought category across the basin. The results show that for a given time scale mild droughts occur most frequently and extreme droughts occur least frequently. More than 50 per cent of the study period experienced droughts. The percentage occurrence of drought events with drought severity level of mild to extreme drought has nearly comparable values for all time scales.

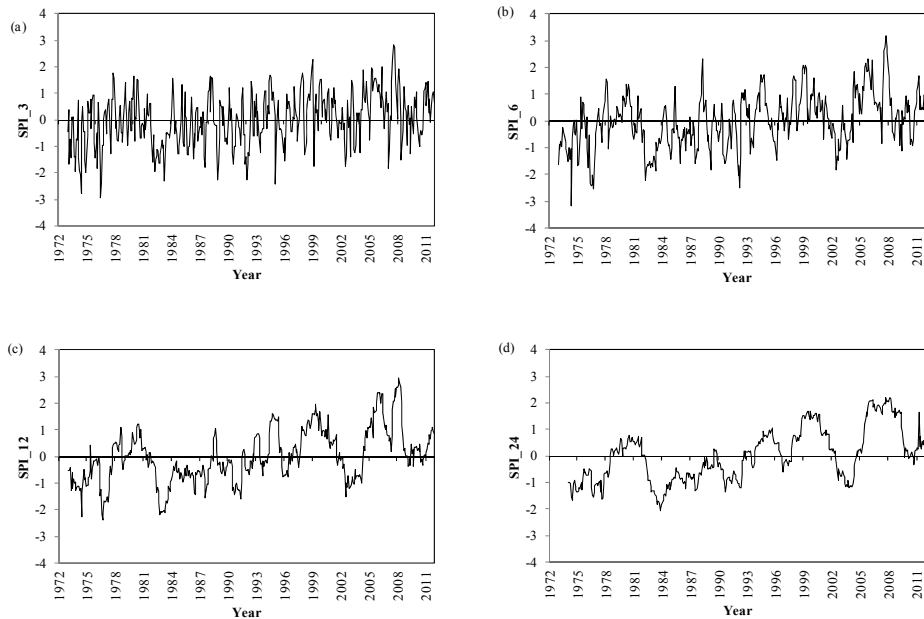


Figure 3. Time series of SPI Values at (a) 3-, (b) 6-, (c) 12- and (d) 24-month, time scales

Table 2. Occurrence of drought categories (percentage) in the PAP basin

Sl.No	Time scale	D1	D2	D3	D4	Total
1	SPI 3	33.76	9.62	4.27	1.92	49.57
2	SPI 6	35.04	8.33	5.56	1.92	50.85
3	SPI 12	39.53	9.62	2.99	2.35	54.49
4	SPI 24	32.46	14.47	3.29	0.44	50.66

Frequency analysis of weighted annual cumulative drought severity:

Frequency analysis was performed using weighted annual cumulative drought severity for searching best fit distribution. In the present work Extreme Value Type I distribution was selected for the frequency analysis as it passed the two tests for SPI_{12} time scale at all grids. It is also a two parameter probability distribution and its parameter values may be estimated with less uncertainty, as the small sample size is used here. It is also used for the numerous extreme drought studies [5, 7, 10, 19, 22, 23]. For the Extreme Value Type I distribution frequency factor can be expressed as:

$$K_T = -\frac{\sqrt{6}}{\pi} \left\{ 0.5772 + \ln \left[\ln \left(\frac{T}{T-1} \right) \right] \right\} \quad (14)$$

Frequency factor of Extreme Value Type I distribution was applied in the Equation 13 and calculated annual cumulative drought severity for different return period (T).

SAF curves of the weighted annual cumulative drought severity: A method to assess the spatial characteristics and the frequency of drought severity over an area is the Drought Severity-Areal Extent- Frequency (*SAF*) curves. In this study, the *SAF* curves were developed for *PAP* basin using gridded *SPI* values. The calculation procedure outlined in the materials and methods has been followed for construction of *SAF* curves.

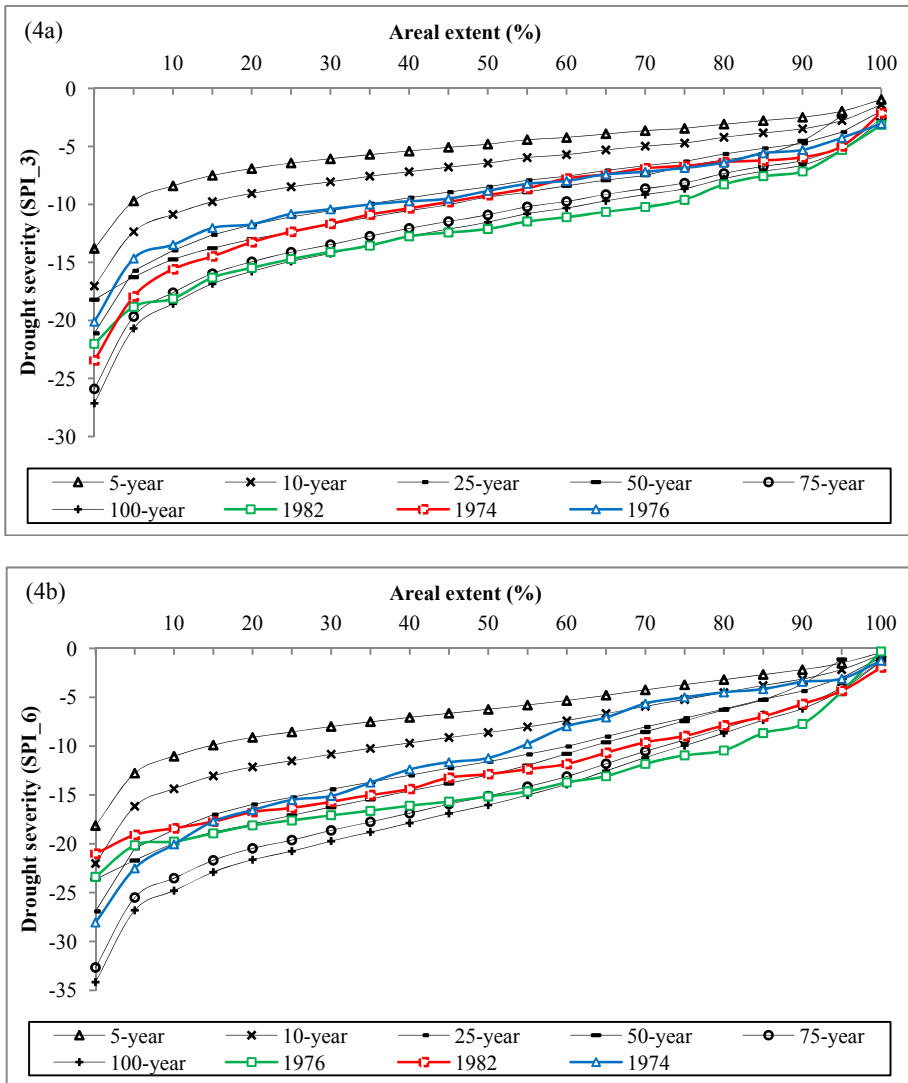


Fig. 4a-d shows the *SAF* curves of weighted annual cumulative drought severity that were developed for 3-, 6-, 12- and 24-month *SPI* values. The *SAF* curves are plotted in Fig. 4a-d, where *X* axis represents percentage of area affected by drought and *Y* axis represents annual drought severity (sum of negative *SPI* values in dry spells) with

different return periods. Most severe drought years recorded during the period of analysis was selected based on highest annual drought severity and driest years were drawn in the *SAF* curves to indentify the recurrence pattern and spatial extent of selected droughts.

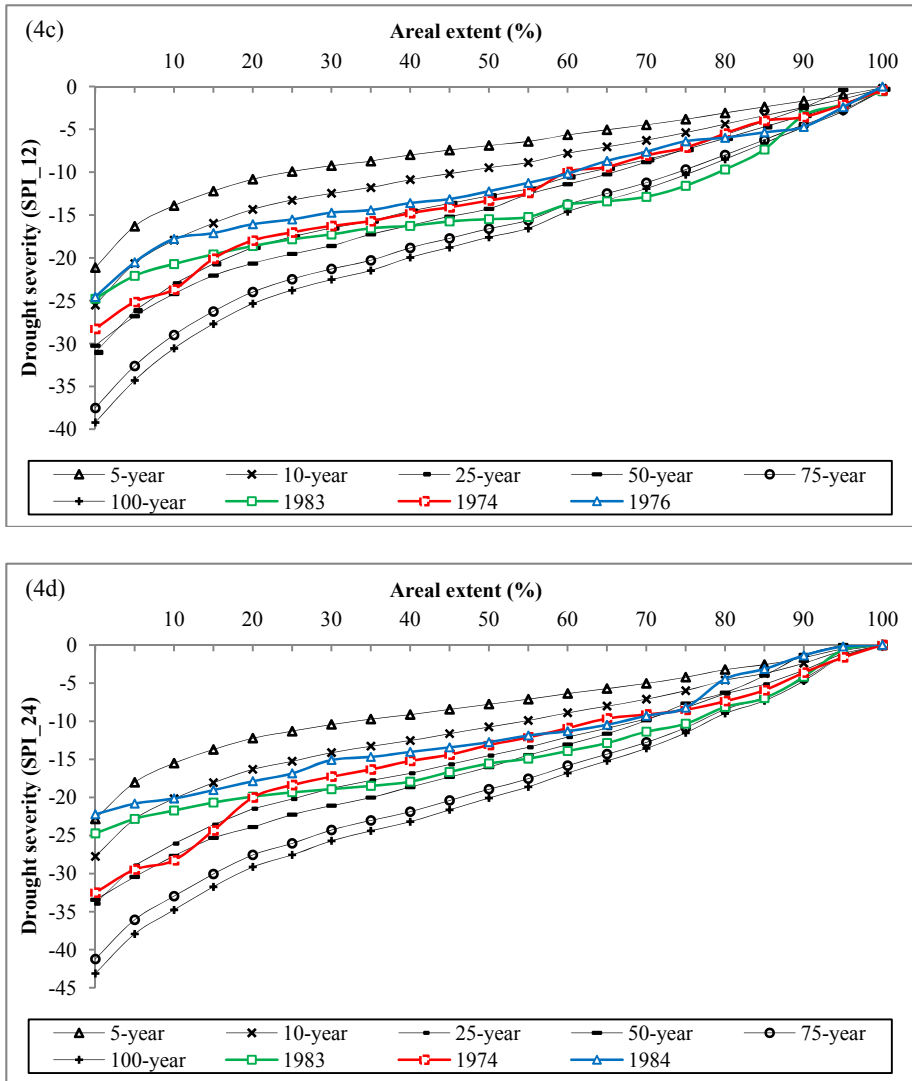


Figure 4. Severity-Areal extent-Frequency curves of the weighted annual cumulative drought severity for (a) 3-, (b) 6-, (c) 12- and (d) 24-month SPI series compared to historical drought

Fig. 4a illustrates the *SAF* curves of SPI₃ for the *PAP* basin and the figure demonstrates that three annual droughts with the highest weighted annual cumulative drought severity in the *PAP* basin occurred during 1982, 1974 and 1976. The drought

that occurred in 1982 has an associate return period of above 100 years with more than 50 per cent of the areal extent. The drought event that occurred in 1974 and 1976 has an associate return period between 25 to 50 years. The most three severe drought year for *SPI_6* based on weighted annual cumulative drought severity was 1976, 1982 and 1974 (Fig. 4b). From the figure, it can be observed that the 1976 drought year has an associate return period of 50 to 100 years. The drought that occurred in 1982 and 1974 has an associate return period between 25 to 50 years.

The droughts of 1983, 1976 and 1974 assessed by *SPI_12* time series have return period between 10 to 25 years (Fig. 4c) and the curve of drought year 1974 runs between the return periods of 10 to 100 years with an increasing areal extent. The drought that occurred in 1983, 1974 and 1984 for 24- month time series have an associate return period between 10 to 50 years (Fig. 4d). From this analysis the year 1974, 1976, 1982, 1983, and 1985 were the severe drought years have large spatial extent and have return period between 10-50 years. Using these curves one can easily identify the drought severity associated with return period drought for a particular drought event.

CONCLUSIONS

This study was focused on analyzing temporal variation and areal extent and frequency of severe droughts in the *PAP* Basin using the *SPI* as an indicator of drought severity. The *SPI* was computed using gridded rainfall at multiple time scales. The temporal analysis of drought was done with mean areal rainfall and *SAF* curves were developed with gridded rainfall over the basin. The temporal and spatial drought analyses indicated that *PAP* basin experience quite frequent moderate and severe droughts on monthly basis. The region has experienced prolonged and severe droughts in terms of severity and durations in the 1970s, 1980s and 2000s. In particular, the persistent and prolonged drought of 1974-1976 and 1982-1985 seriously affected urban water supply, agricultural irrigation, ground water as well as reduction of inflows to the reservoir. The drought severity – areal extent - frequency curve constructed in this study contains drought severity and drought area with respect to drought return period so as to describe and characterize the spatial and recurrence patterns of droughts. It is shown that the drought that occurred in the 1970s and 1980s was associated with a return period of 25 to 50 years with a large areal extent. The identification of the temporal characteristics of droughts and construction of *SAF* curves in the *PAP* basin will be useful for the development of a drought preparedness plan in the region and for sustainable water resource planning and management.

BIBLIOGRAPHY

- [1] Mishra, A.K., Singh, V.P. 2010. A review of drought concepts. *Journal of Hydrology*, 391, p.p. 202-216.
- [2] Bhuiyan, C. 2004. Various drought indices for monitoring drought condition in Aravalli Terrain of India. *Proceedings of the XXth ISPRS Congress*, Istanbul, Turkey, p.p. 12–23.
- [3] Wilhite, D.A. 2000. *Drought as a natural hazard: concepts and definitions*. Drought: a global assessment, Vol. 1. W. D.A. Routledge, New York, USA, p.p. 1–3.

- [4] Hisdal, H., Tallaksen, L. M. 2003. Estimation of regional meteorological and hydrological drought characteristics: A case study for Denmark. *Journal of Hydrology*, 281, 3, p.p. 230-247.
- [5] Mishra, A.K., Desai, V.R. 2005. Spatial and temporal drought analysis in the Kansabati river basin, India. *International Journal of River Basin Management*, 3(1), p.p. 31-41.
- [6] Gupta, A.K., Tyagi, P., Sehgal, V.K. 2011. Drought disaster challenges and mitigation in India: strategic appraisal. *Current science*, 100 (12), p.p. 1795-1806.
- [7] Kim, T., Valdes, J.B., Aparicio, J. 2002. Frequency and spatial characteristics of droughts in the Conchos River Basin, Mexico. *Water International*, 27(3), p.p. 420-430.
- [8] Edossa, D.C., Babel, M.S., Gupta, A.D. 2010. Drought analysis in the Awash River Basin, Ethiopia. *Water Resource Management*, 24, p.p. 1441-1460.
- [9] Moradi, H.R., Rajabi, M., Faragzadeh, M. 2011. Investigation of meteorological drought characteristics in Fars province, Iran. *Catena*, 84, p.p. 35-46.
- [10] Loukas, A., Vasiliades, L. 2004. Probabilistic analysis of drought spatiotemporal characteristics in Thessaly region, Greece. *Natural Hazards and Earth System Sciences*, 4, p.p. 719-731.
- [11] McKee, T.B., Doesken, N.J., Kliest, J. 1993. The relationship of drought frequency and duration to time scales. *Proceedings of the 8th Conference on Applied Climatology*, 17-22 January, Anaheim, CA. American Meteorological Society, Boston, MA, USA, p.p. 179-184.
- [12] Hughes, B.L., Saunders, M.A. 2002. A drought climatology for Europe. *International Journal of Climatology*, 22, p.p. 1571-1592.
- [13] Patel, N.R., Chopra, P., Dadhwal, V.K. 2007. Analyzing spatial patterns of meteorological drought using standardized precipitation index. *Meteorological Applications*, 14(4), 329-336.
- [14] Pradhan, S., Sehgal, V.K., Das, D.K., Singh, R. 2011. Analysis of meteorological drought at New Delhi using SPI. *Journal of Agrometeorology*, 13(1), p.p. 68-71.
- [15] Manikandan, M., Tamilmani, D. 2013. Analysis of meteorological drought characteristics in the Parambikulam-Aliyar basin, Tamil Nadu. *Madras Agricultural Journal*, 100 (1-3), p.p. 236-243.
- [16] Manikandan, M., Tamilmani, D. 2013. Development of drought vulnerability maps in the Parambikulam - Aliyar Basin, Tamil Nadu, India. *Scientific Research and Essays*, 8 (20), p.p. 778-790.
- [17] Edwards, D.C., McKee, T.B. 1997. *Characteristics of 20th Century Drought in the United States at Multiple Timescales*. Colorado State University, Fort Collins, Climatology Report, p.p. 97-2.
- [18] Thom, H.C.S. 1958. A Note on Gamma Distribution. *Monthly Weather Review*, 86, p.p. 117-122.
- [19] Henriques, A.G., Santos, M.J.J. 1999. Regional drought distribution model. *Physics and Chemistry of Earth Part B*, 24 (1-2), p.p. 19-22.
- [20] Zhang, Q., Xiao, M., Chen, X. 2012. Regional evaluations of the meteorological drought characteristics across the Pearl River Basin, China. *American Journal of Climate Change*, 1, p.p. 48-55.
- [21] Chow, V.T. 1951. A generalized formula for hydrologic frequency analysis. *Transactions American Geography Union*, 32 (2), p.p. 231-237.
- [22] Lana, X., Serra, C., Burgueño, A. 1998. Spatial and Temporal Characterization of Annual Extreme Droughts in Catalonia (Northern Spain). *International Journal of Climatology*, 18, p.p. 93-110.
- [23] Dalezios, N.R., Loukas, A., Vasiliades, L., Liakopoulos, E. 2000. Severity-Duration-Frequency Analysis of Droughts and Wet Periods in Greece. *Hydrological Sciences Journal*. 45 (5), p.p. 665-680.

RAZVOJ KRIVIH SUŠE – POLOŽAJA – UČESTALOSTI U PARAMBIKULAM - ALIYAR BASENU, TAMIL NADU, INDIJA

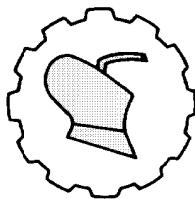
Muthiah Manikandan, Dhanapal Tamilmani

*Poljoprivredni univerzitet Tamil Nadu, Fakultet za poljoprivrednu tehniku,
Institut za konzervaciju zemljišta i voda,
Coimbatore, Tamil Nadu, Indija*

Sažetak: Procena i karakterizacija regionalnih suša daju korisne informacije za održivo planiranje i upravljanje vodenim resursima. U ovom istraživanju primenjen je Standardizovani indeks padavina (*SPI*), kao najšire primenjeni indeks suše zasnovan na padavinama, za ispitivanje vremenskih karakteristika, prostornog oblika i učestalosti suše u basenu Parambikulam-Aliyar, Tamil Nadu. Za ovu svrhu basen je podeljen na 97 mrežnih ćelija dimenzija 5×5 km, tako da svaka ćelija odgovara približno 1.03% ukupne površine. Mesečne padavine u mreži razvijene su tehnikom prostorne interpolacije uz pomoć *GIS*-a u svakoj tački mreže korišćenjem podataka o mesečnim padavinama za period od 40 godina (1972-2011) iz 28 mernih stanica. Regionalne reprezentativne *SPI* vrednosti izračunate iz prostorno prosečnih vrednosti padavina korišćene su za karakterizaciju vremenskih varijacija suše. Krive suše-prostornog položaja-učestalosti (*SAF* krive) su konstruisane korišćenjem mrežnih *SPI* vrednosti za procenu jačine suše i prostornog položaja u odnosu na povratni period, tako da se opišu i karakterišu prostorni i povratni oblici suše. Analiza *SPI* vrednosti pokazuje da su basen pogodile jake suše 1970-tih, 1980-tih i 2000-tih. Razvijene *SAF* krive mogu se koristiti za razradu plana pripravnosti u sušnim periodima u regionu i planiranje održivog upravljanja vodenim resursima u basenu.

Ključne reči: *distribucija ekstremnih vrednosti tipa I, GIS, padavine, SAF krive, SPI, masena kumulativna godišnja suša*

Prijavljen: 23.07.2013.
Submitted:
Ispravljen:
Revised:
Prihvaćen: 14.09.2013.
Accepted:



UDK: 631 (059)

Originalni naučni rad
Original scientific paper

DEVELOPMENT OF AIR ASSISTED SPRAYER FOR GREENHOUSE FLORICULTURE CROPS

**Sachin Vilas Wandkar*, Shailendra Mohan Mathur,
Babasaheb Sukhdeo Gholap, Pravin Prakash Jadhav**

*Maharana Pratap University of Agriculture and Technology,
College of Technology and Engineering,
Department of Farm Machinery and Power Engineering Udaipur, Rajasthan, India*

Abstract: Floriculture is one of the major sectors in Indian agriculture. Main threats to floriculture production are insects, pests and diseases. Therefore, a motor operated air assisted sprayer was developed for greenhouse floricultural crops. A tapered air sleeve was designed and made with fiber reinforced PVC material in order to get uniform air velocity at each outlet. The boom was developed to support air sleeve and nozzles. The centrifugal blower of capacity $0.40 \text{ m}^3 \cdot \text{s}^{-1}$ was used on the system to produce air stream in the sleeves. A horizontal triplex power pump of $16 \text{ l} \cdot \text{min}^{-1}$ capacity was used to create necessary pressure in the nozzles. Blower and pump were operated by 3.73 kW electric motor. The whole assembly of the sprayer was mounted on the trolley. The performance of developed sprayer was evaluated in the laboratory to study the effect of different air velocity ($9, 12, 16$ and $20 \text{ m} \cdot \text{s}^{-1}$) and pump discharge ($2.5, 4.5, 7$ and $9 \text{ l} \cdot \text{min}^{-1}$) levels on droplet size, droplet density and uniformity coefficient at six different positions of artificial plant canopy. The optimum results of droplet size ($100\text{-}150 \mu\text{m}$), droplet density ($25\text{-}35$ droplets per cm^2) and uniformity coefficient (near unity) at all plant positions were observed for air velocity of $20 \text{ m} \cdot \text{s}^{-1}$ and pump discharge of $2.5 \text{ l} \cdot \text{min}^{-1}$.

Key words: *greenhouse, floriculture, air assisted sprayer, droplet size, droplet density*

* Corresponding author. E-mail: sachinwandkar85@gmail.com

Authors sincerely thank to Shree Sharad Patel, the Managing Director, ASPEE Agricultural Research and Development Foundation, Mumbai (India) for providing all necessary facilities and funds for this research work.

INTRODUCTION

Floriculture in India is being viewed as a high growth Industry. Commercial floriculture is becoming important from the export angle. Indian floriculture industry has been shifting from traditional flowers to cut flowers for export purposes. According to a report of the Agricultural and Processed Food Products Export Development Authority (APEDA), Government of India, the total area under flower crops was estimated around 34,000 hectares, which included 24,000 hectares under traditional flowers such as marigold, jasmine, aster, rose, chrysanthemum, tuberose and 10,000 hectares under modern flowers like carnation, rose, gerbera, gladiolous, anthurium. Returns from floricultural products were estimated at Rs. 205 Crores, which included Rs. 105 Crores from traditional and Rs. 100 Crores from modern flowers [13].

Floricultural crops are more susceptible to pests and diseases during their flowering stages. Generally, chemical pesticides are used for controlling pests and diseases. Traditionally farmers use the knapsack sprayer for the application of pesticides. But, the manually operated knapsack sprayer has a number of limitations: it is labor intensive, have low application accuracy and require serious safety precautions. Performance depends on skill of operator; manual application often results in an uneven distribution of the pesticide.

Air assisted spraying is considered as one of the better pesticide application technique. The air assisted spraying system contributes towards: reduction in spray drift and loss on the ground, an increase in the agrochemical deposits levels and coverage rate of the abaxial surface leaves, improvement in the penetration of the spray droplets into the canopy as well as enabling a reduction in both dosage and in application volume [7]. Incorporation of air assistance in the spraying system improves the deposition uniformity in the entire plant canopy structure, spray deposition on the lower part of the plant leaves, where most pests harbor [3]. The air sleeve boom spraying technology is based on air assisted spraying. This system essentially consists of a blower, nozzles, pump and sleeve or duct. The sleeves, made of PVC material, are inflated with the air mass generated by blower. The sleeve has number of holes at bottom for delivering air. The spray droplets produced by nozzles are transported to a target through a stream of air coming out of sleeve orifices which results in better control over spray droplets and deposition [6].

Shahare *et al.* [8, 9] developed a tractor operated air sleeve boom sprayer for cotton crop for better deposition of pesticide throughout the canopy and evaluated its performance in the field for cotton crop with findings that higher air velocity improves the deposition of pesticide on whole canopy of cotton crop. Sirohi *et al.* [10] developed an air-assisted hydraulic sprayer for improved deposition of pesticides in different canopy structures of vegetable crops. Bauer and Raetano [1] evaluated the effects from air speed variation on spraying sleeve boom and conclude that the use of air assistance resulted in better deposit levels on the abaxial surface of the folioles positioned in the lower portion of the plants.

Therefore, efforts have been made to develop an air assisted sprayer for pesticide applications in floricultural crops and the performance of the sprayer was evaluated in the laboratory to study the effect of different air velocity and pump discharge levels on droplet size, droplet density and uniformity coefficient at different positions on plant.

MATERIAL AND METHODS

Development of air assisted sprayer

The basic principle of the system is the replacement of air within the canopy of plant with sprays laden air. The droplets must travel in and around plant canopy in order to cover as many leaves as possible. Efforts were made to develop an air delivery system considering the canopy structure of the greenhouse floriculture crops mainly rose and gerbera. The major components of the sleeve boom spraying system were the blower, sleeve, spraying nozzles and pump. A trolley was fabricated to support whole assembly over it. The blower generated the required volume of air and directed the flow into the sleeve. Air from the blower was conveyed and distributed through two sleeves with multiple orifices to achieve an airflow pattern covering the canopy. The sleeve was designed to produce an air curtain along the length of boom and to distribute air uniformly. The boom was made to support the air sleeve and hydraulic nozzles for a final delivery of air-pesticide mixture onto the target. The details of different components of the sprayer are given below.

Blower

The centrifugal blower of existing mist blower having capacity of $0.40 \text{ m}^3 \cdot \text{s}^{-1}$ was used on the system to create air pressure in the sleeves attached on the either sides of the blower at its outlet. It consists of casing and impeller. Specifications of casing and impeller are given below.

Blower casing. It is fabricated from high density polyethylene plastic. Blower casing was connected to lance assembly to which sleeves were connected on its either sides. Lance assembly was made of PVC pipe. The specifications of the blower casing and lance assembly are shown in Fig. 1.

Blower impeller. Centrifugal impeller was used to provide high velocity air to transmit spray droplets to intended target effectively. The specifications of the impeller are given below.

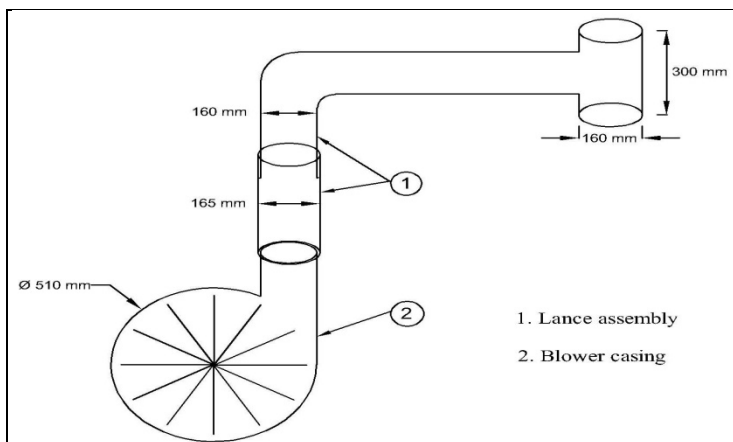


Figure 1. Blower casing with lance assembly

Material	: Stainless steel	No. of blades	: 48
Type of blade	: Forward curved	Blade inlet angle	: 16°
Blade outlet angle	: 160°	Inner diameter	: 220 mm
Outer diameter	: 300 mm	Width of impeller	: 140 mm

Air sleeve

A horizontal flexible air duct was designed to generate an air curtain with a uniform air velocity profile throughout the length of boom by tapering the duct (sleeve) towards the close end.

Let ' L ' be the length of sleeve equal to swath width and ' D_o ' its diameter at the inlet (at the exit of blower) whereas the other end of sleeve is closed. It has ' n ' number of orifices of uniform cross section throughout its length (Fig. 2). The air is blown into the duct from the blower and forced out through the orifices. As it is required to have uniform distribution of air along the duct, it was decided to taper the duct so that vertical air velocity will remain constant along its length [4]. Thus, to maintain uniform distribution of air along the length of the duct, the diameter of the duct at different cross sections (D_x) was determined as shown below. Let D_o , diameter of duct at $X = 0$ and $D_o = 0$ at $X = L_S$ (Fig. 2).

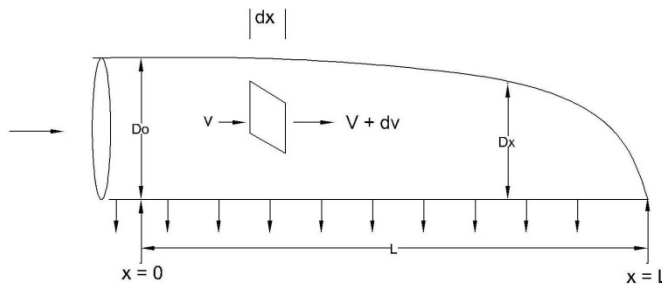


Figure 2. Tapered air duct

The air flow at the duct entrance can be calculated from continuity equation as:

$$Q = A \cdot V \quad (1)$$

where:

Q [$\text{m}^3 \cdot \text{s}^{-1}$] - air flow at the duct entrance,

A [m^2] - area of cross-section,

V [$\text{m} \cdot \text{s}^{-1}$] - air velocity.

The cross sectional area, at $X = 0$ and diameter D_o , can be found as

$$A = \frac{\pi}{4} \cdot D_o^2 \quad (2)$$

where:

π [-] - constant (3.14),

D_o [m] - diameter of duct at $x = 0$.

The total volume entering the duct is equal to the total discharge throughout its length. Therefore,

$$Q = Q_d \cdot L \quad (3)$$

where:

Q_d [$\text{m}^3 \cdot \text{s}^{-1}$] - total discharge from duct throughout the length of the duct,

L [m] - total length of the duct.

The quantity of air passing the section 'X' is calculated as:

$$Q_x = A_x \cdot V \quad (4)$$

where,

Q_x [$\text{m}^3 \cdot \text{s}^{-1}$] - total discharge through the section X,

A_x [m^2] - cross sectional area at section X.

The volume of air passing the section X is equal to the total discharge through the remaining length of duct. Therefore,

$$Q_x = Q_d \cdot (L - X) \quad (5)$$

Therefore, equations (1) and (5) can be written as:

$$Q_d \cdot L = V \cdot \pi / 4 \cdot D_o^2 \quad (6)$$

and:

$$Q_d \cdot (L - X) = V \cdot \pi / 4 \cdot D_x^2 \quad (7)$$

Thus, taking the ratio of the equations (5) and (6) we get:

$$\frac{Q_d \cdot L}{Q_d \cdot (L - X)} = \frac{V \cdot \pi / 4 \cdot D_o^2}{V \cdot \pi / 4 \cdot D_x^2}$$

which results into:

$$\frac{L}{L - X} = \frac{D_o^2}{D_x^2}$$

Therefore, the diameter of the duct at the section X can be found out as:

$$D_x^2 = D_o^2 \cdot \frac{L - X}{L} \Rightarrow D_x = D_o \cdot (1 - X / L)^{1/2} \quad (8)$$

where:

D_x [m] - diameter of duct at section X .

The above equation gives the relation between the length of the duct (air sleeve) and its diameter at different section tapering towards the close end. The diameter of sleeve obtained at different sections is shown in Fig. 3. By considering this two air sleeves of 160 mm in diameter at inlet matching to the outlet diameter of the blower and 2350 mm in length were sewed.

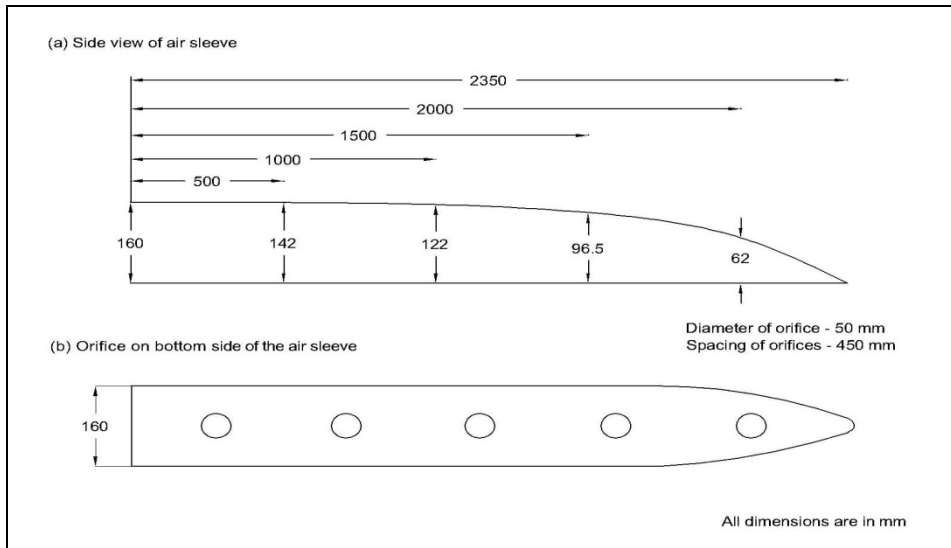


Figure 3. Diameter of sleeve obtained at different sections

Boom

The boom is the part of the sprayer which supports the air sleeve and nozzles. The boom is divided into two parts; center boom and side booms. Center boom was supported on M.S. angles fixed on the trolley and side booms were joined to center boom. It was decided to fabricate the boom from two circular M.S. pipes. One pipe on upper and another one on lower side joined each other with different slender member. The center boom was made up of 1.29 mm thick M.S. pipe of 20 mm outer diameter and side booms were made up of 1.29 mm thick M.S. pipe of 10 mm outer diameter. Six rings made up of M.S. rod of 10 mm diameter were provided on the boom to facilitate holding of flexible air duct. The total length of the boom was kept as 5 m. The nozzles were mounted on the boom along the length of horizontal air duct. A spring was provided at the joint of center boom and side booms to keep the boom straight during operation. The total boom assembly was rested on the M.S angles provided on trolley. The provision was made to facilitate the folding of boom along the length of trolley. The folding arrangement of boom is shown in Fig. 4.



Figure 4. Front view of the air assisted sprayer showing the folding arrangement of the boom

Trolley

The total assembly of the sprayer was supported on the trolley. Trolley was arbitrarily designed by considering row to row spacing of crops; it was decided to keep the width of trolley as 420 mm and its length as 1300 mm.

Trolley had four wheels of 200 mm diameter and one handle was provided at rear end for its operation. The trolley was fabricated from 38.1 mm \times 38.1 mm \times 5 mm section M.S. angle and it was provided with two M.S. angles at front side to support boom over it.

Power unit and nozzles

An electric motor of 5 HP was used as a power unit. It was used to drive the blower and pump. The power is transmitted to blower and pump through 'A' section of 'V' grooved belt and pulley (Fig. 5). Hollow cone plastic nozzles were selected for the study. In this study the spacing of nozzles was 450 mm as used in a conventional boom sprayer.

Accessories

A horizontal triplex power pump (HTP) was used to generate pressure on the spray fluid which worked in the oil bath and produced maximum discharge of 16 l·min⁻¹ at the pressure of 2.75×10^5 Pa. The pump had two deliveries and one bypass hose, pressure gauge, agitator and a pressure control valve to stabilize pressure. A high density polyethylene (HDPE) tank of 25 liter capacity was used for pesticide (Fig. 5). The bypass hose from HTP pump was connected to the tank at the bottom of the tank. The pressurized liquid from pump was brought to the nozzles with the help of hoses. The diameter of hose was 8 mm and made of heavy duty plastic.



Figure 5. Side view of sprayer showing pesticide tank, blower, electric motor and pump

Performance evaluation of the air assisted sprayer

The laboratory experiments were conducted to study sprayer performance with different air velocities and pump discharges for droplet size, droplet density and uniformity coefficient at different plant positions. Air velocities of $9 \text{ m}\cdot\text{s}^{-1}$, $12 \text{ m}\cdot\text{s}^{-1}$, $16 \text{ m}\cdot\text{s}^{-1}$ and $20 \text{ m}\cdot\text{s}^{-1}$; and pump discharges of $2.5 \text{ l}\cdot\text{min}^{-1}$, $4.5 \text{ l}\cdot\text{min}^{-1}$, $7 \text{ l}\cdot\text{min}^{-1}$ and $9 \text{ l}\cdot\text{min}^{-1}$ were used. The different air velocities were obtained by changing the rotations per minute (RPM) of blower by using different combinations of driver and driven pulleys and pump discharge was obtained by using different nozzles having the discharge rates of 0.25 , 0.45 , 0.70 and $0.90 \text{ l}\cdot\text{min}^{-1}$. An artificial plant canopies were prepared with hibiscus plant spaced at recommended spacing of 300 mm . The spraying height was kept as 800 mm during the experiments. To facilitate the evaluation of spray penetration into the canopy of plant, glossy papers of size $44 \times 44 \text{ mm}$ were stapled onto the leaf in different plant locations, i.e. top position of plant canopy, upper leaf surface (TU); top position of plant canopy, lower leaf surface (TL); middle position of plant canopy, upper leaf surface (MU); middle position of plant canopy, lower leaf surface (ML); bottom position of plant canopy, upper leaf surface (BU) and bottom position of plant canopy, lower leaf surface (BL). The sprayer was operated at speed of 1 km/hr for spraying in laboratory. Royal blue indigo dye was mixed with water to prepare coloured spray solution. During the experiments impression of spray solution was collected on glossy papers and then the glossy papers were taken for further analysis using a droplet image analyzer. Droplet size and droplet density were measured by using Image-Pro software.

RESULTS AND DISCUSSION

The developed air assisted sprayer was operated at four air velocities and four pump discharges in the laboratory and its performance was studied for droplet size, droplet density and uniformity coefficient at various locations in artificial plant canopy.

Effect of air velocity on droplet size, droplet density and uniformity coefficient

Analysis of variance (Tab. 1, Tab. 2 and Tab. 3) showed that the air velocity had a significant effect on droplet size, droplet density and uniformity coefficient. The effect of air velocity on droplet size has been plotted in Fig. 6. It indicates that droplet size decreased with increase in air velocity at top, middle and bottom position of plant and on upper and lower leaf surface. The maximum droplet size was observed with air velocity of $9 \text{ m}\cdot\text{s}^{-1}$ and minimum droplet size was observed as an effect of air velocity of $20 \text{ m}\cdot\text{s}^{-1}$ at all plant positions. The values of droplet size observed as an effect of air velocity of $20 \text{ m}\cdot\text{s}^{-1}$ at top, middle and bottom position of plant and on upper and lower leaf surface was within the range of $100 \mu\text{m}$ to $150 \mu\text{m}$, which is very effective for control of pests in most of the crops [2, 5, 11, 12].

Table 1. ANOVA showing the effect of air velocity and pump discharge on droplet size

Source	DF	Sum of Squares	Mean Square	F	SE	CD
Replications	95	68718.73	723.35506	79.294**	1.744	6.417
Air velocity	3	15336.4	5112.13	560.388**	0.356	1.310
Pump discharge	3	27119	9039.68	990.923**	0.356	1.310
Canopy positions	5	21082.3	4216.46	462.205**	0.436	1.604
Air velocity \times Pump discharge	9	597.809	66.4233	7.281**	0.712	2.620
Air velocity \times Canopy positions	15	995.294	66.3529	7.274**	0.872	3.208
Pump discharge \times Canopy positions	15	3156.09	210.406	23.065**	0.872	3.208
Air velocity \times Pump discharge \times Canopy positions	45	3834.11	85.2024	9.340**	1.744	6.417
Error	192	1751.52	9.12249			

** Significant at 1 % level

GM = 146.400, CV = 2.06

Table 2. ANOVA showing the effect of air velocity and pump discharge on droplet density

Source	DF	Sum of Squares	Mean Square	F	SE	CD
Replications	95	6412	67.494737	67.495**	0.577	2.124
Air velocity	3	1780.75	593.583	593.583**	0.118	0.434
Pump discharge	3	2178.25	726.083	726.083**	0.118	0.434
Canopy positions	5	2329.75	465.95	465.950**	0.144	0.531
Air velocity \times Pump discharge	9	422.625	46.9583	46.958**	0.236	0.867
Air velocity \times Canopy positions	15	41	2.73333	2.733**	0.289	1.062
Pump discharge \times Canopy positions	15	44	2.93333	2.933**	0.289	1.062
Air velocity \times Pump discharge \times Canopy positions	45	295.875	6.575	6.575**	0.577	2.124
Error	192	192	1			

** Significant at 1 % level

GM = 22.646 CV = 4.42

The effect of air velocity on droplet density is plotted in Fig. 7. The trend of the curve showed that the droplet density increased with increase in air velocity. This trend

was found similar in almost all positions of the plant. The maximum droplet density obtained through the plant canopy on the upper leaf surface on target plant was at $20 \text{ m}\cdot\text{s}^{-1}$ air velocity and minimum mean droplet density was observed with air velocity of $9 \text{ m}\cdot\text{s}^{-1}$.

Table 3. ANOVA showing the effect of air velocity and pump discharge on uniformity coefficient

Source	DF	Sum of Squares	Mean Square	F	SE	CD
Replications	95	7.9546075	0.083732711	11.214**	0.050	0.184
Air velocity	3	3.61837	1.20612	161.527**	0.010	0.037
Pump discharge	3	1.25115	0.41705	55.852**	0.010	0.037
Canopy positions	5	2.07801	0.415601	55.658**	0.012	0.046
Air velocity \times Pump discharge	9	0.715272	0.0794747	10.643**	0.020	0.075
Air velocity \times Canopy positions	15	0.664458	0.0442972	5.932**	0.025	0.092
Pump discharge \times Canopy positions	15	0.221771	0.0147848	1.980*	0.025	0.092
Air velocity \times Pump discharge \times Canopy positions	45	3.08083	0.0684629	9.169**	0.050	0.184
Error	192	1.43367	0.00746701			

*, ** Significant at 5 % and 1 % level respectively

GM = 1.449 CV = 5.96

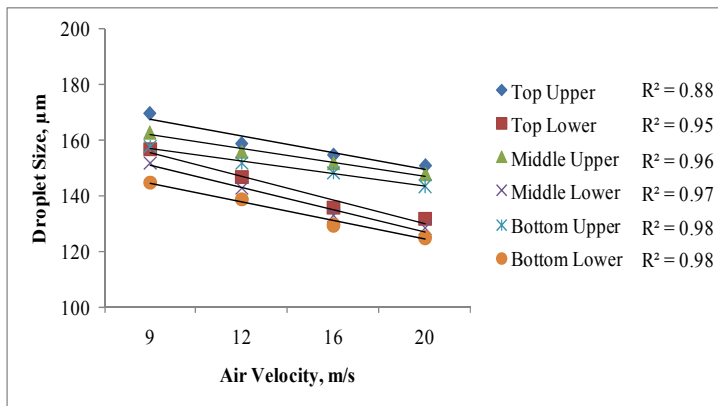


Figure 6. Effect of air velocity on droplet size at different plant positions

The trend of the curve (Fig. 8) showed that uniformity coefficient decreased with increase in air velocity from $9 \text{ m}\cdot\text{s}^{-1}$ to $20 \text{ m}\cdot\text{s}^{-1}$. Uniformity coefficient observed as an effect of air velocity of $20 \text{ m}\cdot\text{s}^{-1}$ was within the recommended range. The reason behind this phenomenon was that the increased air velocity reduces the droplet size and increases droplet density throughout the plant canopy resulting in uniform distribution throughout the plant canopy.

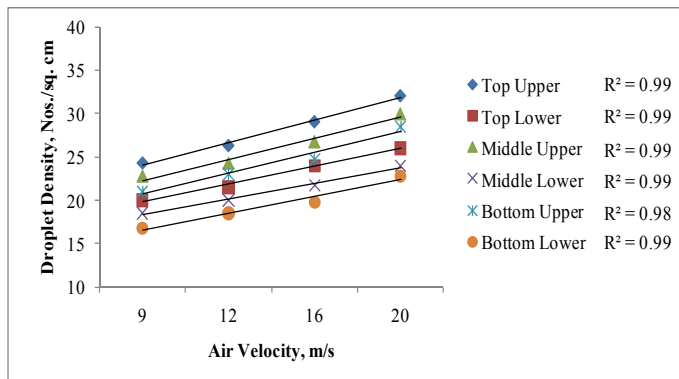


Figure 7. Effect of air velocity on droplet density at different plant positions

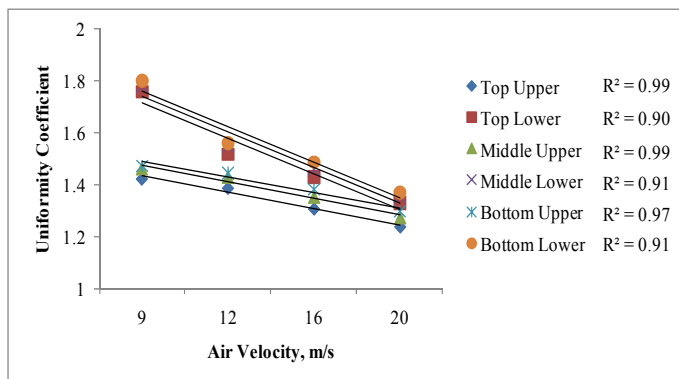


Figure 8. Effect of air velocity on uniformity coefficient at different plant positions

Effect of pump discharge on droplet size, droplet density and uniformity coefficient

The pump discharge was set at $2.5 \text{ l}\cdot\text{min}^{-1}$, $4.5 \text{ l}\cdot\text{min}^{-1}$, $7 \text{ l}\cdot\text{min}^{-1}$ and $9 \text{ l}\cdot\text{min}^{-1}$ and the effect on deposition of droplets at six different plant positions was studied. Analysis of variance (Tab. 1, Tab. 2 and Tab. 3) showed that the pump discharge had a significant effect on droplet size, droplet density and uniformity coefficient. Fig. 9 shows that the droplet size observed as an effect of pump discharge of $2.5 \text{ l}\cdot\text{min}^{-1}$ was within the recommended range. These values are significantly lower than the values of droplet size obtained as an effect of other pump discharge levels at all plant positions. The droplet size was found to decrease from top to bottom position of plant. Higher values of droplet size were observed at upper leaf surface than at lower leaf surface.

The effect of pump discharge on droplet density at different plant positions is shown in Fig. 10. The maximum droplet density was deposited at top position of the plant and upper leaf surface as an effect of pump discharge of $2.5 \text{ l}\cdot\text{min}^{-1}$. It was also observed that droplet density decreased with increase in pump discharge from $2.5 \text{ l}\cdot\text{min}^{-1}$ to $9 \text{ l}\cdot\text{min}^{-1}$ at all plant positions. The maximum mean droplet density was observed with pump discharge of $2.5 \text{ l}\cdot\text{min}^{-1}$.

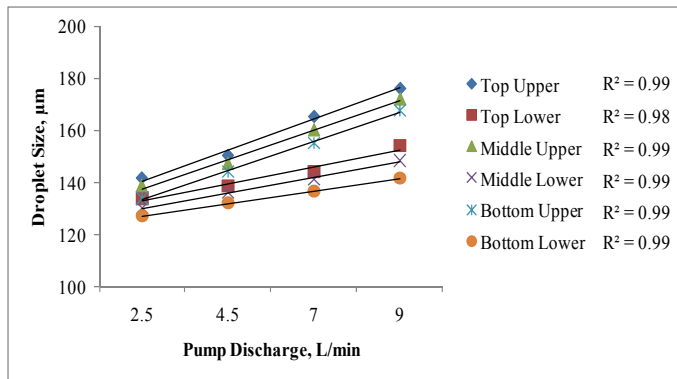


Figure 9. Effect of pump discharge on droplet size at different plant positions

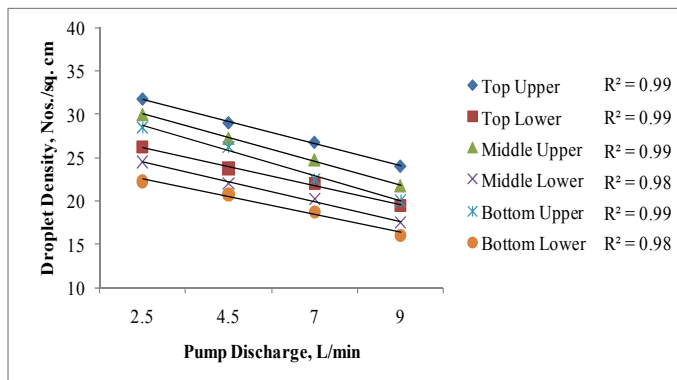


Figure 10. Effect of pump discharge on droplet density at different plant positions

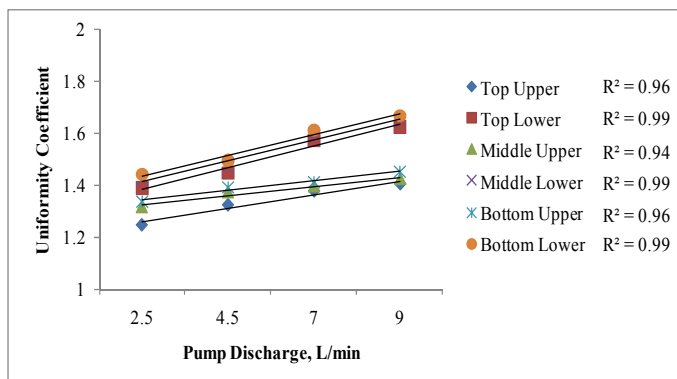


Figure 11. Effect of pump discharge on uniformity coefficient at different plant positions

The effect of pump discharge on uniformity coefficient is shown in Fig. 11. The trend of the curve showed that uniformity coefficient increased with increase in pump

discharge from 2.5 l·min⁻¹ to 9 l·min⁻¹. Uniformity coefficient observed as an effect of pump discharge of 2.5 l·min⁻¹ was within the recommended range.

The optimum droplet size, droplet density and uniformity coefficient were obtained at pump discharge of 2.5 l·min⁻¹.

Combined effect of air velocity and pump discharge on droplet size, droplet density and uniformity coefficient

Analysis of variance (Tab. 1, Tab. 2 and Tab. 3) showed that the combine effect of air velocity and pump discharge on droplet size, droplet density and uniformity coefficient was significant at 99 per cent level of confidence.

Multiple regression analysis was performed to develop a combined relationship among the air velocity, pump discharge and droplet size at all plant positions. The equation of following form was obtained:

$$S = a + b_1 \cdot V + b_2 \cdot Q + b_3 \cdot V \cdot Q \tag{9}$$

where:

- S [µm] - droplet size,
- V [m·s⁻¹] - air velocity,
- Q [l·min⁻¹] -pump discharge,
- a, b₁, b₂, b₃ - regression coefficients.

The regression coefficients for above equation are presented in Tab. 4.

Table 4. Regression coefficients for linear relationship of droplet size with air velocity and pump discharge

Plant Position		Regression Constant (a)	Regression Coefficient (b ₁)	Regression Coefficient (b ₂)	Regression Coefficient (b ₃)	R ²	Computed F
Top	Upper	163.208	-2.532	3.030	0.168	0.97	110.818**
	Lower	157.268	-2.247	3.161	0.011	0.95	67.362**
Middle	Upper	159.324	-2.424	2.397	0.192	0.98	216.577**
	Lower	159.477	-2.548	1.670	0.073	0.95	81.829**
Bottom	Upper	151.993	-2.193	2.728	0.167	0.99	374.028**
	Lower	158.119	-2.555	0.368	0.128	0.98	160.470**

** Significant at 1 % level

The equation shown below was obtained for the combined effect of air velocity and pump discharge at all plant positions on droplet density.

$$D = a + b_1 \cdot V + b_2 \cdot Q + b_3 \cdot V \cdot Q \tag{10}$$

where:

- D [Nos. per cm²] - droplet density.

The regression coefficients for above equation are presented in Tab. 5.

Table 5. Regression coefficients for linear relationship of droplet density with air velocity and pump discharge

Plant Position		Regression Constant (a)	Regression Coefficient (b ₁)	Regression Coefficient (b ₂)	Regression Coefficient (b ₃)	R ²	Computed F
Top	Upper	23.787	0.753	-1.033	-0.009	0.99	492.989**
	Lower	18.684	0.696	-0.645	-0.025	0.98	173.875**
Middle	Upper	24.513	0.598	-1.386	-0.011	0.99	309.773**
	Lower	18.734	0.578	-0.818	-0.015	0.97	136.328**
Bottom	Upper	21.763	0.717	-1.186	-0.010	0.99	274.980**
	Lower	15.387	0.664	-0.587	-0.025	0.97	145.275**

** Significant at 1 % level

Multiple regression analysis was also performed to study the combined effect of air velocity and pump discharge on uniformity coefficient at all plant positions. It gives following form of equation.

$$U = a + b_1 \cdot V + b_2 \cdot Q + b_3 \cdot V \cdot Q \quad (11)$$

where:

U [-] - uniformity coefficient,

The regression coefficients for above equation are presented in Tab. 6.

Table 6. Regression coefficients for linear relationship of uniformity coefficient with air velocity and pump discharge

Plant Position		Regression Constant (a)	Regression Coefficient (b ₁)	Regression Coefficient (b ₂)	Regression Coefficient (b ₃)	R ²	Computed F
Top	Upper	1.580	-0.026	0.001	0.002	0.97	113.848**
	Lower	1.796	-0.036	0.040	0.000	0.92	41.743**
Middle	Upper	1.685	-0.028	-0.011	0.002	0.96	93.519**
	Lower	1.805	-0.034	0.042	0.000	0.92	45.186**
Bottom	Upper	1.668	-0.025	-0.007	0.002	0.95	79.418**
	Lower	1.802	-0.032	0.046	0.000	0.92	43.717**

** Significant at 1 % level

CONCLUSIONS

On the basis of laboratory experiments following conclusions were drawn:

1. Droplet size and uniformity coefficient of developed air assisted sprayer was found to be decreased linearly with the increase in air velocity and decrease in pump discharge.
2. The droplet density was found to increase with increase in air velocity and decrease in pump discharge at all plant positions.
3. The recommended droplet size i.e. between 100 μm to 150 μm was obtained at air velocity of 20 m·s⁻¹ and pump discharge of 2.5 l·min⁻¹.
4. The developed air assisted sprayer exhibited better deposition efficiency with the air velocity of 20 m·s⁻¹ and pump discharge of 2.5 l·min⁻¹.

BIBLIOGRAPHY

- [1] Bauer, F.C., Raetano, C.G. 2003. Air-assisted boom sprayer and spray deposition on bean plants. *Scientia Agricola* (Piracicaba, Braz.) 60(2), 211-215.
- [2] Ennis, W.B. 1979. Introduction to crop protection. *A. Soc. Agro.*, Madison: 267-292.
- [3] Hadar, E. 1980. *Development criteria for air assisted ground crop sprayer*. Degania sprayer, Degania Bet, 15230, Israel, 23-26.
- [4] Hall, C.W. 1970. *Principle of air movement*. Drying of Farms Crops. Lyall Book Depot. Ludhiana.
- [5] Lake, J R., Taylor, W.A. 1974. Effect of the form of a deposit on the activity of Barban applied to *Avena Fatua* (L). *Weed Research*, 14: 13-18.
- [6] Manor, G.A., Hofman, O.R., Phishler, G., Epstin, Y., Nakash, T., Jakobi, M. 1989. Air stream facilitate application of cotton foliage treatment. *Transactions of ASAE* 32(1), 37-40.
- [7] Raetano, C.G. 2005. Air assistance in sleeve boom sprayers. Available through: www.jacto.com/PDF/white_papers/AirAssist_Sleeve_Boom_Sprayers.pdf [Accessed 20th Aug. 2013.]
- [8] Shahare, P.U., Thakre, S.K., Mathur, S.M., Bhatt, Y.C. 2010. Sleeve Boom Sprayer I: Design and Development of Tractor Mounted Sleeve Boom Sprayer for Cotton. *Agricultural Mechanization in Asia, Africa and Latin America*, 41(2), 48-54.
- [9] Shahare, P.U., Thakre, S.K., Mathur, S.M., Bhatt, Y.C. 2010. Sleeve Boom Sprayer II: Performance Evaluation of a Tractor Mounted Sleeve Boom Sprayer for Cotton. *Agricultural Mechanization in Asia, Africa and Latin America*, 41(3), 21-29.
- [10] Sirohi, N.P.S., Gupta, P., Mani, I. 2008. Development of air-assisted hydraulic sprayer for vegetable crops. *IE (I) Journal-AG*, 89.
- [11] Smith, D B., Burt, E.C., Lloyd, E.P. 1975. Selection of optimum sprays droplets sizes for Ball weevil and drift control. *J. Eco. Ento.*, 68: 415-417.
- [12] Willson, J.P., Hedden, O.K., Slesman, J.P. 1963. Spray droplet size as related to disease and insect control on row crops. *Ohio. Agric. Expt. Stn. Res. Bulletin*, USA: 945-50.
- [13] Yadawad, S.M., Kadapatti, R.G. 2011. Floriculture - present status and scope. *Gloden Research Thoughts*, 1(6), 1-4.

RAZVOJ VAZDUŠNOG RASPRSKIVAČA ZA ZAŠTITU CVEĆA U ZAŠTIĆENOM PROSTORU

**Sachin Vilas Wandkar, Shailendra Mohan Mathur,
Babasaheb Sukhdeo Gholap, Pravin Prakash Jadhav**

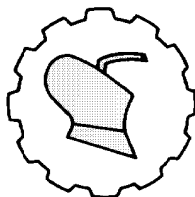
*Univerzitet za poljoprivredu i tehnologiju Maharana Pratap,
Fakultet za tehnologiju i inženjering, Institut za poljoprivredne mašine i pogonski
inženjering Udaipur, Rajasthan, India*

Sažetak: Cvečarstvo je jedna od glavnih oblasti indijske poljoprivrede. Ovu proizvodnju najviše ugrožavaju insekti, štetočine i bolesti. Zato je vazdušni rasprskivač na motorni pogon razvijen za zaštitu cvečarskih kultura u zaštićenom prostoru. Konusni usmerivač vazduha je konstruisan i napravljen od ojačanog PVC materijala kako bi dao

ujednačenu brzinu strujanja vazduha u svakom izlaznom otvoru. Nosač je razvijen kao oslonac za usmerivač vazduha i mlaznice. U sistem je ugrađen centrifugalni duvač kapaciteta $0.40 \text{ m}^3 \cdot \text{s}^{-1}$ koji stvara vazdušnu struju u usmerivačima. Horizontalna trostruka pogonska pumpa kapaciteta $16 \text{ l} \cdot \text{min}^{-1}$ je upotrebljena za obezbeđenje potrebnog pritiska u mlaznicama. Duvač i pumpa dobijaju pogon od elektromotora snage 3.73 kW. Ceo sklop rasprskivača postavljen je na kolica. Kod razvijenog rasprskivača u laboratoriji su ispitivani uticaji različitih brzina vazduha ($9, 12, 16$ i $20 \text{ m} \cdot \text{s}^{-1}$) i kapaciteta pumpe ($2.5, 4.5, 7$ i $9 \text{ l} \cdot \text{min}^{-1}$) na veličinu kapljica, gustinu kapljica i koeficijent ujednačenosti u šest različitih položaja veštačkog biljnog krova. Optimalni rezultati veličine kapljica ($100\text{-}150 \text{ }\mu\text{m}$), gustine kapljica ($25\text{-}35$ kapljica po cm^2) i koeficijenta ujednačenosti kod svih položaja biljke su dobijeni za brzinu vazduha od $20 \text{ m} \cdot \text{s}^{-1}$ i kapacitet pumpe od $2.5 \text{ l} \cdot \text{min}^{-1}$.

Ključne reči: zaštićeni prostor, cvečarstvo, vazdušni rasprskivač, veličina kapljice, gustina kapljica

Prijavljen: 26.06.2013.
Submitted:
Ispravljen: 10.08.2013
Revised:
Prihvaćen: 22.08.2013.
Accepted:



UDK: 631.312.021.3:621.791.3.004.67

Originalni naučni rad
Original scientific paper

THEORETICAL AND EXPERIMENTAL RESEARCH OF STRENGTH OF SOLDERED JOINTS (METAL OF SHARE – METAL CERAMICS)

Vladimir Goncharenko*

*Orel State Agrarian University, Faculty of Agrotechnics and Energy Supply,
Chair of Technology of Constructional Materials and Organization of Technical Service,
Orel, the Russian Federation*

Abstract. This article presents theoretical estimate of soldered strain and the obtained equivalent stresses distributions along the share length. It is suggested to estimate the soldered joints strength taking into consideration complicated character of stress condition taking place in the elements under loading. The main factors influencing soldered joints strength are defined in the article. Clearance gap between soldered samples, the overlapping area and groove depth are referred to these factors. The soldered samples tests on force of tear and shear showed that strength σ_B of soldered joint for metal of share JI65 and metal ceramic plate of alloy BK-8, corresponds to $\sigma_B = 119,6 \dots 120,6$ MPa at clearance gap 0,5...0,75 mm, that is proved with the theory.

Key words: *plow share, metal ceramic plate, hydrogen-oxygen flame, tangential and normal stresses, soldering, hardness, restoration.*

INTRODUCTION

In recent years to increase the wear resistance of operation bodies of tillage machines, particularly, plow shares metal ceramics plates are used. The problem arises at fixing the plates to share surface. Inadequate adhesive strength of today used glued connection decreases the share potential resource [1]. Researches are directed to the practicability and efficiency of operating surface formation by metal ceramics hard-face

* Corresponding author. E-mail: vovaniiii@rambler.ru

plates applying braze welding aiming at the plow share restoration and increasing its resource by 4-5 times.

Purpose is to estimate the hardness of soldered connection and the peculiarities of strain-stress state at soldering the metal ceramics plates to plow share blade using the hydrogen-oxygen flame.

MATERIALS AND METHODS

To test the soldering applying electrolyser “Energya-1,5 УХЛ4” we carried out the calculations of tangential τ and normal stresses σ_1 , σ_2 and the distribution of stresses along the length of the soldered connection, also we carried out laboratory tests of soldered pieces for cutting (τ_{cp}), tear (σ_e) using device ИР-500.

RESULTS AND DISCUSSION

To solve the problem of application of the electrolysers in the repair industry particularly for metal ceramics plates soldering to plow share is necessary to solve the following problems: to investigate the soldering mechanism with hydrogen-oxygen flame usage, to develop and optimize the technological solutions of realization of soldering with hydrogen-oxygen flame; to investigate the hardness of soldered connections for cutting and compression; to calculate economic efficiency of electrolysers application at plow share restoration.

At estimation of the soldered connections the complicated type of strain-stress state appearing in their elements at on-load was taken into consideration. The hardness of soldered connection is defined first of all by peculiarities of strain-stress state in soldered joint. That is why the main attention we pay to the analysis of stresses in soldered joints of overlapped soldered connections. If we suppose that stresses in a joint do not exceed the solder alloy elastic limit then for soldered connection it is possible to use the data obtained for glued and soldered connections in the limits of elasticity.

Strain-stress state in soldered joint in overlapped soldered connections is considered to be plain. Tangential τ and normal stresses σ_1 , σ_2 , are created in soldered joint under the influence of external forces. Tangential stresses according to [2-5] correspond to 0,5...0,6 from acceptable values of normal stresses:

$$\tau = (0,5...0,6)\sigma \quad (1)$$

where:

τ [MPa] - tangential stress,
 σ [MPa] - normal stress.

More than that, as the connecting elements are inset it is necessary to calculate the connections for tear by normal stresses.

Tangential stresses concentrators will be higher, the higher the ratio of elasticity modules of connected elements E_1 and E_2 to solder alloy elasticity module E .

Stresses, according to Sazhin (1964) [3], in overlapped soldered connections are distributed in the following way. In the connecting elements normal stresses σ_1 and σ_2 and the corresponding to them deformations appear ε_1 and ε_2 in the soldered joint only tangential stresses τ and the corresponding to them angular deformations J (Fig. 2) appear.

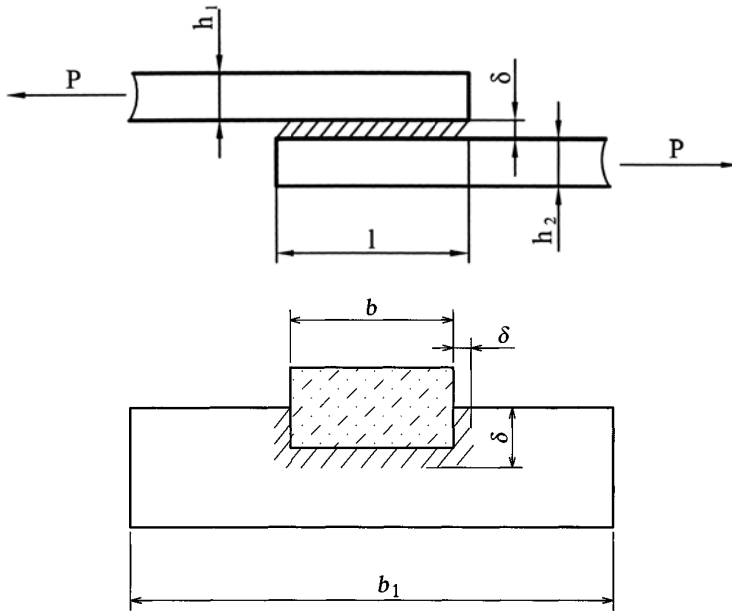


Figure 1. overlapped soldered connection:

l - lap length, mm; δ - soldered joint thickness, mm; h_1, h_2 - elements thickness, mm; P - force, H; b - lap width, mm; b_1 - piece length, mm

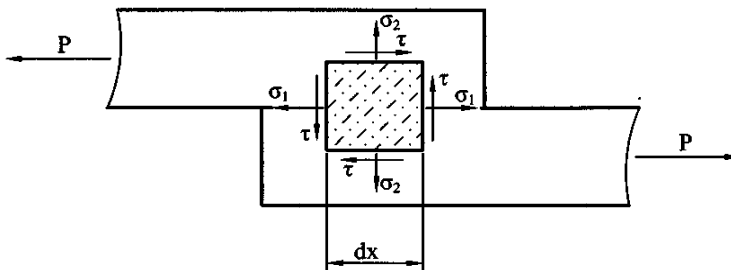


Figure 2. Type of the strain-stress state in overlapped soldered joint:

σ_1 - axial stress, MPa; σ_2 - tear stress, MPa; τ - tangential stress, MPa

$$\frac{\delta \cdot dj}{dx} = \varepsilon_2 - \varepsilon_1 \tag{2}$$

where:

δ [mm] - soldered joint thickness,

ε_1 [-] - axial deformation,

ε_2 [-] - tear deformation.

From equilibrium condition of soldered connection we obtain:

$$\frac{h_1 \cdot d\sigma_1}{dx} = -\tau \quad \frac{h_2 \cdot d\sigma_2}{dx} = \tau \quad (3)$$

$$\sigma_1 \cdot h_1 + \sigma_2 \cdot h_2 = P / b$$

where

σ_1 [MPa] - axial stress,

σ_2 [MPa] - tear stress,

h_1, h_2 [mm] - elements thickness,

P [N] - force,

b [mm] - lap width.

According to Guck's law:

$$\sigma_1 = E_1 \cdot \varepsilon_1$$

$$\sigma_2 = E_2 \cdot \varepsilon_2 \quad (4)$$

$$\tau = j \cdot G$$

where:

E_1, E_2 [10^9 Pa] - elasticity modules of joint elements related to elasticity module of alloy E,

j [-] - angular deformation,

G [MPa] - shear module of soldered seam

Solution to equations (4) – (6) gives:

$$\sigma_2'' - \alpha_{II} \cdot \sigma_2' + \beta_{II} \cdot \sigma_2 = 0 \quad (5)$$

where:

σ_2'' [MPa] - the second derived function of stresses,

σ_2' [MPa] - the first derived function of stresses,

$\alpha_{II} = \sqrt{\beta_{II} / \psi_{II}}$ [$1 \cdot \text{mm}^{-1}$] - ratio showing the changes of stiffness properties of metal of share ЛI-65 at its connection with soldered element (metal ceramics alloy BK-8),

$\beta_{II} = G / (\delta \cdot E_1 \cdot h_1)$ [$1 \cdot \text{mm}^{-2}$] - aspect ratio of shear stiffness and tension to joint width and soldered element (metal

ceramics alloy BK-8),
 $\psi_{II} = E_2 \cdot h_2 / (E_1 \cdot h_1 + E_2 \cdot h_2)$ [-] - Aspect ratio of resistance (stiffness) of elements in soldered connection.

Paying attention to the obtained aspect ratios solution to Eq. (5) allows the definition of stresses in arbitrary point of soldered connection depending on coordinate x .

$$\begin{cases} \sigma_1 = \sigma_{10} [1 - \psi_{II} \cdot (1 - ch(\alpha_{II} \cdot x))] - \frac{1 - \psi_{II} \cdot (1 - ch(\alpha_{II} \cdot l))}{sh(\alpha_{II} \cdot l) \cdot sh(\alpha_{II} \cdot x)} \\ \sigma_2 = \sigma_{2l} [\psi_{II} (1 - ch(\alpha_{II} \cdot x))] + \frac{1 - \psi_{II} \cdot (1 - ch(\alpha_{II} \cdot l))}{sh(\alpha_{II} \cdot l) \cdot sh(\alpha_{II} \cdot x)} \\ \tau = \tau_m \cdot \alpha_{II} \cdot l \cdot \frac{1 - \psi_{II} \cdot (1 - sh(\alpha_{II} \cdot l))}{sh(\alpha_{II} \cdot l) \cdot ch(\alpha_{II} \cdot x) - \psi_{II} \cdot sh(\alpha_{II} \cdot x)} \end{cases} \quad (6)$$

where:

l [mm] - lap length,

τ_m [MPa] - tangential stress of flow limit,

ch [-] - hyperbolic cosine of cut angle,

sh [-] - hyperbolic sine of cut angle.

We'll obtain: $\tau_{x=0} = \tau_{x=l} = 8 \cdot \tau_m$.

Stresses are connected with deformations by the following relations:

$$\varepsilon_1 = \frac{N_1 \cdot F_1}{E_1}$$

$$\varepsilon_2 = \frac{N_2 \cdot F_2}{E_2}$$

(7)

$$\varepsilon_y = \frac{\sigma_y}{E}$$

$$j = \frac{\tau}{G}$$

where:

N [N] - normal force undergoing deformations of extension or compression,

F [mm²] - cross-section area of soldered connection.

From equilibrium condition:

$$\begin{aligned} N'_1 &= -\tau \\ N'_2 &= \tau \end{aligned} \quad (8)$$

where:

N'_1, N'_2 [-] - the first area derivative.

From equation system (6) – (8):

$$\tau''' - \mu_1^2 \cdot \tau = 0 - \text{transcendent equation,} \quad (9)$$

where:

τ''' [MPa] - the third derivative from tangential stress,

$\mu_1 = \sqrt{8 \cdot G / (E_1 \cdot h_1 \cdot \delta)} = \sqrt{8 \cdot \beta_{II}}$ [$1 \cdot \text{mm}^{-1}$] - ratio taking into consideration the force distribution to soldered connection width.

Solution to equation (11) gives particular and total solution for center.

$$\tau = \eta_1 + \nu_1 \cdot \frac{ch\left(\frac{\mu_1}{x}\right)}{sh\left(\frac{\mu_1}{l}\right)} \quad (10)$$

where:

$\eta_1 = 3 \cdot N_0 / (8 \cdot \ell)$ [N/mm] - ratio taking into consideration the force distribution to unit length of soldered connection.

$$\nu_1 = \mu_1 \cdot \frac{N_0}{8}$$

where:

N_0 [$\text{kN} \cdot \text{mm}^{-1}$] - effort from extension of solid beam, having a form of soldered connection to width of element being soldered:

$$N_0 = P / b = 52,945 \text{ kN} \cdot \text{mm}^{-1}$$

The ratio analysis (6) shows that the most hard will be connections with straps that have $h_1 = 0,5 \cdot h_2$. Bearing capacity of this connections is by 1,31 times higher in comparison with the connection with one strap. Deviation of straps width in any side from optimal ratio can decrease bearing capacity of connection.

In analogy (6) to normal stresses σ_1 and σ_2 ratio deduced by Sazhin (1964) [3] the formula to calculate the elements with symmetric lap along tangential stresses is obtained.

$$\tau = \tau_m \left\{ 1 - \left[\frac{A_1}{\cos(2\pi x)} + A_2 \cdot \cos(4\pi x) \right] \right\} \quad (11)$$

where:

$$A_1 = \frac{a^2 + 53,2 \cdot a + 1000}{0,5 \cdot a^2 + 35,6 \cdot a + 542}$$

$$A_2 = \frac{9 \cdot a + 42}{0,5 \cdot a^2 + 35,6 \cdot a + 542}$$

[-] - ratios being obtained at approximation the obtained solutions by program complex Table Curve 2.0,

$$a = \frac{G \cdot l^2}{E_1 \cdot h_1 \cdot \delta}$$

[-] - ratio of joint resistance to metal cutting of share Л-65.

Polynomial functions in Fig. 3 are obtained.

All the described dependences show good reproducibility.

Calculations on the ratios for stresses obtained by different ways coordinate with each other with error to 5% that is a result of the correctness of the presented model.

Maximum stresses values obtained at the calculations on cutting and tear are 5 times less than stresses in the maximum loaded connection element that gives evidence of its high durability.

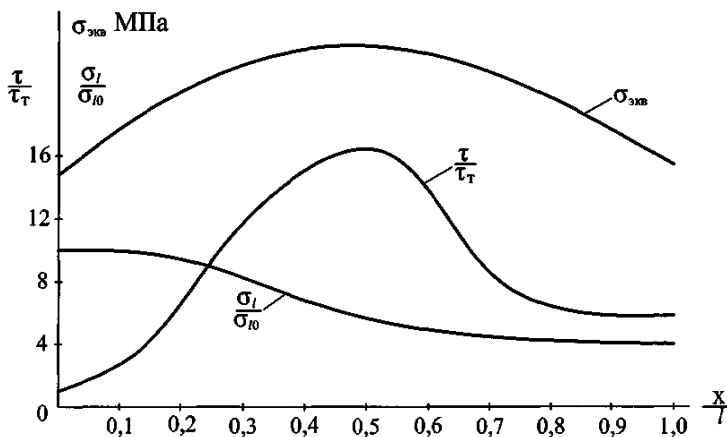


Figure 3. Distribution of the stresses influencing a share to the stresses corresponding to the material elastic ratio

For alloy BK-8 stresses values correspond to 115...120 MPa.

The calculation results and their checking according to III and IV failure theory show that the equivalent stresses in the given soldered connection reach 25...28 MPa, that is as mentioned above considerably lower than the ultimate values obtained at the experiment.

$$\text{III – failure theory } \sigma_{\text{эKB}} = \sqrt{\sigma^2 + 4 \cdot \tau^2} \leq [\sigma] = 120 \text{ MPa.}$$

$$\text{IV – failure theory } \sigma_{\text{эKB}} = \sqrt{\sigma^2 + 3 \cdot \tau^2} \leq [\sigma] = 115 \text{ MPa.}$$

The suggested type of connection can bear the calculated load excess by 4...5 times. That gives the evidence reliability of connection at dynamic effects with the dynamic response factor (k_{δ}) $k_{\delta} = 5$ and is a good result.

To proof the theoretical calculations the investigations of experimental determination of the soldered connections indicators according to the requirements of the state standard at using hydrogen-oxygen flame are carried out.

Results of experimental research

It is proved that with the overlapping area increase the joint strength increases too. The rational overlapping area is 288...320 mm² (Fig. 4, б). At overlapping area increase more than stated values the ultimate strength decreases. It corresponds to the dependence of solder flowing area from contact angle (Fig. 5). For example, for alloy BK-8 at contact angle decrease $\beta=16^{\circ}$ solder flowing area increases ($S=395 \text{ mm}^2$), but at increase of $\beta=25^{\circ}$ solder flowing area decreases ($S=316 \text{ mm}^2$). Such kind of dependence is typical for share steel Л-65. The obtained data corresponds to the necessary technical requirements.

At increase of slot depth strength increases (Fig. 4, c), the rational slot depth is 4...4,5 mm. The mentioned depth is provided with the ultimate share thickness.

The analysis of slot between soldered samples (Fig. 4, а) showed that the optimal strength of the soldered joint 123 MPa is obtained when slot is 1,0 mm. Rational slot between soldered samples is 0,5...0,75 mm. Thus the soldered joint strength will be 120...121 MPa. It is connected with the fact that when the slots are more than 0,8 mm the layered directed crystallization resulting in fraction formation is observed.

To define the influence of the main factors, influencing on the strength change σ_{B} , and also their mutual interaction complete factor test is done 2³. Investigated factors: x_1 – slot between soldered samples, δ , mm; x_2 – the overlapping area of metal ceramics plates, S , mm²; x_3 – slot depth, l , mm. Response function y is strength σ_{B} of soldered samples from metal ceramics (BK-8) and share steel (Л65), MPa.

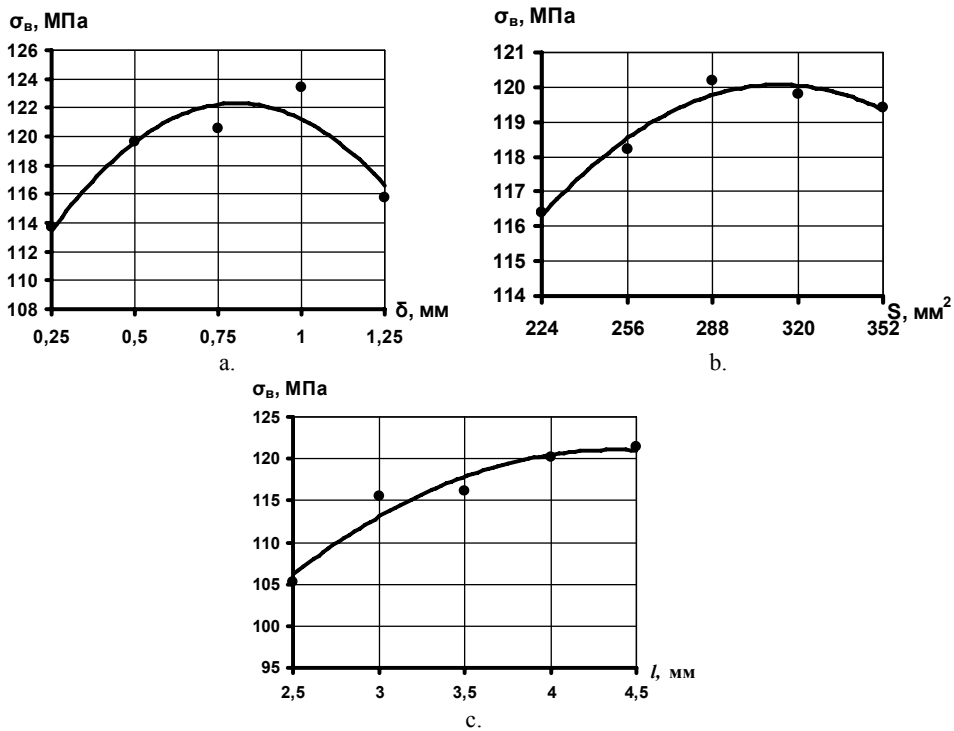


Figure 4. Dependence of strength σ_B of soldered sample joint from metal ceramics (BK-8) and share metal (Л165) from:
 a. slot between soldered samples δ , mm,
 b. solder flowing areas S , mm²,
 c. slot depth l , mm.

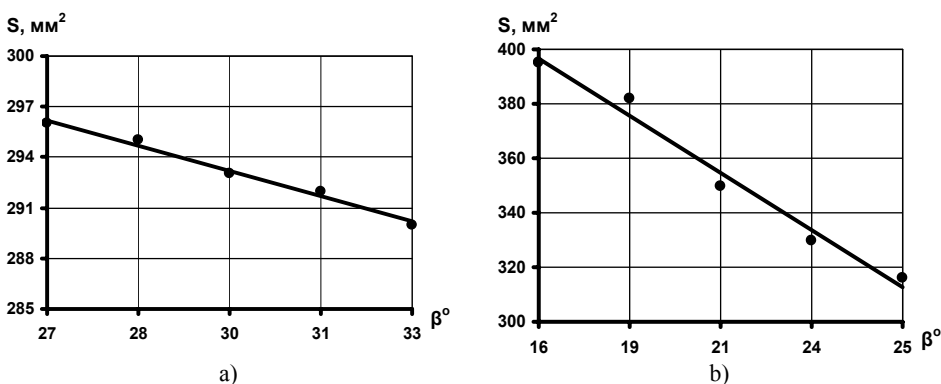


Figure 5. Dependence of solder flowing area from contact angle for materials from metal ceramics plate BK-8 (a) and share metal Л165 (b)

The investigated process is adequately described with the regression equation:

$$Y=41,5649+34,4625x_1+0,1767x_2+8,3407x_3-0,0107x_1x_2+3,3926x_1x_3+0,0162x_2x_3-22,97x_1^2-0,0004x_2^2-1,1493x_3^2 \quad (12)$$

The given equation rather precisely describes the factor influence depending on the slot between soldered samples, slot depth and plate overlapping area.

Regression coefficient calculations and other statistical indicators were carried out with computing aids usage, application soft Microsoft Excel. According to the analysis the change of soldered joint strength is maximally influenced with the slot between soldered samples and minimally with slot depth. The influence of plate overlapping area is inconsiderable.

It follows from the theory that the most dangerous section along the tangent stresses is midsection of soldered seam. Maximum normal stress at the boundary of soldered seam, according to the chart (Fig. 3), but the most dangerous will be the section of soldered seam where tangent and normal stresses are great. The results agree with theory because the practically obtained correlation is $x/l=0,45$, but in theory is $x/l=0,5$.

Overlapping of three charts (Fig. 4, a, b, c) with single scale of abscissas allows to chose the rational parameters of overlapping area, slot depth, slot between soldered samples using three maximum peak stresses. Matching them with Fig. 3 shows good reproducibility according to III and IV strength theory.

At the same time we determined: wetting along the contact angle and spreading radius; gap-filling with solder alloy; corrosive resistance; adhesive strength; we carried out the metallographic observations.

In Orel State Agrarian University soldered hydrogen-oxygen device "Energya-1,5 YXJ14" [6] was used at the investigation of the soldered process with application of hydrogen-oxygen flame.

CONCLUSIONS

1. As the result of the analysis the theoretical dependences of ultimate stress σ_B of soldered joints of samples from share metal (JI65) and metal-ceramics plate (BK-8) from clearance gap between soldered samples δ , from overlapping area of plate S and groove depth l are obtained. The most rational values of ultimate stress will be provided at $S=256...320 \text{ mm}^2$, $\delta=0,5...1,0 \text{ mm}$, $l=3,5...4,0 \text{ mm}$.

2. The suggested type of connection can bear the calculated load excess by 4...5 times. That gives the evidence reliability of connection at dynamic effects with the dynamic response factor $(k_\delta) k_\delta = 5$.

3. Adhesive strength of metal-ceramics plates on share metal obtained by means of soldering using hydrogen-oxygen flame depends on overlapping area, groove depth and clearance gap between soldered samples.

4. Soldered sample tests using hydrogen-oxygen flame on force of tear and shear demonstrated strength σ_B of soldered joint for metal of share JI65 and metal-ceramics plate was $\sigma_B = 119,6...120,6 \text{ MPa}$ at clearance gap 0,5...1,0 mm, that is proved with the theory.

5. The mentioned full 2-leveled factor experiment of type 2^3 , that was done in the local time limit demonstrates that the theoretical values of ultimate stress σ_B practically do not differ from experimental values.

6. The technology of plow share restoration by soldering using hydrogen-oxygen flame with high strength properties of soldered connections is developed. It allows reducing the production cost of restoration using cheap hydrogen-oxygen gas mixture being obtained as a result of water electrolyser and through utilization of metal ceramics plates in tool-producing industry.

BIBLIOGRAPHY

- [1] Goncharenko, V.V. 2007. *Technology of restoration and hardening of plow shares with metal ceramics plates (Технология восстановления и упрочнения лемехов плугов металлокерамическими пластинами)*. Dissertation of candidate of technical sciences. Faculty of Mechanization and Technical Service, Russian State Agrarian Extramural University, Moscow.. 158p.
- [2] Fesik, S.P. 1982. *Reference book of resistance of materials (Справочник по сопротивлению материалов)*. S.P. Fesik. – Kiev : Budivelnik. 290 p.
- [3] Sazhin, A.M. 1964. *Stress calculation in adhesive joints of metal plates at shear (Расчет напряжений в клеевых соединениях металлических пластин при сдвиге)*. Vestnik of Machinostroenye. №11. P.43-48.
- [4] Kuznetsov, O.A. 1987. *Hardness of soldered joints (Прочность паяных соединений)*. Machinostroenye, P.40-41.
- [5] Goncharenko, V.V. 2013. Stress calculation of soldered joints (metal ceramics) at plow shares restoration. *Proceedings of the union of scientists. Fifth conference „Energy efficiency and agricultural engineering”*. – Ruse, Bulgaria, 17-18 may, p.p. 539-543, ISSN 1311-9974
- [6] Goncharenko, V.V. 2009. Pat. 2344913 Russian Federation, МПК⁷ B23P6/00, B23K1/00, A01B15/04. *Way of plow share restoration (Способ восстановления лемехов плугов)*. Published 27.01.2009, Bulletin. №3. – 3 p.

TEORIJSKO I EKSPERIMENTALNO ISTRAŽIVANJE JAČINE LEMLJENIH SPOJEVA (METAL METAL – METAL KERAMIKA)

Vladimir Goncharenko

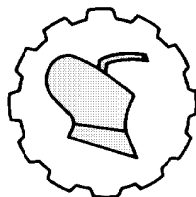
Državni Poljoprivredni Univerzitet Orel, Fakultet za poljoprivrednu tehniku i energetiku, Katedra za tehnologiju konstruktivnih materijala i organizaciju tehničkog servisa, Orel, Ruska Federacija

Sažetak. Ovaj rad predstavlja teorijsku procenu jačine lema i postignutih ekvivalentnih distribucija duž spoja. Predloženo je da se proceni jačina lemljenih spojeva uzimajući u obzir komplikovani karakter uslova kojima su elementi izloženi pod

opterećenjem. U radu su definisani osnovni faktori koji utiču na jačinu lemljenih spojeva. Zazor između lemljenih uzoraka, zona preklapanja i dubina su svrstani u ove faktore. Testovi lemljenih spojeva na sile kidanja i smicanja pokazali su da jačina σ_B lemljenog spoja metala Л165 i metal-keramičke ploče legure BK-8, odgovara intervalu $\sigma_B = 119,6 \dots 120,6$ MPa pri zazoru 0,5...0,75 mm, što je teorijski dokazano.

Ključne reči: *plužno smicanje, metal-keramička ploča, vodonično-kiseonični plamen, tangencijalna i normalna opterećenja, lemljenje, tvrdoća, obnova.*

Prijavljen: 13.06.2013.
Submitted:
Ispravljen: 10.07.2013.
Revised:
Prihvaćen: 28.07.2013.
Accepted:



UDK: 582.872

Originalni naučni rad
Original scientific paper

THIN LAYER DRYING KINETICS OF HENNA LEAVES

Dattatreya M. Kadam¹, Manoj Kumar Gupta^{2*}, Vaijayanta M. Kadam³

¹Central Institute of Post-Harvest Engineering and Technology (CIPHET),
PO: PAU campus, Ludhiana-141004 (Punjab), India

²Infosys Limited, Electronic City, Phase I, Bangalore, Karnataka, India

³Karnataka State Department of Horticulture, India

Abstract: Henna leaves are well known for their cosmetic agent with anti-carcinogenic, anti-inflammatory, analgesic and antipyretic properties. To investigate the effect of different drying conditions on kinetics of henna leaves, the laboratory models of tunnel dryer was employed and the leaves were dried at 40, 45, 50, 55, 60 and 65°C. Drying of henna leaves prominently occurred in falling rate period and drying was faster at higher temperature. Twelve thin layer-drying models were fitted to the experimental moisture ratio data. Among the mathematical models investigated, the Midilli-Kucuk model satisfactorily described the drying behavior with highest r^2 values. The effective moisture diffusivity (D_{eff}) of basil leaves increased with the increase in drying air temperature. Effective moisture diffusivity of henna leaves ranged from $2.24 \cdot 10^{-10}$ to $4.31 \cdot 10^{-10} \text{ m}^2 \cdot \text{s}^{-1}$ and activation energy was $27.03 \text{ kJ} \cdot \text{mol}^{-1}$. The dried leaves were ground to make the powder and the powder had average particle size of 0.2069 mm with a fineness modulus of 1.3685.

Key words: henna, mathematical modeling, drying, moisture diffusivity, activation energy

INTRODUCTION

Henna (*Lawsonia inermis*, syn. *L. alba*) is native to tropical and subtropical regions of Africa, southern Asia, and northern Australia in semi-arid zones. The plant is found all over the world including Australia, the Mediterranean, Africa, and in Southern United States. The variety of henna plant varies from region to region and different plants have

* Corresponding author. E-mail: mnjoff@gmail.com

different coloring properties and the color of the powder also varies. Henna is a tall shrub or small tree 2 to 6 m high. It is glabrous, multi-branched with spine tipped branch lets. Henna is commercially cultivated in western India, Pakistan, Iran, Yemen, Morocco and Sudan.

Herbal medicines are in great demand in the developed as well as developing countries for primary healthcare because of their wide biological and medicinal activities, higher safety margins and less cost. Henna has been used for thousands of years for its medicinal properties and cosmetic properties. Henna is worldwide known as cosmetic agent with anti-carcinogenic, anti-inflammatory, analgesic and antipyretic properties [1]. Alcoholic extracts of henna, leaves showed mild antibacterial activity against, *Micrococcus pyrogenes var Aureus* and *Eschericia coli* [2]. The tannin and the gallic acid seem to have a complimentary beneficial effect. Several studies have been dedicated to explore the medicinal value of henna leaves. Henna leaves have been effective in management of burn wound infections [3], and henna leaves extract can be used as sources of natural antioxidants [1]. Researchers studied the stability of henna paste for skin decoration, tattooing and hair dyeing [4]. Researchers have also applied henna dye on wool fabric to impart antimicrobial characteristics and found the treated fabrics were antimicrobial [5, 6]. Henna produces a red-orange dye molecule called laws one. This molecule has an affinity for bonding with protein, and thus has been used to dye skin, hair, fingernails, leather, silk and wool. The color produced by pure natural henna ranges from orange to red, to black cherry and to near black color. The color of henna powder depends not only on the variety of the plant, storage conditions, pasting method but also on the drying method and dying process parameters. Most of the henna is traded in powder form after drying and grinding of dried leaves. So, drying of the leaves is an interesting area of the research to ascertain optimized drying conditions of the leaves. The presented study evaluates drying kinetics of henna leaves.

THEORETICAL CONSIDERATIONS

Mathematical formulation

The moisture contents of henna leaves during the experiments were expressed in dimensionless form as moisture ratios (MR) with the help of the following equation [7-12].

$$MR = \frac{M - M_e}{M_0 - M_e} \quad (1)$$

where:

M [%] - mean henna leaves moisture content,

M_0 [%] - initial moisture content,

M_e [%] - equilibrium moisture content.

M_e value is very small compared to those of M_0 and M . So, the M_e value can be neglected and the moisture ratio can be simplified and can be expressed as [10-15]:

$$MR = \frac{M}{M_0} \quad (2)$$

Table 1. Thin layer drying models considered for the study

S.No.	Name of the model	Model equation
1	Newton	$MR = \text{Exp}(-k * t)$
2	Page	$MR = \text{Exp}(-k * t ** n)$
3	Modified Page 1	$MR = \text{Exp}(-(k * t) ** n)$
4	Henderson and Pabis	$MR = a * \text{Exp}(-k * t)$
5	Logarithmic	$MR = a * \text{Exp}(-k * t) + c$
6	Two-term	$MR = a * \text{Exp}(-k * t) + b * \text{Exp}(-n * t)$
7	Two-term exponential	$MR = a * \text{Exp}(-k * t) + (1-a) * \text{Exp}(-k * a * t)$
8	Wang and singh	$MR = 1 + (a * t) + (b * (t ** 2))$
9	Diffusion approach	$MR = a * \text{Exp}(-k * t) + (1-a) * \text{Exp}(-k * b * t)$
10	Modified Henderson and Pabis	$MR = a * \text{Exp}(-k * t) + b * \text{Exp}(-n * t) + c * \text{Exp}(-m * t)$
11	Verma <i>et al.</i>	$MR = a * \text{Exp}(-k * t) + (1-a) * \text{Exp}(-m * t)$
12	Midilli-Kucuk	$MR = a * \text{Exp}(-k * (t ** n)) + b * t$

Data were fit to 12 thin layer drying models to ascertain the best model which can describe the drying behavior of the product (Table 1). To determine the best fit model, non-linear regression analysis was done using the STATISTICA. The coefficient of determination, r^2 , was one of the primary and main criteria for selecting the best equation to account for variation in the drying curves of dried samples [8, 16, 17]. In addition to coefficient of determination, the goodness of fit was determined by the statistical parameters such as reduced chi-square (χ^2), mean bias error (MBE), and root mean square error (RMSE). The best fit was evaluated on the basis of highest r^2 value, and lowest values of χ^2 , MBE and RMSE [17-20]. The above parameters were calculated as per the following relationships:

$$\chi^2 = \frac{\sum_{i=1}^N (MR_{\text{exp}.i} - MR_{\text{pre}.i})^2}{N - z} \quad (3)$$

$$MBE = \frac{1}{N} \sum_{i=1}^N (MR_{\text{pre}.i} - MR_{\text{exp}.i}) \quad (4)$$

$$RMSE = \left[\frac{1}{N} \sum_{i=1}^N (MR_{\text{pre}.i} - MR_{\text{exp}.i})^2 \right]^{1/2} \quad (5)$$

Effective moisture diffusivity (D_{eff})

Fick's diffusion equation for particles with slab geometry was used for calculation of effective moisture diffusivity. The samples were considered of slab geometry [21]. The diffusion equation can be expressed as [22]:

$$MR = \frac{8}{\pi^2} \exp\left(\frac{-\pi^2 D_{eff} t}{4 L^2}\right) \quad (6)$$

Equation (6) can be rewritten as:

$$\ln MR = D_{eff} k_o + \ln \frac{8}{\pi^2} \quad (7)$$

where:

k_o [-] - slope,

is calculated by plotting $\ln(MR)$ versus time according to equation (7) to determine the effective diffusivity for different temperatures.

$$k_o = \left(\frac{\pi^2 D_{eff}}{4 L^2}\right) \quad (8)$$

Activation energy (E_a)

The effective diffusivity can be related with temperature by Arrhenius equation [23] as presented in the following equation:

$$D_{eff} = D_0 \exp\left[\frac{E_a}{R(T + 273.15)}\right] \quad (9)$$

where:

D_0 [$\text{m}^2 \cdot \text{s}^{-1}$] - constant in Arrhenius equation,

E_a [$\text{kJ} \cdot \text{mol}^{-1}$] - activation energy,

T [$^{\circ}\text{C}$] - temperature,

R [$\text{kJ} \cdot \text{mol}^{-1} \cdot \text{K}^{-1}$] - universal gas constant

Equation (9) can be rearranged in the form of :

$$\ln(D_{eff}) = \ln(D_0) - \frac{E_a}{R(T + 273.15)} \quad (10)$$

The activation energy can be calculated by plotting a curve between $\ln(D_{eff})$ versus $1 \cdot (T+273.15)^{-1}$.

MATERIAL AND METHODS

The experiments were conducted at CIPHET, Ludhiana. Henna leaves were dried in tunnel dryer to study the drying behavior of henna leave.

Sample Preparation

The henna leaves from CIPHET, Ludhiana farm were harvested in the morning for each experiment. Harvested leaves were cleaned and sorted for unwanted stems and waste materials before putting them in to drying operation. The known weights of samples (300 g) were weighed and spread uniformly in thin layers within the drying trays.

Drying Equipment and Procedure

Henna leaves were dried in a tunnel dryer at six drying temperatures viz.; 40, 45, 50, 55, 60 and 65°C. Tunnel dryer, laboratory model, was a cross flow type dryer (NSW-600, Narang Scientific Works, New Delhi). Tunnel dryer's overall dimensions were 3.06 x 1.10 x 2.15 m. A tunnel, an electrical heater, a fan and a temperature controller (30 to 110°C) were the main components of the dryer. The speed of the tunnel was fixed at 0.004 m·s⁻¹ for the experiments. Samples were replicated thrice in each case of drying. The weight loss data were observed at an interval of 30 minutes during drying.

Physical Properties

Henna leaves thickness, length and breadth were measured using micrometer with a least count of 0.01 mm. Surface temperatures of henna leaves were measured by high performance Infrared thermometer (MaxiTemp, SIKA, Germany, Model: IR M x 4PTDG).

Henna Powder Preparation

Dried henna leaf samples were ground to fine particles by using a home mixer and the powder was sieved before making paste. Henna powder was analyzed for particle size distribution with the help of sieve analysis (Sieve No: 100, 65, 35 and pan).

Statistical Analysis

The experimental data was analyzed as per the procedure of one way/ two way classified ANOVA using computer software package AgRes and mathematical modeling of convective thin layer drying of henna leaves was done by using STATISTICA 6.0.

RESULTS AND DISCUSSION

Physical Dimensions of Fresh Henna Leaves

The physical dimensions of henna leaves are presented in Table 2. The average thickness, length and central breadth of leaves were about 0.26 mm, 18.42 mm, and 7.82 mm, respectively. The surface area of the leaves was ranged from 63.90 to 205.00 mm² with an average of 149.42 mm².

Table 2. Physical dimension of henna leaves (mm)

Sample	Thickness (mm)	Length (mm)	Breadth (mm)	Surface area (mm ²)
1	0.27	19.63	7.46	146.40
2	0.26	17.42	7.95	138.49
3	0.26	22.60	7.36	166.33
4	0.27	16.80	12.13	203.70
5	0.27	21.75	7.31	188.99
6	0.26	14.20	5.14	73.02
7	0.25	19.20	8.28	158.97
8	0.26	14.20	4.50	63.90
9	0.25	20.00	10.25	205.00
Mean	0.26	18.42	7.82	149.42

Drying Behavior of Henna Leaves

Moisture content of fresh henna leaves was 66.954% (w.b). Table 3. presents the drying time at different drying temperature regime in tunnel dryer. Minimum time (270 min) was recorded at 65°C, whereas maximum time (540 min) was observed for henna leaves drying in tunnel dryer at 40°C.

Table 3. Drying time for henna leaves in tunnel dryer

S. No.	Drying air temperature (°C)	Henna leaves drying time (min)
1	65	270
2	60	300
3	55	360
4	50	420
5	45	510
6	40	540

Drying of the leaves mainly occurred in falling rate period. Figure 1. shows the plot between moisture losses with respect to time for the samples dried in tunnel dryer at

different drying temperatures. The more was the temperature, the faster was the drying. The moisture depletion per hour was more in the initial drying period and subsequently it started to decrease. The similar pattern was observed for all samples dried at different temperatures in tunnel dryer. In some cases drying rate was initially low and then started to increase, this period is known as heating period. Heating period observed because sometimes a portion of energy is utilized to heat the material instead of completely contributing for moisture loss. A constant rate period was not observed because of higher time interval between (30 min) between two successive observations. A single falling rate period was observed for all samples for drying of henna leaves in tunnel dryer. Similar findings were observed by [10] for basil leaves and by [11] for mint leaves. Figure 1 shows moisture ratio variation with respect to time for henna drying in the tunnel dryer at different temperatures.

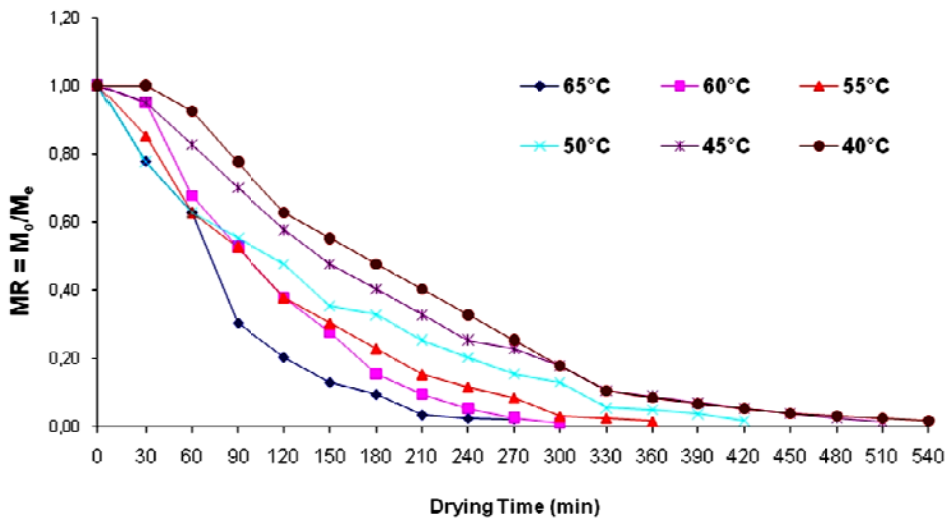


Figure 1. MR of tunnel dried henna leaves

Mathematical Models for Fitting Drying Curves

Moisture ratio and drying time data were fitted for 12 thin layer drying models (Table 1) and the models were evaluated on the basis of r^2 , χ^2 , MBE and $RMSE$ values. Table 4. depicts on the mentioned parameters to ascertain the best fit of the observed data.

In all cases, the r^2 values were greater than 0.90 except for Page model at all temperatures, indicating a good fit of the data. The results (Table 4) show that highest values of r^2 and lowest values of χ^2 , MBE and $RMSE$ were obtained for Midilli-Kucuk model with highest r^2 value of 0.9987 followed Modified Page 1 (0.9985) and Diffusion approach (0.9984). Thus, Midilli-Kucuk model marginally better represented the thin layer drying behavior of henna leaves when dried in tunnel dryer. Similar findings were reported for hot air drying of apricots [15, 19], rosehip [8] and plum [20]. An examination of the r^2 , χ^2 , MBE and $RMSE$ showed that the all models vary with temperatures (Table 4). The constants of the models are presented in Table 5(a-c).

Table 4. Mathematical models statistical analyses results of thin layer tunnel drying of Henna leaves

S.no.	Model name	Model equation	Drying temp.(°C)	R ²	Chi sq	MBE	RMSE
1	Newton						
		MR = Exp(-k t)	65	0.97042	0.00369	-0.00396	0.01824
			60	0.95016	0.00664	-0.00039	0.02343
			55	0.98806	0.00127	-0.00340	0.00950
			50	0.99000	0.00089	-0.00605	0.00742
			45	0.97141	0.00315	-0.00078	0.01285
			40	0.94089	0.00737	0.00146	0.01918
2	Page						
		MR = Exp(-k t ⁿ)	65	0.45550	0.07650	0.00000	0.07823
			60	0.32056	0.10065	0.00000	0.08652
			55	0.37623	0.07245	0.00000	0.06867
			50	0.38350	0.05879	0.00000	0.05828
			45	0.23870	0.08901	0.00000	0.06630
			40	0.18953	0.10705	0.00000	0.07100
3	Modified Page 1						
		MR = Exp(-(k t) ⁿ)	65	0.99157	0.00118	0.00248	0.00973
			60	0.99558	0.00066	0.00124	0.00698
			55	0.99736	0.00031	-0.00204	0.00447
			50	0.99010	0.00094	-0.00608	0.00739
			45	0.99855	0.00017	0.00040	0.00289
			40	0.99580	0.00055	0.00256	0.00511
4	Henderson and Pabis						
		MR = a Exp(- k t)	65	0.97440	0.00360	-0.01045	0.01696
			60	0.96452	0.00526	-0.01457	0.01977
			55	0.99081	0.00107	-0.00783	0.00834
			50	0.99017	0.00094	-0.00514	0.00736
			45	0.98280	0.00201	-0.01015	0.00997
			40	0.96479	0.00465	-0.01436	0.01480
5	Logarithmic						
		MR = a Exp(- k t) + c	65	0.98137	0.00299	0.00000	0.01447
			60	0.98520	0.00247	0.00000	0.01277
			55	0.99711	0.00037	0.00000	0.00467
			50	0.99462	0.00056	0.00000	0.00544
			45	0.99369	0.00079	0.00000	0.00604
			40	0.98359	0.00230	0.00000	0.01010
6	Two-term						
		MR = a Exp(-k t) +b Exp(-n t)	65	0.98737	0.00237	-0.00421	0.01191
			60	0.99308	0.00132	-0.00762	0.00873
			55	0.99563	0.00062	-0.00486	0.00575
			50	0.99039	0.00108	-0.00561	0.00728

			45	0.99388	0.00082	-0.00667	0.00594
			40	0.98529	0.00220	-0.01007	0.00956
7	Two-term exponential						
	$MR = a \text{Exp}(-k t) + (1 - a) \text{Exp}(-k a t)$		65	0.97017	0.00419	-0.00472	0.01831
			60	0.94983	0.00743	-0.00089	0.02351
			55	0.98784	0.00141	-0.00382	0.00959
			50	0.99039	0.00092	-0.00561	0.00728
			45	0.97107	0.00338	-0.00166	0.01292
			40	0.94048	0.00786	0.00038	0.01924
8	Wang and Singh						
	$MR = 1 + a t + b t^2$		65	0.98693	0.00184	0.00187	0.01212
			60	0.98570	0.00212	0.00966	0.01255
			55	0.99518	0.00056	0.00961	0.00604
			50	0.97962	0.00194	-0.01054	0.01060
			45	0.99476	0.00061	0.00509	0.00550
			40	0.98129	0.00247	0.01265	0.01079
9	Diffusion approach						
	$MR = a \text{Exp}(-k t) + (1 - a) \text{Exp}(-k b t)$		65	0.99176	0.00132	0.00051	0.00962
			60	0.99602	0.00066	-0.00215	0.00662
			55	0.99723	0.00035	-0.00176	0.00458
			50	0.99039	0.00099	-0.00562	0.00728
			45	0.99845	0.00019	-0.00078	0.00299
			40	0.99586	0.00058	-0.00244	0.00507
10	Modified Henderson and Pabis						
	$MR = a \text{Exp}(-k t) + b \text{Exp}(-n t) + c \text{Exp}(-m t)$		65	0.97440	0.00719	-0.01045	0.01696
			60	0.96452	0.00946	-0.01457	0.01977
			55	0.99081	0.00168	-0.00783	0.00834
			50	0.99017	0.00135	-0.00514	0.00736
			45	0.98280	0.00268	-0.01015	0.00997
			40	0.96479	0.00608	-0.01436	0.01480
11	Verma <i>et al.</i>						
	$MR = a \text{Exp}(-k t) + (1 - a) \text{Exp}(-m t)$		65	0.98737	0.00203	-0.00421	0.01191
			60	0.99308	0.00115	-0.00762	0.00873
			55	0.99563	0.00056	-0.00486	0.00575
			50	0.99039	0.00099	-0.00561	0.00728
			45	0.99388	0.00076	-0.00667	0.00594
			40	0.98529	0.00206	-0.01007	0.00956
12	Midilli-Kucuk						
	$MR = a \text{Exp}(-k t^n) + b t$		65	0.06939	0.17434	0.13295	0.10228
			60	0.99598	0.00077	0.00001	0.00665
			55	0.99805	0.00028	0.00001	0.00384
			50	0.99690	0.00035	-0.00004	0.00414
			45	0.99874	0.00017	0.00003	0.00270
			40	0.99623	0.00056	-0.00011	0.00484

Table 5a. Mathematical models statistical analyses constants and standard errors of thin layer tunnel drying of Henna leaves

S. no.	Model name	Model equation	Drying temp. (°C)	Constant			Std Error		
				K	N	A	K	N	A
1	Newton								
	MR = Exp(-k t)		65	0.011828			0.000873		
			60	0.008577			0.000745		
			55	0.008234			0.000300		
			50	0.006917			0.000194		
			45	0.005400			0.000254		
			40	0.004861			0.000335		
2	Page								
	MR = Exp(-k t ⁿ)		65	1.403437	0.000000		0.375025	0.000000	
			60	1.157232	0.000000		0.319137	0.000000	
			55	1.278839	0.000000		0.279142	0.000000	
			50	1.250749	0.000000		0.226350	0.000000	
			45	1.163550	0.000000		0.231642	0.000000	
			40	1.109421	0.000000		0.233868	0.000000	
3	Modified Page 1								
	MR = Exp(-(k t) ⁿ)		65	0.011312	1.397826		0.000398	0.102615	
			60	0.008219	1.563206		0.000173	0.076078	
			55	0.007991	1.206282		0.000131	0.036930	
			50	0.006893	1.018002		0.000204	0.050701	
			45	0.005201	1.378942		0.000047	0.026223	
			40	0.004658	1.625569		0.000067	0.055497	
4	Henderson and Pabis								
	MR = a Exp(-k t)		65	0.012430		1.057635	0.001064		0.052995
			60	0.009437		1.110480	0.000856		0.060281
			55	0.008601		1.046831	0.000355		0.026411
			50	0.006842		0.989086	0.000259		0.023182
			45	0.005917		1.101172	0.000275		0.032313
			40	0.005552		1.154763	0.000364		0.048090

Table 5b Mathematical models statistical analyses constants and standard errors of thin layer tunnel drying of Hienna leaves

S. no.	Model name	Drying equation temp.(°C)	Constant					Std Error				
			K	N	A	B	C	K	N	A	B	C
5	Logarithmic $MR = a \text{Exp}(-k t) + c$	65	0.010191		1.124493		-0.085655	0.001656		0.066261		0.064661
		60	0.006074		1.312793		-0.243194	0.001136		0.100574		0.112957
		55	0.006916		1.114694		-0.092894	0.000401		0.022674		0.023978
		50	0.005558		1.048864		-0.084069	0.000424		0.028110		0.030927
		45	0.004401		1.203500		-0.139822	0.000337		0.032357		0.036503
6	Two-term $MR = a \text{Exp}(k t) + b \text{Exp}(-n t)$	65	1.000000	0.014647	-0.267967	1.267967		0.000000	0.001394	0.117566	0.107363	
		60	1.000000	0.011412	-0.362067	1.362067		0.000000	0.000632	0.072821	0.063121	
		55	1.000000	0.009290	-0.133976	1.133976		0.000000	0.000368	0.043935	0.036197	
		50	1.000000	0.006746	0.024702	0.975298		0.000000	0.000345	0.050132	0.037815	
		45	1.000000	0.006470	-0.207868	1.207868		0.000000	0.000219	0.042497	0.031440	
7	Two-term exponential $MR = a \text{Exp}(k t) + (1 - a) \text{Exp}(-k a t)$	65	6.894096		0.001707				421.472894	0.116786		
		60	6.808698		0.001256				591.273531	0.120329		
		55	4.365043		0.001880				106.353312	0.049891		
		50	0.273781		0.024642				0.398160	0.034862		
		45	3.711693		0.001448				130.470032	0.057152		
8	Wang and Singh $MR = 1 + a t + b t^2$	65			-0.008591	0.000019				0.000341	0.000000	
		60			-0.006228	0.000010				0.000315	0.000000	
		55			-0.006012	0.000009				0.000124	0.000000	
		50			-0.005074	0.000007				0.000185	0.000000	
		45			-0.003986	0.000004				0.000078	0.000000	
		40			-0.003556	0.000003			-0.003556	0.000000		

Table 3c. Mathematical models statistical analyses constants and standard errors of thin layer tunnel drying of *Hemra leavus*

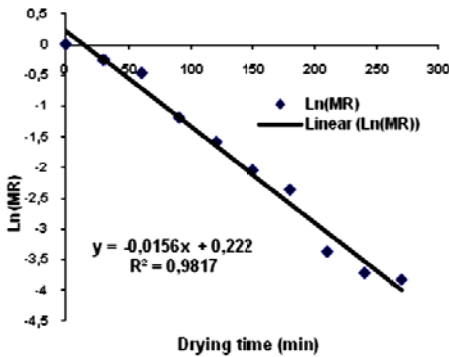
S. no.	Model name	Model equation	Drying temp.(°C)	Constant						Std Error						
				K	N	A	B	C	M	K	N	A	B	C	M	
9. Diffusion approach																
	$MR = a \cdot \text{Exp}(-k \cdot t) - (1 - a) \cdot \text{Exp}(-k \cdot b \cdot t)$		65	0.025151	-5.576747	0.858802				0.069194			182.4629	4.223544		
			60	0.020756	-5.452366	0.831049				0.024624			65.05097	1.756778		
			55	0.014703	-4.702405	0.856850				0.030915			148.5565	3.312333		
			50	0.224515	0.024682	0.030046				52.202869			7.090273			
			45	0.011694	-4.376389	0.833857				0.007193			27.10980	0.898172		
			40	0.011675	-7.814641	0.871906				0.011833			108.38962	1.624833		
10. Modified Henderson and Pabis																
	$MR = a \cdot \text{Exp}(k \cdot t) + b \cdot \text{Exp}(-a \cdot t) + c \cdot \text{Exp}(-m \cdot t)$		65	0.012433	0.012425	0.455135	0.410554	0.193936	0.012430	4.23655053	36679.2359	3818307.3657	5400632.3181	4659588.4969	176566.9151	
			60	0.009438	0.009436	0.336407	0.565152	0.208919	0.009438	1.59146.5521	40810.3507	0.000000	1626478.8966	11107992.7237	143866.6381	
			55	0.008600	0.008601	0.387794	0.489312	0.169731	0.008604	3.9537.9895	17346.0108	2442849.9688	3163593.9120	1420548.6888	40512.3606	
			50	0.006841	0.006843	0.369564	0.457351	0.162170	0.006839	11791.8409	12465.0893	0.000000	0.0000	0.0000	8297.3145	
			45	0.005917	0.005917	0.389005	0.518821	0.193347	0.005917	55465.6116	49848.6969	2250803.3630	2261165.6365	1349684.3862	22167.6813	
			40	0.005553	0.005552	0.335496	0.583768	0.235508	0.005553	59394.9853	5850.3560	6978719.7541	111189654.6409	4603090.4172	99206.3588	
11. Verma et al.																
	$MR = a \cdot \text{Exp}(-k \cdot t) + (1 - a) \cdot \text{Exp}(-m \cdot t)$		65	0.014647	1.267975				1.000000	0.001291			0.099389			0.0000
			60	0.011412	1.362059				1.000000	0.000591			0.059048			0.0000
			55	0.009290	1.133973				1.000000	0.000349			0.034341			0.0000
			50	0.006746	0.975299				1.000000	0.000330			0.036204			0.0000
			45	0.006470	1.207866				1.000000	0.000212			0.030374			0.0000
			40	0.006221	1.302332				1.000000	0.000302			0.048511			0.0000
12. Midilli-Kucuk																
	$MR = a \cdot \text{Exp}(-k \cdot t)^n + b \cdot t$		65	1.000000	1.000000	1.000000	0.00653			0.000000			0.000000	0.000824		
			60	0.000778	1.492092	1.019436	-0.00041			0.000462			0.125075	0.025728	0.000095	
			55	0.004004	1.134934	1.005132	-0.00089			0.001137			0.039528	0.016066	0.000054	
			50	0.014100	0.819776	0.996263	-0.00323			0.004197			0.063870	0.018442	0.000088	
			45	0.000930	1.327473	1.014047	-0.00022			0.000022			0.045477	0.011357	0.000023	
			40	0.000232	1.564158	1.023611	-0.00002			0.000110			0.088503	0.018884	0.000032	

Moisture Diffusivity

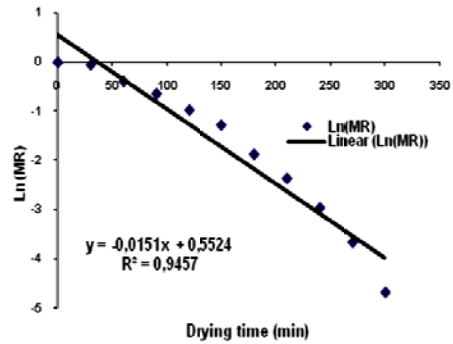
Values of D_{eff} with coefficient of correlation and r^2 are given in Table 6. Effective moisture diffusivity of henna leaves ranged from $2.24 \cdot 10^{-10}$ to $4.31 \cdot 10^{-10} \text{ m}^2 \cdot \text{s}^{-1}$. These values are within the general range $10^{-9} - 10^{-11} \text{ m}^2 \cdot \text{s}^{-1}$ for drying of food materials [24]. The moisture diffusivity increased as drying air temperature was increased. Plots of moisture diffusivity during drying are shown in Figures 2 (a-f) for different temperature regimes.

Table 6. Moisture diffusivity and its linear equation for henna leaves at different temperatures

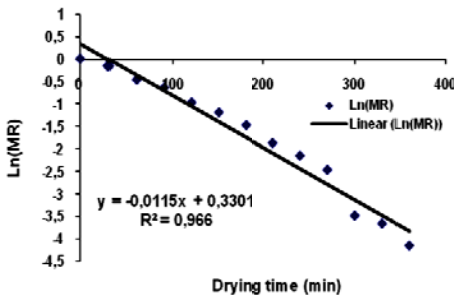
Drying temperature (°C)	Equation	K_o	D_{eff}	R^2
65	$y = -0.0156x + 0.2220$	-0.0156	4.31E-10	0.9817
60	$y = -0.0151x + 0.5524$	-0.0151	4.17E-10	0.9457
55	$y = -0.0115x + 0.3301$	-0.0115	3.18E-10	0.9660
50	$y = -0.0089x + 0.2449$	-0.0089	2.46E-10	0.9537
45	$y = -0.0081x + 0.4028$	-0.0081	2.24E-10	0.9697
40	$y = -0.0081x + 0.4799$	-0.0081	2.24E-10	0.9764



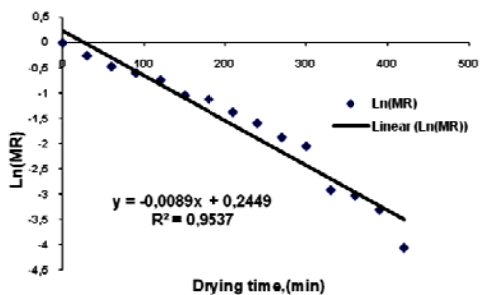
a.



b.



c.



d.

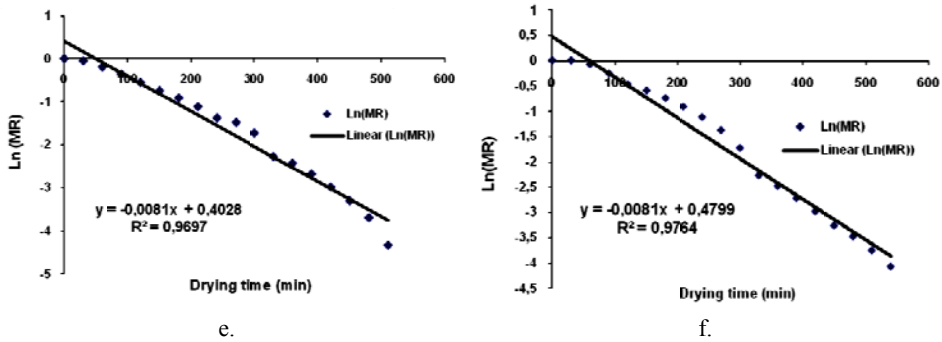


Figure 2. Effect of different drying air temperature on moisture diffusivity during tunnel drying ($\ln(MR)$ Vs. Drying time) of henna leaves
a. 65°C, b. 60°C, c. 55°C, d. 50°C, e. 45°C, f. 40°C

Activation Energy

Activation energy is the minimum energy required to initiate the moisture migration from the product. Moisture diffusivity (on log scale) values were plotted against temperature and the slope of the plot was used to calculate the activation energy as discussed in material and methods section. The activation energy of henna leaves was $27.04 \text{ kJ}\cdot\text{mol}^{-1}$, which is within the range of $12.87 - 58.15 \text{ kJ}\cdot\text{mol}^{-1}$ reported by [25] for other highly perishable commodities. The dried henna leaves were ground using home mixer to an average particle size of 0.2069 mm with a fineness modulus of 1.3685 [26].

CONCLUSIONS

The drying studies on henna leaves was carried at different temperatures from 40 to 65°C at an interval of 5°C in a tunnel dryer with belt speed of 30 rpm . Tunnel dryer took about 270 to 540 minutes to dry a 300 g of henna leaves samples. The thickness of henna leaf was about 0.2611 mm and having moisture content of $66.95\% \text{ w.b.}$ The drying of henna leaves occurred mainly in falling rate period. The drying time required was minimum in case of 65°C temperature samples and it increased with the decrease in drying air temperature. Midilli-Kucuk model described the drying behavior of henna leaves with highest r^2 value of 0.9987 . Effective moisture diffusivity of henna leaves ranged from $2.24\cdot 10^{-10}$ to $4.31\cdot 10^{-10} \text{ m}^2\cdot\text{s}^{-1}$ and it increased with the increase in drying air temperature. The activation energy for the henna leaves was found to be $27.03 \text{ kJ}\cdot\text{mol}^{-1}$. The fineness modulus of powder was 1.3685 and average particle size was 0.2069 mm .

BIBLIOGRAPHY

- [1] Hosein, H., Zinab, D. 2007. Phenolic Compounds and Antioxidant Activity of Henna Leaves extracts (*Lawsonia Inermis*). *World Journal of Dairy and Food Sciences*, 2(1), 38-41.

- [2] Kikuzaki, H., Nakatani, N. 1993. Antioxidant effects of some ginger constituents. *Journal of Food Science*, 58(14), 1407-1410.
- [3] Muhammad, H., Muhammad, S. 2005. The use of *Lawsonia inermis* linn. (henna) in the management of burn wound infections. *African Journal of Biotechnology*, 4 (9), 934-937.
- [4] Verma, N., Mehra, D., Niyogi, U., Khandal, R. 2008. Retention of color intensity in henna paste during storage. *Radiance*, 7(2), 118-121.
- [5] Dev, V., Venugopal, J., Sudha, S., Deepika, G., Ramkrishna, S. 2009. Dyeing and antimicrobial characteristics of chitosan treated wool fabrics with henna dye. *Carbohydrate Polymers*, 75 (4), 646-650.
- [6] Chaudhary, G., Goyal, S., Poonia, P. 2010. *Lawsonia inermis* Linnaeus: A Phytopharmacological Review. *International Journal of Pharmaceutical Sciences and Drug Research*, 2(2), 91-98
- [7] Midilli, A. 2001. Determination of pistachio drying behaviour and conditions in solar drying systems. *International Journal of Energy Research*, 25, 715-725.
- [8] Erenturk, S., Gulaboglu, M., Gultekin, S. 2004. The thin layer drying characteristics of rosehip. *Biosystems Engineering*, 89 (2), 159 – 166.
- [9] Kadam, D., Samuel, D. 2006. Convective flat-plate solar heat collector for cauliflower drying. *Biosystems Engineering*, 93 (2), 189-198.
- [10] Kadam, D., Goyal, R., Gupta, M. 2011. Mathematical modeling of convective thin layer drying of basil leaves. *Journal of Medicinal Plants Research*, 5(19), 4721-4730.
- [11] Kadam, D., Goyal, R., Singh, K., Gupta, M. 2011. Thin layer convective drying of mint leaves. *Journal of Medicinal Plants Research*, 5(2), 164-170.
- [12] Pangavhane, D., Sawhney, R., Sarsavadia, P. 1999. Effect of various dipping pre-treatment on drying kinetics of Thompson seedless grapes. *Journal of Food Engineering*, 39, 211-216.
- [13] Kadam, D., Dhingra, D. 2011. Mass transfer kinetics of banana slices during osmo-convective drying. *Journal of Food Process Engineering*, 34 (2), 511-532.
- [14] Kadam, D., Nangare, D., Singh, R., Kumar, S. 2011. Low-cost greenhouse technology for drying onion (*Allium cepa* L.) Slices. *Journal of Food Process Engineering*, 34 (1), 67-82.
- [15] Doymaz, I. 2004. Effect of pre-treatments using potassium metabisulphite and alkaline ethyl oleate on the drying kinetics of apricots. *Biosystems Engineering*, 89(3), 281 – 287.
- [16] Ozdemir, M., Devres, Y. 1999. The thin layer drying characteristic of hazelnuts during roasting. *Journal of Food Engineering*, 42, 225-233.
- [17] Yaldiz, O., Ertekin, C., Uzun, H. 2001. Mathematical modeling of thin layer solar drying of sultana grapes. *Energy – An International Journal*, 26, 457 – 465.
- [18] Sarsavadia, P., Sawhney, R., Pangavhane, D., Singh, S. 1999. Drying behavior of brined onion slices. *Journal of Food Engineering*, 40, 219 – 226.
- [19] Togrul, I., Pehlivan, D. 2002. Mathematical modeling of solar drying of apricots in thin layers. *Journal of Food Engineering*, 55, 209 – 216.
- [20] Goyal, R., Kingsly, A., Manikanthan, M., Ilyas, S. 2007. Mathematical modeling of thin layer drying kinetics of plum in a tunnel dryer. *Journal of Food Engineering*, 79, 176 – 180.
- [21] Doymaz, I., Togrul, N., Pala, M. 2006. Drying characteristics of dill and parsley leaves. *Journal of Food Engineering*, 77, 559-565.
- [22] Crank, J. 1975. *Mathematics of diffusion*. Clarendon Press, Oxford, UK.
- [23] Simal, S., Mulet, A., Tarrazo, J., Rosello, C. 1996. Drying models for green peas. *Food Chemistry*, 55, 121-128.

- [24] Maskan, A., Kaya, S., Maskan, M. 2002. Hot air and sun drying of grape leather (pestil). *Journal of Food Engineering*, 54, 81-88.
- [25] Senadeera, W., Bhandari, B., Young, G., Wijesinghe, B. 2003. Influence of shapes of selected vegetable materials on drying kinetics during fluidized bed drying. *Journal of Food Engineering*, 58, 277-283.
- [26] Sahay, K., Singh, K. 1994. *Unit Operations of Agricultural Processing*. 1st Ed. Vikas Publishing House Pvt. Ltd, New Delhi, India.

KINETIKA SUŠENJA TANKOG SLOJA LISTOVA KANE

Dattatreya M. Kadam¹, Manoj Kumar Gupta², Vaijayanta M Kadam³

¹Centralni institut za post-žetveni inženjering i tehnologiju,

PO: PAU campus, Ludhiana-141004 (Pendžab), Indija

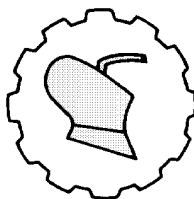
²Infosys Limited, Electronic City, Phase I, Bangalor, Karnataka, Indija

³Državni institut za hortikulturu, Karnataka, Indija

Sažetak: Listovi kane su dobro poznati po svojim kozmetičkim agensima sa anti-kancerogenim, anti-inflamatornim, analgetskim i anti-piretičkim svojstvima. Laboratorijski modeli tunelske sušare su korišćeni za sušenje listova na 40, 45, 50, 55, 60 i 65°C i ispitivanje uticaja različitih uslova kinetiku sušenja listova kane. Period sušenja listova kane se skraćivao i sušenje je bilo brže pri višoj temperature. Dvanaest modela sušenja tankog sloja je poređeno sa eksperimentalnim podacima o odnosima vlage. Među matematičkim modelima koji su ispitivani, model Midilli-Kucuk je na zadovoljavajući način opisao ponašanje pri sušenju sa najvišim vrednostima r^2 . Efektivna difuzija vlage (D_{eff}) listova povećala se sa povećanjem temperature vazduha za sušenje. Efektivna difuzija vlage listova kane iznosila je od $2.24 \cdot 10^{-10}$ do $4.31 \cdot 10^{-10} \text{ m}^2 \cdot \text{s}^{-1}$, a energija aktivacije $27.03 \text{ kJ} \cdot \text{mol}^{-1}$. Osušeni listovi su mleveni u prah sa prosečnim dimenzijama čestica od 0.2069 mm i modulom finoće 1.3685.

Ključne reči: kana, matematičko modeliranje, sušenje, difuzija vlage, energija aktivacije

Prijavljen: 23.06.2013.
Submitted:
Ispravljen: 07.07.2013.
Revised:
Prihvaćen: 30.07.2013.
Accepted:



UDK: 631.536

Originalni naučni rad
Original scientific paper

AERODYNAMIC AND SOLIDS CIRCULATION RATES IN SPOUTED BED DRYING OF CARDAMOM (Part 2)

**Murugesan Balakrishnan¹, Velath Variyathodiyil Sreenarayanan¹,
Ashutosh Singh², Gopu Raveendran Nair², Rangaraju Viswanathan¹,
Grama Seetharama Iyengar², Vijaya Raghavan^{2*}**

¹*Tamil Nadu Agricultural University,
Department of Food and Agricultural Process Engineering,, Coimbatore, India*
²*McGill University, Department of Bioresource Engineering,
Macdonald Campus, Ste-Anne-de-Bellevue, Quebec, Canada*

Abstract: Two dimensional spouted bed units with flexible bed dimensions were used with draft tubes to study spouting pressure drop and minimum spouting velocity, solids circulation rate and average cycle time. The data were collected while varying slant angle, draft tube height, separation distance and height of bed using cardamom. The variables which affect the spouting pressure drop and airflow through the beds are discussed. Empirical correlations were developed following the principles of dimensional analysis and similitude. The developed correlations were in accordance with the collected data. The article has been divided into two parts where the first part includes the analysis for spouting pressure drop and minimum spouting velocity and the second parts includes the solids circulation rate and average cycle time.

Key words: *Spouting pressure drop, minimum spouting velocity, solids circulation rate, average cycle time, dimensional analysis, Elettaria cardamomum, Conical-Cylindrical Spouted Bed (CSB), curing chambers, rectangular orifices*

* Corresponding author. E-mail: vijaya.raghavan@mcgill.ca

The authors are grateful for the financial support provided by Canadian International Development Agency (CIDA) and Natural Sciences and Engineering Research Council (NSERC) of Canada.

INTRODUCTION

Spouted bed technology is very useful for drying solids that are sticky, have irregular texture and vary widely in particle size distribution. Application of vigorous movements of solids in spouted bed helps in uniform drying but the performance depends widely on the cyclic movement of the solid particles and also on the properties related to solid circulation such as cycle time and fraction of this time spent in the spout and annular zones [1]. The solid circulation rate in a two dimensional spouted bed dryer is estimated using the particle velocity above the cone and the particle voidage in the spout or in the downcomer [2]. In the spout, the particle velocity is measured by tracking the particle but in the downcomer the particle velocity is influenced by the inlet air velocity, the inlet nozzle width, spout width and the separation distance between the draft tubes. Several researchers have tried to develop mathematical models for solid circulation rate, but they lack a sound understanding of parametric relationships. Hence for a two dimensional spouted bed dryer it is important to conduct proper experimental studies to explain the relation between factors and how they are influenced by the presence of draft tubes.

In a spouted bed dryer the continuous movement of particles between the spout and the downcomer has a significant effect on its performance. In 1959 Thorley, *et al.* [6] investigated conical-cylindrical spouted beds without draft tubes indicating that the cycle time can be quantified with or without solid circulation rate in conjunction with particle properties, bed geometry and volumetric gas flow. They calculated the mean cycle time by dividing the total mass of particles in the bed by the solids circulation rate. The approach applied by Thorley *et al.* (1959) [6] agrees well with measured values and are compatible for estimation of cycle time [2].

In the present study, parameters such as spouting pressure drop, minimum spouting velocity, solid circulation rate and average cycle time have been considered for the development of mathematical models based on dimensional analysis and similitude principles for a batch type slotted 2DSB with draft tube [3-5]. In part 1 of the study we analysed mathematical models based on spouting pressure drop and minimum spouting velocity. The intent of Part 2 of the study is to investigate the influence of solids circulation rate and average cycle time on the spouting characteristics of spouted bed with draft tube while taking into account grain particle parameters in order to provide a sound basis for the design of commercially viable units.

MATERIAL AND METHODS

Details on the theory and model development are provided in the Part 1 of the study. The assumptions made to generate mathematical models for solids circulation rate and average cycle time are same as mentioned in Part 1 of the study. Tables 1 and 2 represent the pertinent and repeating variables considered for the mathematical modeling.

The chosen variables were convenient for the experimental and analytical phase of the study. The time taken by particles to make the journey from the top of the down comer back to their starting point is of considerable interest in solids mixing, heat treatment and drying applications. Previous studies have shown that the proportion of time spent by a particle in the draft tube is insignificant compared to time spent in the down comer [6-8]. Hence, the average cycle time should be dependent on the total mass of solids in the bed, the solids

circulation rate, width of the down comer, slanting angle and normal distance. Other factors, which may affect the average cycle time, may be airflow and some material properties.

Table 1. The pertinent variables for the mathematical modeling of fluid and particle dynamics in the 2DSB with draft tube

Symbol	Variable	Unit
P_s	Spouting pressure drop	Pa
U_f	Minimum spouting velocity	$\text{m}\cdot\text{s}^{-1}$
ρ_ϕ	Dry air density	$\text{kg}\cdot\text{m}^{-3}$
μ	Absolute viscosity	$\text{kg}\cdot\text{m}^{-1}\cdot\text{s}^{-1}$
g	Acceleration due to gravity	$\text{m}\cdot\text{s}^{-2}$
V_p	Average particle velocity	$\text{m}\cdot\text{s}^{-1}$
Q_p	Volumetric flow rate of grains	$\text{m}^3\cdot\text{s}^{-1}$
S_p	Solids circulation rate	$\text{kg}\cdot\text{s}^{-1}$
M_p	Mass of grains in the spouted bed	kg
t_c	Average cycle time	s
d_p	Geometric diameter of particle	m
ϕ	Sphericity	--
ρ_β	Bulk density of grains	$\text{kg}\cdot\text{m}^{-3}$
ρ_π	Particle density of grains	$\text{kg}\cdot\text{m}^{-3}$
E_v	Bed voidage	---
W_b	Width of spouted bed	m
W_d	Width of a down-comer of spouted bed	m
L_b	Length of spouted bed	m
H_b	Depth of grains in spouted bed	m
H_t	Height of draft tube	m
D_i	Diameter of air entry slot	m
θ_σ	Slant angle	--
D_s	Diameter of draft tube or spout	m
W_o	Normal distance	m

Table 2. Repeating variables for the mathematical models and variables representing mass, length and time

Symbol	Mathematical models				
	P_s	U_f	S_p	t_c	
ρ_ϕ	-	+	+	-	
g	+	+	+	-	
S_p	-	-	-	+	
M_p	-	-	-	+	
d_p	-	+	-	+	
ρ_π	+	-	-	-	
H_t	+	-	-	-	
W_o	-	-	+	+	
	L	H_t	d_p	W_o	d_p
	M	$\rho_\pi H_t^3$	$\rho_\phi \delta_\pi^3$	$\rho_\phi \Omega \sigma^3$	M_p
	T	$(H_t/g)^{1/2}$	$(d_p/g)^{1/2}$	$(W_o/g)^{1/2}$	S_p/M_p

+ = Variable in the theoretical model,

- = Variable not in the theoretical model

The variables that were important for the analysis of air and solids dynamics were selected. A list of variables for the mathematical modeling of 2DSBs with draft tube is given in Tab. 1. It should be noted that not all of these variables are necessarily important for each operational phase of spouted beds.

The normal distance (W_o) of the orifice was calculated from relationship of separation distance (H_E) and slant angle (θ_s): $W_o = H_E \cos \theta_s$

Solids circulation rate: The relevant variables given in Tables 1-2 for the development of the model for the solids circulation rate (average particle velocity) were arranged:

$$F(V_p, U_f, \rho_f, \mu, g, d_p, \rho_p, \phi, E_v, W_o, D_s, \theta_s, L_b, D_b, H_f) = 0 \quad (1)$$

Taking the considered variables in Eq. 1 and using the repeating variables, the following dimensionless numbers were developed:

$$F[V_p/(gW_o)^{0.5}, d_p/W_o, U_f^2/gW_o, \mu^2/g\rho_f^2W_o^3, \rho_p-\rho_f/\rho_f, \phi, E_v, L_b/W_o, \theta_s, W_b/W_o, D_s/D_b, H_f/W_o] = 0 \quad (2)$$

The *PI* numbers given in Eq. 2 were transformed in to the following dimensionless numbers in Eq. 3:

$$V_p/(gW_o)^{0.5} = F[d_p/W_o, Fr, Ar, \rho_p-\rho_f/\rho_f, \phi, E_v, L_b/W_o, \theta_s, D_s/D_b, H_f/W_o] = 0 \quad (3)$$

Where, *Fr* and *Ar* are Froude number and Archimedes number respectively. The theoretical solids circulation rate would then be Eq. 4:

$$S_p = \rho_b A_d V_p \quad (4)$$

Where, A_d is the cross-sectional area of the downcomers.

Or:

$$\begin{aligned} S_p/\rho_b A_d (gW_o)^{0.5} = \\ = F[d_p/W_o, Fr, Ar, \rho_p-\rho_f/\rho_f, \phi, E_v, L_b/W_o, \theta_s, D_s/D_b, H_f/W_o] = 0 \end{aligned} \quad (5)$$

Average cycle time: The relevant variables from Tab. 1, which may constitute the mathematical model of average cycle time, are shown:

$$F(t_c, S_p, M_p, d_p, \phi, W_o, \theta_s, H_b, W_d) = 0 \quad (6)$$

Taking the pertinent variables from Eq. 6 and using the variables in Tables 1-2 the following dimensionless *PI* numbers were generated:

$$F(t_c S_p/M_p, \phi, \theta_s, W_o/d_p, H_b/d_p, W_d/d_p) = 0 \quad (7)$$

The dimensionless numbers in Eq. 7 were transformed in to the following *DPS* to simplify the relationship for average cycle time as shown below:

$$t_c S_p/M_p = F(\phi, \theta_s, W_o/d_p, H_b/W_o, W_d/d_p) = 0 \quad (8)$$

Experimental methods and procedures: The spouted bed drier used for the study is represented in Fig. 1, it consists of motor-blower assembly, heating chamber, hot air delivery duct, temperature controller, plenum chamber and spouted bed chamber. The airflow rate could be adjusted using the built-in motor blower on the suction side. The temperature of the inlet hot air was controlled using temperature controllers. The system was also fitted with ball valves in between the hot air delivery duct and spouted bed to keep cardamom capsules in minimum spouting conditions for as long as needed by adjusting the airflow rate. The design of the two dimensional spouted bed provided the opportunity to vary the bed length-width, the slant angles, separation distance, spout width and air entry slots. A detailed description of the design and measurement procedure is provided in Part 1 of the study.

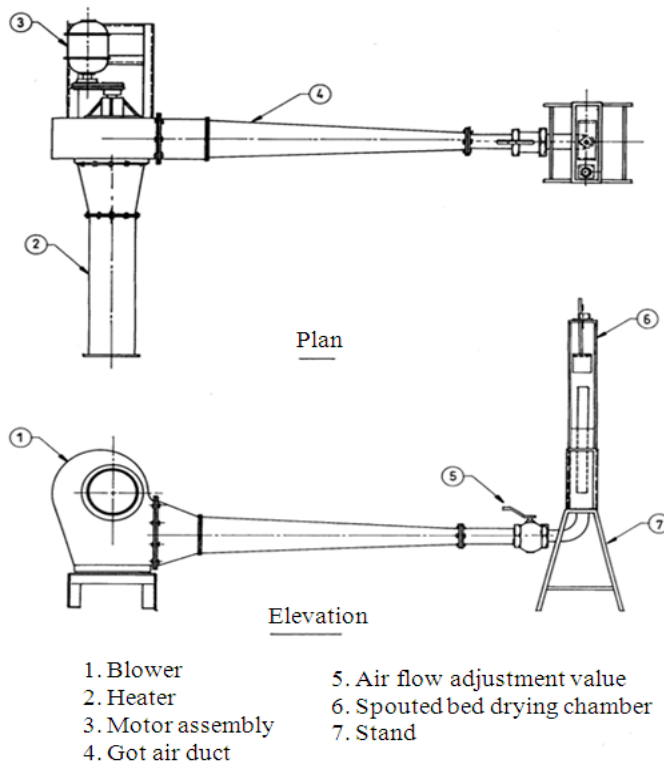


Figure 1. Schematic diagram of spouted bed dryer

RESULTS AND DISCUSSION

PI terms proposed for solids circulation rate and average cycle time were generated from the experimental data and linearized by natural logarithm transformation. M-STAT was used to analyze the data using full regression model and the model was evaluated on the basis of the R^2 statistic, standard error, level of significance (α), residual characteristics and the number of terms in the model.

Solids circulation rate/average particle velocity: The average particle velocities observed over all the runs were in the range of 0.76-1.25 $\text{cm}\cdot\text{sec}^{-1}$. The lowest particle velocity was 0.76 $\text{cm}\cdot\text{sec}^{-1}$ in the case of cardamom dried at air temperature 40°C, 45° slant angle, 5 cm separation distance and draft tube height of 40 cm and the highest was 1.25 $\text{cm}\cdot\text{sec}^{-1}$ in the case of cardamom dried at air temperature 50°C, 60° slant angle, 7.5 cm separation distance and draft tube height of 60 cm with tempering period for 30 min. The solids circulation rates were calculated from the average particle velocity, the effective cross-sectional area of the down comers and the average bulk density. Plots of solids circulation rate versus draft tube heights for various slant angles and separation distances have been shown in Figs. 2-3. It may be observed that the solids circulation rate increased with separation distance. Possible cause for this trend as explained by Buchanan and Wilson (1965) [9], Khoe and Brakel (1983) [1] and Claflin and Fane (1984) [10] for Conical-cylindrical spouted beds and Law *et al.* (1984) [11] and Kalwar *et al.* (1992) [2] for two-dimensional spouted beds.

The solids circulation increased as the draft tube height increased from 40-60 cm and its magnitude increased with separation distance as shown in Figs. 2-3. The solids circulation rate was almost the same when the draft tube height was increased from 50-60 cm, but the difference became greater as the separation distance increased due to the higher number of capsules entering the draft tube.

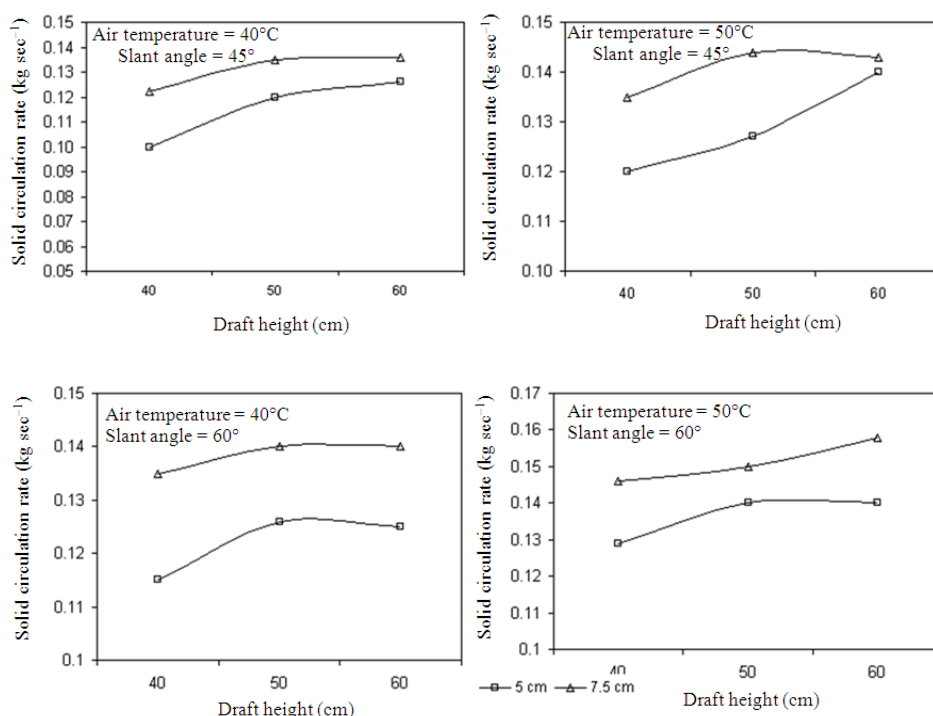


Figure 2. Effect of draft height (H_d) on solid circulation rate for cardamom

The effects of slant angle were detectable when the separation distances were 5 and 7.5 cm as can be judged from Figures 2-3. A steady increase was observed in solids circulation with a rise in slant angle from 45°-60°. This occurred because the solids circulation rate was limited by the dimensions of the orifice formed at the point of normal distance from the slanting base to the bottom of the draft tube. These dimensions decreased as slant angle increased at the same separation distance.

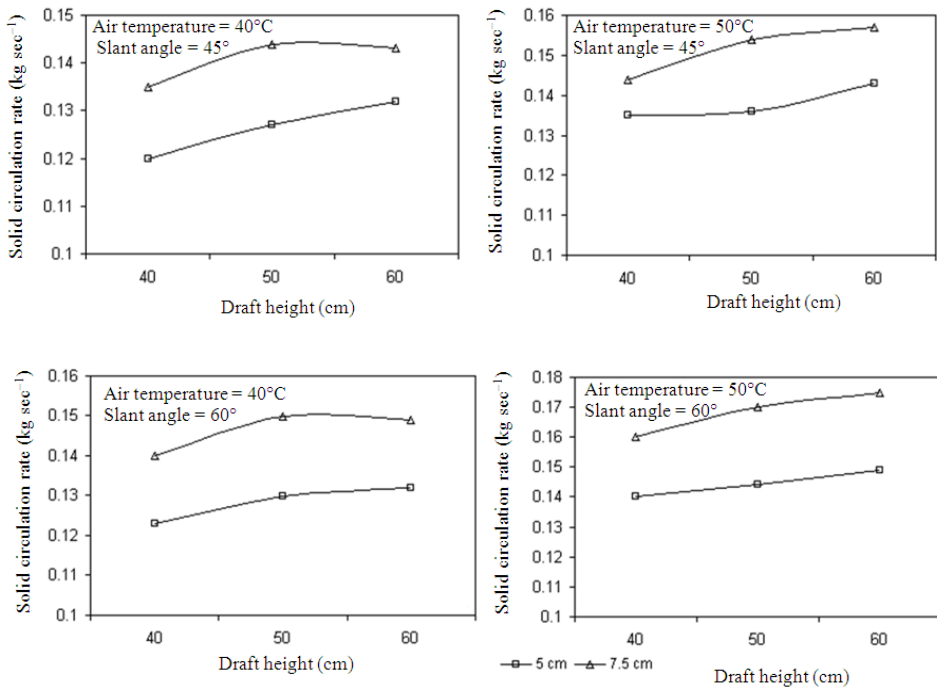


Figure 3. Effect of draft height (H_d) on solid circulation rate with tempering for 30 min for cardamom

Hence, higher than minimum airflow through the bed will not enhance the solid circulation rate. Any further increase in slant angle decreased the solids circulation rate as well as air percolation into the down comer.

From Figs. 2 and 3, it was also observed that the increase in air temperature produced a positive effect on solids circulation rate. This was due to the fact that most of the heating of cardamom capsules occurs in the draft tube and the temperature of air increased the circulation rate of capsules. The mathematical model obtained for solids circulation rate is shown below:

$$= (U_f^2/g H_d)^{-0.2435} (d_p/W_o)^{6.5 E-15} (L_b/W_o)^{0.5513} (D_s H_i/D_i W_o)^{0.0614} (\theta_s)^{0.6268} \quad (9)$$

with $R^2 = 96.51\%$, standard error of estimate = 0.0225 and $\alpha = 0.0001$. A print out of residuals against selected model predictions is shown in Fig. 4b. The plot of observed and predicted values for the solids circulation rate model is plotted in Figure 4a. The developed model predicted the collected data with an average error of $\pm 1.8\%$. The predictions from the solids circulation rate model have been presented in Fig. 4a, which showed a good agreement.

Average cycle time: The cycle times of particles in the case of 45° were 16-20% greater than the slant angle of 60° because of longer particle paths and the mass of grains in the bed. The shortest particle cycle time of 105 sec was observed when the slant angle was 60° , separation distance was 7.5 cm, draft tube height of 40 cm and air temperature of 50°C with tempering period of 30 min. The longest cycle time of 200 sec was found when slant angle was 45° , separation distance was 5 cm, draft tube height of 60 cm and air temperature of 40°C .

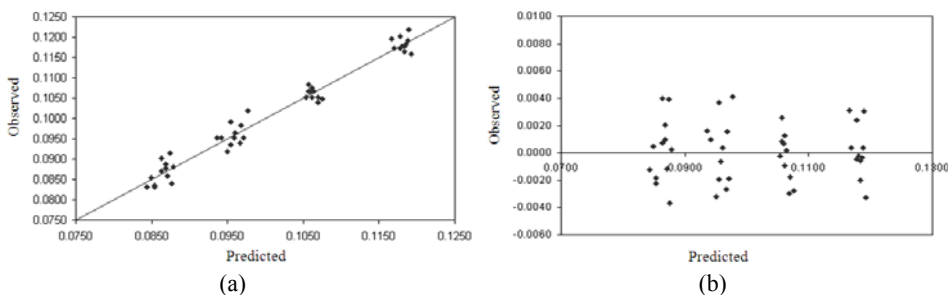


Figure 4. (a) Comparison of solids circulation rate measured with solids circulation rate predicted by Eq. 9 (b) Residual plot for solids circulation rate model, Eq. 9

For any given geometry, the particle cycle time decreases with the distance of particles in the down comer.

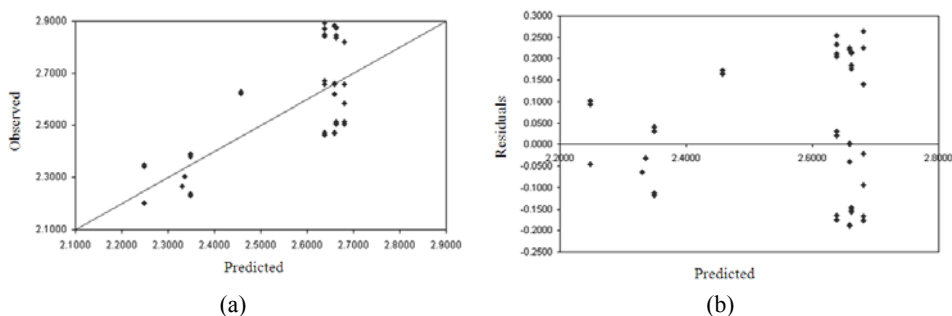


Figure 5. (a) Comparison of observed cycle time data Vs predicted cycle time by Eq. 10 (b) Residual plot average cycle time model, Eq. 10

The cycle time data from the drying runs were regressed against the dimensionless numbers. In principle, the average cycle time should be equal to the mass of particles in the bed divided by the solids circulation rate. But this was not so in the study. The problem could

be due to the effect of separation distance on the cycle time distribution of individual particles. The mathematical model developed for average cycle time is given in Eq. 10.

$$t_c S_p / M_p = (d_p/W_o)^{0.9495} (H_b W_d / W_o d_p)^{-0.9975} (\theta_s)^{1.11} \quad (10)$$

with $R^2 = 81.63\%$, standard error of estimate = 0.0618 and significance level = 0.0001. The model predictions versus observed average cycle times are shown in Fig. 5a. It is concluded that the developed model fits the collected data with an average error of $\pm 12\%$. A print out of residual against selected model predictions is shown in Fig. 5b.

CONCLUSIONS

In part 1 of the study we concluded that spouting pressure drop increases with an increase in separation distance and slant angle. It was also observed that increase in draft tube height led to an increase in spouting pressure drop. We also concluded that minimum spouting velocity increases as the separation distance and draft tube height increase and as the slant angle decreases. In Part 2 of the study it was observed that solid circulation rates (average particle velocity in the down comers) were also affected by separation distance, draft tube height, slant angle and vary with spouting velocity. The average particle times were found to vary with slant angle. Empirical models were developed for solids circulation rate and average cycle time and were found to be in close agreement with experimental data.

BIBLIOGRAPHY

- [1] Khoe, G., Brakel, V.J. 1983. Drying characteristics of a draft tube spouted bed. *The Canadian Journal of Chemical Engineering*, 1983. 61(3): p. 411-418.
- [2] Kalwar, M., Raghavan, G., Mujumdar, A. 1992. Spouting of two-dimensional beds with draft plates. *The Canadian Journal of Chemical Engineering*, 1992. 70(5): p. 887-894.
- [3] Osorio-Revilla, G., Elías-Serrano, R., Gallardo-Velázquez, T. 2004. Drying of Liquid Feedstocks in a Spout-Fluid-Bed with Draft-Tube Submerged in Inert Solids: Hydrodynamics and Drying Performance. *The Canadian Journal of Chemical Engineering*, 2004. 82(1): p. 142-147.
- [4] Osorio-Revilla, G., López-Suárez, T., Gallardo-Velázquez, T. 2004. Simultaneous Drying and Cleaning of Guava Seeds in a Spout-Fluid Bed with Draft Tube. *The Canadian Journal of Chemical Engineering*, 2004. 82(1): p. 148-153.
- [5] Stocker, R.K., Eng, J.H., Svrcek, W.Y., Behie, L.A. 1989. Ultraprolysis of propane in a spouted-bed reactor with a draft tube. *AIChE Journal*, 1989. 35(10): p. 1617-1624.
- [6] Thorley, B., Saunby, J.B., Mathur, K.B., Osberg, G.L. 1959. An analysis of air and solid flow in a spouted wheat bed. *The Canadian Journal of Chemical Engineering*, 1959. 37(5): p. 184-192.
- [7] Becker, H.A. 1961. An investigation of laws governing the spouting of coarse particles. *Chemical Engineering Science*, 1961. 13(4): p. 245-262.
- [8] Gay, E. 1970. Air Flow Requirements and Bed Turnover Time for a Spouted Leed Peanut Dryer. *ASAE*, 22p. 1970.

- [9] Buchanan, R., Wilson, B. 1965. The fluid-lift solids recirculator. *Mech. Chem. Eng. Trans.*, 1965. 1(1): p. 117-124.
- [10] Clafin, J.K., Fane, A.G. 1984. Gas distribution and heat transfer in a draft-tube spouted bed. *In AIChE symposium series, ISSN 0065-8812.* American institute of chemical engineers. 1984, vol. 80, no241, pp. 17-23
- [11] Law, L., et al. 1984. Pressure drop and particle circulation studies in modified slot spouted beds. *Drying'84Hemisphere*, New York, 1984: p. 386-389.

STEPENI AERODINAMIKE I PROTOKA ČVRSTE MATERIJE U ODVODNIM KANALIMA ZA SUŠENJE KARDAMOMA (2. deo)

**Murugesan Balakrishnan¹, Velath Variyathodiyil Sreenarayanan¹,
Ashutosh Singh², Gopu Raveendran Nair², Rangaraju Viswanathan¹,
Grama Seetharama Iyengar², Vijaya Raghavan²**

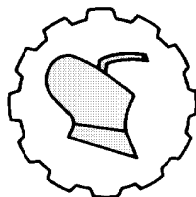
¹*Institut za inženjering prehrambenih i poljoprivrednih procesa,
Poljoprivredni Univerzitet Tamil Nadu, India*

²*Institut za inženjering bioresursa, Univerzitet McGill,
Kampus Macdonald, Ste-Anne-de-Bellevue, Quebec, Kanada*

Sažetak: Za proučavanje pada pritiska u odvodnom kanalu, minimalne brzine odvođenja materijala, stepena cirkulacije čvrstog materijala i prosečnog vremena ciklusa korišćene su dvodimenzionalne jedinice odvodnih kanala sa fleksibilnim dimenzijama. Podaci su prikupljeni variranjem ugla nagiba, visine pripremnog kanala, rastojanja pri separaciji i visine kanala. Analizirane su veličine koje utiču na pad pritiska u odvodnom kanalu i protok kroz kanal. Razvijene su empirijske zavisnosti korišćenjem simulacije i dimenzione analize. Razvijene zavisnosti su bile u skladu sa prikupljenim podacima. Rad je podeljen u dva dela pri čemu se prvi deo bavi analizom pada pritiska u odvodnom kanalu i minimalnom brzinom odvođenja a drugi deo stepenom protoka čvrste materije i prosečnim vremenom ciklusa.

Ključne reči: *Pad pritiska pri odvođenju materijala, minimalna brzina odvođenja, stepen protoka čvrste materije, prosečno vreme ciklusa, dimenziona analiza, Elettaria cardamomum, konično-cilindrični kanal za odvođenje (CSB), komore za konzervaciju, pravougaoni otvori*

Prijavljen: 04.05.2013.
Submitted:
Ispravljen:
Revised:
Prihvaćen: 20.07.2013.
Accepted:



UDK: 027.54

Originalni naučni rad
Original scientific paper

WATER DROPLETS ANALYSIS: THE CLASSICAL AND QUANTUM HYDRODYNAMIC FRAMEWORKS

Daniele De Wrachien¹, Giulio Lorenzini^{2*}, Stefano Mambretti³, Marco Medici²

¹ *University of Milan, Department of Environmental and Agricultural Sciences, Italy*

² *University of Parma, Department of Industrial Engineering, Italy,*

³ *University of Campinas, Faculdade de Tecnologia, Brazil*

Abstract: The design of a sprinkler irrigation system is always associated with a full understanding of the kinematics of the droplets during their aerial path. Resolving this problem involves both theoretical and experimental considerations. Among the theoretical studies the classical mechanical approach, based on the Newton's law, offers a useful tool to describe the trajectories of water droplets from the sprinkler nozzle to the ground. The problem becomes even more complicated when not just a single droplet alone is assessed but a multi-droplet system is accounted for. In addition to the inter-parameter dependencies, it is also observed an inter-droplet reciprocal repulsion, mainly due to electrical interactions between the hydrogen and the oxygen atoms of the different water molecules. An alternative to traditional classical procedures, to analyse water droplet dynamics in sprinkler irrigation, has been recently proposed in the form of a quantum approach. In this context, the whole classic-quantum and single-droplet versus multi-droplet alternatives need to be discussed and pinpointed and these are the main aims of the present paper which focuses on the theoretical part of the issue, thus highlighting the new perspectives of a deeper comprehension in the spray flow related phenomena. On the whole, the new approach leads to the concept of quantum trajectory in analogy to the well-established concept of classical trajectory and allows to recast the classical fluid dynamic equations into the so-called quantum equations.

Key words: *spray particles kinematics, single- and multi-droplet systems, classic and quantum mechanics, sprinkler water droplets, mathematical modelling*

* Corresponding author. E-mail: giulio.lorenzini@unipr.it

INTRODUCTION

Albeit the process of a liquid particle moving within a gaseous phase may describe many different technical applications, broadly investigated in many scientific sectors and from many different points of view, a complete, clear and generally applicable mathematical modelling is still far from having been achieved. Very recently Molle *et al.* [1] gave an extremely useful experimental contribution in the field of irrigation, which will be of substantial usefulness for future investigations and modelling attempts. The results of the present paper were mainly reached by featuring the sprinkler irrigation context. The outcomes, if suitably adapted, may also apply to other fields and aims, such as pesticides distribution, heat removal or fire suppression, to name but a few. The fundamental problem is not just that of solving the equations ruling the development of the system and of the phenomenon but, upstream of that, it lies in the characterization of such equations. According to the Authors of this paper such hurdle can be attributed to a not complete understanding of the system-process evolution. This of course should not be taken as a form of underestimation of the analytical difficulties due to the mutual interrelationships between the parameters that govern the process, on the one hand, and the characteristics of the particles involved, on the other. In fact the main thematic scientific literature [2-6] tries to overcome such computational complication binding the solutions achieved to the specific case studies faced. In general, however, the kinematic analysis of sprinkler water droplets during their aerial path is devised adopting a Newtonian approach and considering a single-droplet system. A ballistic form of the same viewpoint, based on a Newtonian approach for a single-droplet system, was also proposed by the Authors [7-9]. This approach will be described in the paper as a classic/single-droplet model. Coming again to the “not complete understanding of the system-process evolutions” quoted above, the issue has very recently led the Authors of the present work to the belief that to fully comprehend and describe the phenomenon another viewpoint could be considered: the quantum one [10]. The results which were arrived at [11] were in the form of the time-dependent Schroedinger's equation (TDSE) and of the Scale Relativity Theory [12] written as a Riccati equation. The former, in particular, was written for single-droplet systems, seen as waves and material particles [13] and considering a Lagrangian or Eulerian description for both steady and transient states. The present paper, therefore, will treat further possibilities to study the kinematic behaviour of both single- and multi-droplet systems during their aerial path in according to both the classic (i.e. Newtonian) and quantum approach. Moreover, a new procedure, the so-called Density Functional Theory for many-particle systems, has been highlighted, that allows to design a common 3-D space for the assessment of both the droplet trajectories and their interactions, and, so, to recast the TDSE into the quantum fluid-dynamic (continuity and Navier-Stokes) equations [14].

The basic picture that emerges is that of a multi-component fluid mixture moving into a 3-D space under the effects of common electric and magnetic fields and classic and quantum potentials.

THE CLASSIC MECHANICAL PICTURE

We do not wish to review the whole classic approach, as reported in the literature, but to explore the modelling possibilities in relation to the topic of the present paper. Anyway some more information on spray kinematics modelling (mainly Lagrangian) both in sprinkler irrigation and in chemical sprays contexts are also available [3,15-17], while spray drift Lagrangian modelling is treated in [18], and in [19]. Recently the Authors defined the following simplified analytical model feasible to solve water droplets kinematics, based on the Second Principle of Dynamics [7-9]:

$$\begin{cases} \ddot{m} x = -k \dot{x}^2 \\ \ddot{m} y = -k \dot{y}^2 - ng \end{cases} \quad (1)$$

developed in terms of parametric equations:

$$x(t) = \frac{m}{k} \ln \left(\frac{v_{0x} k}{m} t + 1 \right) \quad (2)$$

$$\dot{x}(t) = \frac{m v_{0x}}{m + k v_{0x} t} \quad (3)$$

$$y(t) = h - \frac{m}{k} \ln \frac{\cos \left(\arctan \frac{\sqrt{\frac{k}{m}} v_{0y}}{\sqrt{\frac{n}{m}} g} \right)}{\cos \left(\arctan \frac{\sqrt{\frac{k}{m}} v_{0y}}{\sqrt{\frac{n}{m}} g} - t \frac{\sqrt{kng}}{m} \right)} \quad (4)$$

$$\dot{y}(t) = -\sqrt{\frac{ng}{k}} \tan \left[-\frac{\sqrt{ngk}}{m} t + \arctan \left(\sqrt{\frac{k}{ng}} v_{0y} \right) \right] \quad (5)$$

where:

- f [-] - friction factor according to Fanning [20],
- g [$\text{m}\cdot\text{s}^{-2}$] - gravity,
- h [m] - initial y co-ordinate,
- $k = \frac{f\rho A}{2}$ [$\text{kg}\cdot\text{m}^{-1}$] - friction coefficient,
- m [kg] - particle mass,

n	[kg]	- droplet actual mass (buoyancy),
t	[s]	- time,
v_{0x}, v_{0y}	[m·s ⁻¹]	- initial horizontal and vertical velocity components,
x, y	[m]	- co-ordinates along the horizontal and vertical axes,
\dot{x}, \dot{y}	[m·s ⁻¹]	- velocities along the horizontal and vertical axes,
\ddot{x}, \ddot{y}	[m·s ⁻²]	- accelerations along the horizontal and vertical axes.

Being the model analytical, albeit simplified, it is applicable to a variety of problems but the more reliable results were obtained for high Reynolds numbers. Obviously, as mentioned above, the model presented is one of the possible ones which can describe a single-droplet system from a classic viewpoint: the choice was mainly due to the fact that such model is tightly related to the second law of dynamics, as previously mentioned. To complete the topic, anyway, one may in general face the kinematic analysis of a multi-droplet system (i.e. composed of N droplets) from a classic viewpoint by means of the following analytical expression [21]:

$$m_k \frac{d^2 Q_k(t)}{dt^2} = -\nabla_k V \cdot Q(t) \quad (6)$$

where:

m_k	[kg]	- k -th particle mass ($1 \leq k \leq N$),
Q	[m]	- classic trajectory,
V	[kg·m·s ⁻²]	- potential function accounting for time dependence,
∇_k	[m ⁻¹]	- 3-D gradient operator referred to the k -th particle.

The classical procedure needs a quantitative approach to check how reliable the predictions are. In order to validate the kinematic model just reported, comparisons of field measurements and theoretical values have been already reported in literature [2, 6, 8]. In conclusion the model here defined proves to be kinematically reliable in its predictions from a qualitative and quantitative points of view, particularly when droplets having a “not too small” diameter are considered.

Quantum mechanics for a single particle

The discrepancies between a classic V s. quantum description, on the one hand, and between a single-droplet V s. multi-droplet one, on the other, may be highlighted examining the following expressions for single- and multi-droplet systems (respectively) as compared to those in the previous section of this paper [11, 21]:

$$m \frac{d^2 Q(t)}{dt^2} = F(t) \quad (7)$$

$$m_k \frac{d^2 Q_k(t)}{dt^2} = \nabla_k \left(V \mid V_{qu}^{w_i} \right) Q(t) \quad (8)$$

where:

$$\begin{array}{lll}
 F & [\text{N}] & \text{- force,} \\
 \hbar & [\text{J}\cdot\text{s}] & \text{- the Dirac constant,} \\
 V_{qu}^{\psi_i} = -\sum_{j=1}^N \frac{\hbar^2}{2m_j} \frac{\nabla_j^2 |\psi|}{|\psi|} & [\text{kg}\cdot\text{m}\cdot\text{s}^{-2}] & \text{- quantum potential, } (1 \leq j < k \leq N).
 \end{array}$$

Comparing Eq. (8) with Eq. (6), the first useful consideration is that, if the quantum potential tends to zero, then the quantum and classic kinematic pictures tend to coincide. But as a quantum viewpoint presumes that the “object” evaluated is not just a material particle but also a wave, then for each element of a multi-droplet system one may write the *TDSE* as:

$$D^2 \nabla^2 \psi(\vec{x}, t) - \frac{1}{2} \cdot m \cdot V(\vec{x}, t) \cdot \psi(\vec{x}, t) = -i \cdot D \cdot \left(\frac{\partial}{\partial t} \right) \cdot \psi(\vec{x}, t) \quad (9)$$

With:

$$\psi(\vec{x}, t) = R(\vec{x}, t) \cdot \exp[S(\vec{x}, t)] \quad (10)$$

where:

$$\begin{array}{ll}
 D & [\text{m}^2 \cdot \text{s}^{-1}] \text{ - diffusion coefficient,} \\
 i & [-] \text{ - imaginary unit,} \\
 R & [-] \text{ - wave amplitude,} \\
 S & [\text{rad}] \text{ - wave phase.}
 \end{array}$$

Eq. (9) can be re-written in the form of continuity and Euler-type “quantum fluid-dynamic equations”, respectively [11, 14, 22]:

$$\frac{\partial}{\partial t} \rho(\vec{x}, t) + \nabla[\rho(\vec{x}, t) \cdot \vec{v}(\vec{x}, t)] = 0 \quad (11)$$

$$\frac{\partial}{\partial t} \vec{v}(\vec{x}, t) \equiv \left[\frac{\partial}{\partial t} + \vec{v}(\vec{x}, t) \cdot \nabla \right] \vec{v}(\vec{x}, t) = -\frac{1}{m} \cdot \nabla[V(\vec{x}, t) + Q(\vec{x}, t)] \quad (12)$$

where:

$$\begin{array}{ll}
 \rho & [\text{kg}\cdot\text{m}^{-3}] \text{ - density,} \\
 \vec{v} & [\text{m}\cdot\text{s}^{-1}] \text{ - velocity.}
 \end{array}$$

Eq. (9) can be re-worked by means of Nottale's Scale Relativity theory [12] using a probability density function for a semi-infinite domain [23] for writing the second law of dynamics in the complex field:

$$-\nabla u = m \cdot \frac{\partial}{\partial t} W \quad (13)$$

where:

$$\begin{array}{ll}
 u & [\text{m}^2 \cdot \text{kg} \cdot \text{s}^{-2}] \text{ - scalar potential,} \\
 W & [\text{m}\cdot\text{s}^{-1}] \text{ - complex velocity.}
 \end{array}$$

Dividing the real and imaginary parts in Eq. (13) (U is the imaginary part of W) one gets:

$$\begin{cases} -D \cdot \Delta U - (U \cdot \nabla)U = -\nabla u \\ \frac{\partial}{\partial t} U = 0 \end{cases} \quad (14)$$

which (first equation) may be re-written for a 1-D path as a Riccati equation [24], being c a constant and $y(x)$ an arbitrary function of x :

$$\frac{d}{dx} U(x) = -\frac{m}{\hbar} U^2(x) + \frac{2}{\hbar} \cdot (u(x) - c \cdot m) \quad (15)$$

$$\frac{d^2}{dx^2} y(x) = -\frac{2m}{\hbar^2} \cdot (u(x) - c \cdot m) \cdot y(x) = 0 \quad (16)$$

Both are very powerful tools as they allow for quantum particles computations avoiding the *TDSE*, even if just for 1-D domains, which is useful in particular cases as for instance a droplet vertical downfall.

Quantum mechanics for many-particle systems

Considering multi-droplet systems the *TDSE* needs to be suitably re-written, provided that water has a V-shaped molecule resulting in a magnetic field due to the electric potential between oxygen and hydrogen. This results in [14]:

$$\left[\frac{1}{2} \sum_j \left(-2iD \nabla_j - \vec{K}(\vec{x}_j, t) \right)^2 + \frac{1}{m} V(\vec{x}^N, t) \right] \psi(\vec{x}^N, t) = 2iD \frac{\partial \psi(\vec{x}^N, t)}{\partial t} \quad (17)$$

being the electric potential $V(\vec{x}^N, t)$:

$$V(\vec{x}^N, t) = \sum_{j=1}^N \left[V_o \vec{r}_j - e\Phi(\vec{x}_j, t) \right] + U(\vec{x}^N, t) \quad (18)$$

where:

$\vec{K}(\vec{x}_j, t)$ [$\text{V} \cdot \text{T} \cdot \text{m}^{-3}$] - vector potential for the electromagnetic field,

$\Phi(\vec{x}_j, t)$ [$\text{V} \cdot \text{C}^{-1}$] - external time-dependent scalar potential,

\vec{x}^N [x, y, z] - N -particle coordinates,

e [C] - elementary charge,

\vec{r}_j [m] - location vector,

V_o [$\text{V} \cdot \text{m}^{-1}$] - starting potential

It is now possible to write the continuity equation:

$$\frac{\partial \rho^N(\vec{x}^N, t)}{\partial t} + \sum_{k=1}^N \nabla_k \cdot \vec{j}_k(\vec{x}^N, t) = 0 \quad (19)$$

and the Euler-type equation:

$$\begin{aligned} \frac{\partial \vec{v}_k(\vec{x}^N, t)}{\partial t} + \sum_j (\vec{v}_j(\vec{x}^N, t) \nabla_k) \vec{v}_j(\vec{x}^N, t) + \sum_j (1 - \delta_{jk}) \vec{v}_j(\vec{x}^N, t) \times (\nabla_k \times) \vec{v}_j(\vec{x}^N, t) = \\ = - \left(e \vec{E}(\vec{x}_k, t) + \frac{e}{c} \vec{v}_k(\vec{x}^N, t) \times \vec{B}(\vec{x}_k, t) \right) - \frac{1}{m} \nabla [V_0(\vec{x}^N, t) + U(\vec{x}^N, t) + Q(\vec{x}^N, t)] \end{aligned} \quad (20)$$

where:

$$\begin{aligned} \rho^N(\vec{x}^N, t) &= R^2(\vec{x}^N, t) & [\text{m}^{-3}] & \text{ - } N\text{-particle density,} \\ \vec{j}_k(\vec{x}^N, t) &= \rho^N(\vec{x}^N, t) \vec{v}_k(\vec{x}^N, t) & [\text{m}^{-2} \cdot \text{s}^{-1}] & \text{ - flow-fluid density,} \\ \vec{v}_k(\vec{x}^N, t) &= \frac{\hbar}{m} \nabla_k S(\vec{x}^N, t) - \frac{e}{mc} A(\vec{x}^N, t) & [\text{m} \cdot \text{s}^{-1}] & \text{ - } k\text{-th particle field velocity,} \\ \vec{E}(\vec{x}_k, t) &= -\nabla \Phi(\vec{x}_j, t) - \frac{1}{c} \cdot \frac{\partial A(\vec{x}^N, t)}{\partial t} & [\text{V} \cdot \text{m}^{-1}] & \text{ - external electric field,} \\ \vec{B}(\vec{x}_k, t) &= \text{curl} A(\vec{x}^N, t) & [\text{T}] & \text{ - external magnetic field.} \\ U(\vec{x}^N, t) & & [\text{C}^2 \cdot \text{m}^{-2}] & \text{ - mutual inter-electrical Coulomb repulsion.} \\ C & & [-] & \text{ - numerical coefficient,} \\ A(\vec{x}^N, t) & & [\text{V} \cdot \text{s} \cdot \text{m}^{-1}] & \text{ - vector potential of the classic forces,} \\ S(\vec{x}^N, t) & & [\text{rad}] & \text{ - wave function phase.} \end{aligned}$$

The first integrations of Eq. (19) and Eq. (20) were carried out by Madelung [25], and the work was successively extended by Bohm [26, 27].

Quantum mechanics within a Density Functional Framework (DFF)

The quantum mechanics approach for many-particle systems leads to the continuity (15) and Euler (16) equations in configuration space, thus involving the N-particle density $\rho^N(\vec{x}^N, t)$ with the 3N-D velocity field (corresponding to the k -th particle) given by:

$$\vec{v}_k(\vec{x}^N, t) = \left(\frac{\hbar}{m} \right) \nabla_k S(\vec{x}^N, t) - \left(\frac{e}{mc} \right) \vec{A}(\vec{x}_k, t) \quad (21)$$

The quantum mechanical equations are, however, appealing only if they are in 3-D space in terms of the basic variables $\rho(\vec{x}, t)$ and $\vec{J}(\vec{x}, t)$ and for N-particle systems, as a sprinkler spray flow, to obtain the continuity and Euler equations of quantum mechanics in 3-D space one can resort to the DFF which employs a partitioning of the particle-density and the current-density variables [14]. The DFF provides a single-particle based approach for the description of the motion of many-particle systems in 3-D space. In the context of the DFF, the single particle density and the current density (for the k -th particle trajectory)

are, respectively, given by $R_k^2(\vec{x}^N, t)$ and $\rho_k(\vec{x}, t)\vec{v}_k(\vec{x}, t)$, as explained in the previous chapter, with the corresponding velocity field now expressed as:

$$\vec{v}_k(\vec{x}, t) = \left(\frac{\hbar}{m}\right) \nabla_k S(\vec{x}, t) - \left(\frac{e}{mc}\right) \vec{A}_{eff}(\vec{x}, t) \quad (22)$$

where:

$$\vec{A}_{eff}(\vec{x}, t) \quad [\text{V}\cdot\text{s}\cdot\text{m}^{-1}] \quad - \text{effective classic forces potential.}$$

Within this ground the continuity equation can be written as:

$$\frac{\partial \rho_k(\vec{x}, t)}{\partial t} + \nabla \cdot \vec{j}_k(\vec{x}, t) = 0 \quad (23)$$

and the Euler equation as:

$$\frac{\partial \vec{v}_k(\vec{x}, t)}{\partial t} = -\frac{e}{m} \left[\vec{E}_{eff}(\vec{x}, t) + \frac{1}{c} \vec{v}_k(\vec{x}, t) \times \vec{B}_{eff}(\vec{x}, t) \right] - \frac{1}{m} \nabla [V_{eff}(\vec{x}, t) + Q_k(\vec{x}, t)] \quad (24)$$

where:

$$\vec{E}_{eff}(\vec{x}, t) = -\nabla \Phi(\vec{x}, t) - \frac{1}{c} \frac{\partial}{\partial t} \vec{A}_{eff}(\vec{x}, t) \quad [\text{V}\cdot\text{m}^{-1}] \quad - \text{effective electric field,}$$

$$\vec{B}_{eff}(\vec{x}, t) = \text{curl}(\vec{A}_{eff}(\vec{x}, t)) \quad [\text{T}] \quad - \text{effective magnetic field.}$$

And the quantum potential can be expressed as:

$$Q_k(\vec{x}, t) = \frac{\hbar^2}{2m} \nabla \rho_k(\vec{x}, t) \frac{\nabla \rho_k(\vec{x}, t)}{\rho_k^2(\vec{x}, t)} - \frac{\hbar^2}{4m} \frac{\nabla^2 \rho_k(\vec{x}, t)}{\rho_k(\vec{x}, t)} \quad (25)$$

which is trajectory dependent.

The Euler equation (22) can be recast into the Navier-Stokes equation given by [28]:

$$\frac{\partial \vec{j}_k(\vec{x}, t)}{\partial t} = -\frac{e}{m} \left[\rho_k(\vec{x}, t) \vec{E}_{eff}(\vec{x}, t) + \frac{1}{c} \vec{j}_k(\vec{x}, t) \times \vec{B}_{eff}(\vec{x}, t) \right] - \frac{1}{m} \rho_k(\vec{x}, t) \nabla V_{eff}(\vec{x}, t) + \nabla \vec{T}_k(\vec{x}, t) \quad (26)$$

where $\vec{T}_k(\vec{x}, t)$ represents the stress tensor expressed as:

$$\vec{T}_k(\vec{x}, t) = \left(\frac{\hbar}{2m}\right)^2 \nabla \nabla \rho_k(\vec{x}, t) + \frac{1}{\rho_k(\vec{x}, t)} \left[\vec{j}_k(\vec{x}, t) \vec{j}_k(\vec{x}, t) - \left(\frac{\hbar}{2m}\right)^2 \nabla \rho_k(\vec{x}, t) \rho_k(\vec{x}, t) \right] \quad (27)$$

The stress tensor is due to the contributions of both the quantum potential $\vec{Q}_k(\vec{x}, t)$ and the current density of the k -th particle trajectory. The jet flow is featured as a mixture of N components (particles) and each component, described by Euler equation,

is characterized by common effective electric and magnetic fields, and by a trajectory-dependent quantum force of stress tensor [14].

For many-particle systems, as a sprinkler spray flow, the DFF represents a versatile tool for description of equilibrium as well as dynamical characteristics of the system. The basic picture is that of a multi-component fluid mixture moving in common effective electric and magnetic fields and component-specific quantum potentials.

This approach leads to the concept of quantum trajectory, in analogy to the well-established concept of classical trajectory and can represent an exciting area of research in sprinkler irrigation systems and, more generally, in the agricultural environment.

THE DYNAMICAL AND NUMERICAL APPROXIMATIONS

In any case an analytical “closed form” solution of the equations describing the quantum kinematics of particles is obviously extremely difficult and even the most advanced techniques often fail to achieve such purpose, albeit in the years to come this attempt will not be abandoned. This is why, recently, different forms of approximation have been introduced to treat the “quantum fluid-dynamic equations”: among those, literature reports numerical and dynamical approximations [29], which are both currently being developed. The formers may rely on Eulerian, Lagrangian or Arbitrary Lagrangian-Eulerian descriptions, all characterised by advantages and disadvantages. Lagrangian descriptions are easier in the form through which they write down the equations, as the grid moves with the particle and follows its evolution; but they become difficult to handle as, step after step, the grid becomes non-uniform with problems in the accuracy of the flow solution. Eulerian descriptions are complicate at the beginning of the simulation, due to an increased analytical complication, but prove to be more practical afterwards as the grid does not change with time. A uniform grid following the flow evolution is instead met in the Arbitrary Lagrangian-Eulerian descriptions, also adopted in some computational fluid dynamics codes.

Within each of the three procedures, a given numerical approach can be further subdivided into different algorithms for evaluating derivatives and propagating in time such as the meshless Moving Least Squares (MLS) [29]. The MLS tends to average out any numerical error which may be accumulating in the solution ,helping by this means to stabilize the computational process. The advantages of Mesh based approaches include, also, computational efficiency, higher resolution, accuracy and stability.

The dynamical approximations do not rely in a mathematically-simplified description of the problem but in a physically-simplified one by superimposing some particular conditions (e.g. incompressible flow) or neglecting some other characteristics considered not so relevant to the whole picture. Several approximate methods have been developed in recent years, such as the Linearized Quantum Force (LQF), the Derivative Propagation Method (DPM) and the Vibrational Decoupling Scheme (VDS) [22]. Obviously it would not be inconceivable to imagine a mixed numerical-dynamical approximation approach and we feel that on this aspect research will invest a part of its future resources: in relation to this challenge one should highlight that quantum trajectories can be treated quite similarly to the classic ones when considering, for the particles treated, the suitable relations among the dynamic and the potential part of the problem.

CONCLUSIONS

Remarkable progress has recently been made in the development and application of quantum trajectories as a computational tool for solving the TDSE, which involves the time evolution of the wave function. In the Quantum Theory of Motion (QTM) the complete description of a physical system needs the simultaneous presence of the “wave” and the “particle”.

The wave motion is governed by the TDSE, and the motion of a particle guided by that wave, for a given initial position, is characterized by a velocity defined as the gradient of the phase of the wave function. An assembly of initial positions will constitute an ensemble of particle motions (the so-called quantum trajectories or Bohmian trajectories), guided by the same wave, and the probability of having the particle in a given region of space at a given time is provided by the quantum mechanical TD probability density [30].

A crucial link between QTM and Quantum Fluid Dynamics (QFD) is the quantum potential. In QTM, the particles are under the stress of forces originated from both classical and quantum potentials, while in QFD the fluid motion takes place under the influence of the external classical potential augmented by the quantum potential.

In addition to featuring water droplet ballistics in a sprinkler spray flow, novel quantum trajectory methods are being developed for a broad range of dynamical problems such as mixed classical-quantum dynamics density matrix evaluation in dissipative systems, and electronic non-adiabatic dynamics.

In this context, the present investigation starts from recent hypothesis made by the same Authors of this paper: a water droplet could be treated as a quantum object, characterised both by material particle and by wave properties. Thus the TDSE may be employed to study the process and a parallel classic-quantum description may be achieved, both for single-droplet and for multi-droplet systems. The latter systems are not only affected by the usual fluid-dynamic parameters but the mutual repulsions and attractions between particles are to be accounted for, in the form of electric-magnetic potentials bound to the molecular structure of water: this allows one to re-write the TDSE and the so-called “quantum fluid-dynamic equations” in a novel and more complete form. Future studies will deepen the novel modelling approach suggested to make it more and more suitable for practical applications.

BIBLIOGRAPHY

- [1] Molle, B., Tomas, S., Hendawi, M., Granier, J. 2012. Evaporation and wind drift losses during sprinkler irrigation influenced by droplet size distribution. *Irrigation and Drainage*, 61(2), 240–250.
- [2] Edling, R.J. 1985. Kinetic energy, evaporation and wind drift of droplets from low pressure irrigation nozzles. *Transactions of the ASAE*, 28 (5): 1543 – 1550.
- [3] Keller, J., Bliesner, R.D. 1990. *Sprinkler and Trickle irrigation*. Van Nostrand Reinhold, New York.
- [4] Kincaid, D.C., Longley, T.S. 1989. A water droplet evaporation and temperature model. *Transactions of the ASAE*, 32 (2), 457–463.
- [5] Kinzer, G.D., Gunn, R. 1951. The evaporation, temperature and thermal relaxation-time of freely falling waterdrops. *Journal of Meteorology*, 8(2), 71-83.

- [6] Thompson, A.L., Gilley, J.R., Norman, J.M. 1993. A sprinkler water droplet evaporation and plant canopy model: II. Model applications. *Transactions of the ASAE*, 36 (3), 743-750.
- [7] De Wrachien, D., Lorenzini, G. 2006. Modelling jet flow and losses in sprinkler irrigation: overview and perspective of a new approach. *Biosystems Engineering*, 94 (2), 297-309.
- [8] Lorenzini, G. 2004. Simplified modelling of sprinkler droplet dynamics. *Biosystems Engineering*, 87 (1), 1-11.
- [9] Lorenzini, G. 2006. Water droplet dynamics and evaporation in an irrigation spray, *Transactions of the ASAE*, 49 (2), 545-549.
- [10] Dirac, P.A. 1931. Quantized singularities in the electromagnetic field. *Proceedings of the Royal Society*, A133, 1-60.
- [11] De Wrachien, D., Lorenzini, G., Mambretti, S. 2012. Water droplet trajectories in an irrigation spray: the classic and Quantum Mechanical pictures. *40th International Symposium on Agricultural Engineering*, Opatija (Croatia), 85-96.
- [12] Nottale, L. 1992. The theory of scale relativity. *International Journal of Modern Physics*, 7(20), 4899-4935.
- [13] Goldstein, S., Tumulka, R., Zanghi, N. 2011. Bohmian trajectories as the foundation of quantum mechanics. *Quantum Trajectories (ed. Chattaraj)*, CRC Press, Taylor and Francis Group, 1-15.
- [14] Ghosh, S.K. 2011. Quantum fluid dynamics within the framework of density functional theory. *Quantum Trajectories (ed. Chattaraj)*, CRC Press, Taylor and Francis Group, 183-195.
- [15] Teske, M.E., Hermansky, C.G., Riley, C.M. 1998. Evaporation rates of agricultural spray material at low relative wind speeds. *Atomization and Spray* 8, 471-478.
- [16] Teske, M.E., Thistle, H.W., Eav, B. 1998. New ways to predict aerial spray deposition and drift. *Journal of Forestry*, 96(6), 25-31.
- [17] Teske, M.E., Ice, G.G. 2002. A one-dimensional model for aerial spray assessment in forest streams. *Journal of Forestry*, 100(3), 40-45.
- [18] Hewitt, A.J., Johnson, D.A., Fish, J.D., Hermansky, C.G., Valcore, D.L. 2002. Development of spray drift task force database for aerial applications. *Environmental Toxicology and Chemistry*, 21(3), 648-658.
- [19] Bird, S.L., Perry, S.G., Ray, S.L., Teske, M.E. 2002. Evaluation of the AGDISP aerial spray algorithms in the AgDRIFT model. *Environmental Toxicology and Chemistry*, 21 (3), 672-681.
- [20] Bird, R.B., Steward, W.E., Lighfoot, E.N. 1960. *Transport Phenomena*, Wiley and Sons, New York.
- [21] Lopreore, C.L., Wyatt, R.E. 1999. Quantum wave packet dynamics with trajectories. *Physical Review Letters*, 82, 5190-5193.
- [22] Wyatt, R.E. 2005. Quantum Dynamics with Trajectories. *Introduction to Quantum Dynamics*, Springer, 1-405.
- [23] Hermann, R.P. 1997. Numerical simulation of a quantum particle in a box. *Journal of Physics I: Mathematical and General*, 30(11), 3967-3975.
- [24] Al-Rashid, S.N.T., Habeeb, M.A., Amed, K.A. 2011. Application of the scale relativity (ScR) theory to the problem of a particle in a finite one-dimensional square well (FODSW) potential. *Journal of Quantum Information Science*, 1, 7-17.
- [25] Madelung, E. 1926. Eine anschauliche Deutung der Gleichung von Schroedinger. *Naturwissenschaften*, 14 (45), 1004-1004.
- [26] Bohm, D. 1952. A suggested interpretation of the quantum theory in terms of "hidden variables – I, *Physical Review*, 85 (2), 166-179.

- [27] Bohm, D. 1952. A suggested interpretation of the quantum theory in terms of "hidden variables – II, *Physical Review*, 85 (2), 180–193.
- [28] Holland, P. 2011. Quantum field dynamics from trajectories. *Quantum Trajectories* (ed. Chattaraj). CRC Press, Taylor and Francis Group, 73-86.
- [29] Kendrick, B.K. 2011. Direct numerical solution of the quantum hydrodynamic equation of motion. *Quantum Trajectories* (ed. Chattaraj), CRC Press, Taylor and Francis Group, 325-344.
- [30] Chattaraj, P. K. 2011. *Quantum Trajectories*, CRC Press, London.

ANALIZA KAPLJICA VODE: KLASIČNI I KVANTNI HIDRODINAMIČKI OKVIRI

Daniele De Wrachien¹, Giulio Lorenzini², Stefano Mambretti³, Marco Medici²

¹ *Univerzitet u Milanu, Institut za ekološke i poljoprivredne nauke, Italija*

² *Univerzitet u Parmi, Institut za industrijski inženjering, Italija*

³ *Univerzitet u Kampinasu, Tehnološki fakultet, Brazil*

Sažetak: Konstrukcija sistema za navodnjavanje sa rasprskivačima uvek je praćena potpunim razumevanjem kinematike kretanja kapljica kroz vazduh. Rešavanje ovog problema uključuje, kako teorijska, tako i eksperimentalna razmatranja. Među teorijskim studijama, klasični mehanički pristup, zasnovan na Njutnovim zakonima, daje korisno sredstvo za opis putanja kretanja kapljica vode od rasprskivača do tla. Problem postaje još komplikovaniji kad se ne posmatra samo jedna sama kapljica, već system više kapljica. Pored inter-parametarskih zavisnosti, proučavano je i među-kapljično uzajamno odbijanje, najviše usled električnih interakcija između atoma vodonika i kiseonika iz različitih molekula vode. Alternativa tradicionalnim klasičnim postupcima za analizu dinamike vodenih kapljica pri rasprskivanju, nedavno je ponuđena u obliku kvantnog pristupa. U ovom kontekstu treba proučiti ceo sistem klasičnog i kvantnog pristupa kao i alternative jedno-kapljične i više-kapljične strukture, pa su ovo osnovni ciljevi predstavljenog rada, koji se fokusira na teorijski deo problema, čime naglašava nove perspektive i celovitije obuhvata fenomen toka rasprsnutog spreja. Uopšte, novi pristup vodi do koncepta kvantne putanje u analogiji sa dobro ustanovljenim konceptom klasične trajektorije i dozvoljava da se prerađuje klasične jednačine dinamike fluida u tzv. kvantne jednačine.

Ključne reči: *kinematika čestica spreja, jedno- i više-kapljični sistemi, klasična i kvantna mehanika, kapljice rasprsnute vode, matematičko modeliranje*

Prijavljen: 02.07.2013.
Submitted:
Ispravljen: 17.07.2013.
Revised:
Prihvaćen: 02.08.2013.
Accepted:



MILUROVIĆ KOMERC
Ugrinjevići, Beogradska 32, Tel.: 011/2609-328, Fax: 011/2609-809
www.milurovic-komerc.com e-mail: milurovic@komerc.com

Kubota

DRAGO
PROJEKT

**ITALIJANSKI ČASOVI, KURSEVI
KONVERZACIJA
PRIPREMA ISPITA**

Jovan Jovanović
064 84 23 696
063 84 23 696
www.iltuoinsegnante.net

VebeX

Postojimo zbog Vas
Veleprodaja i distribucija pića

омаадинска зааруга
Г р а д а ц

11070 Нови Београд, Бул. др Зорана Ђинђића 179
ДОМ КУЛТУРЕ - СТУДЕНТСКИ ГРАД
Тел./Факс: 011/2673-244

GIPSKARTON SISTEMI
dipl. ing. Dušan Savić
063 34 89 41
gipssystem@gmail.com

Programni zidovi
Spušteni plafoni
2D crteži
3D animacije

L i n g u a
M u n d i

Agencija za prevodilačke i konsultantske usluge
„LINGVAE MUNDI“
www.lingvaemundi.co.rs
E-mail: office@lingvaemundi.co.rs
lingvaemundi@eunet.rs
Tel. (011) 3240 737, 3342 166, 3342 237
Faks (011) 3228 315
Mobili 063 8043 519

Akademiska izdanja d.o.o.

ZEMUN, Slobodana Bajića 23
tel./faks 011/37-54-079, mob. 063/84-99-101
e-mail: akademiskaizdanja@gmail.com



Vlada Republike Srbije
Ministarstvo prosvete, nauke i
tehnološkog razvoja

Vaša najpouzdanija veza sa svetom!

CIP – Каталогизација у публикацији
Народна библиотека Србије, Београд

631(059)

ПОЉОПРИВРЕДНА техника : научни часопис =
Agricultural engineering : scientific journal / главни и
одговорни уредник Горан Тописировић. – Год. 1, бр. 1
(1963)- . - Београд; Земун : Институт за пољопривредну
технику, 1963- (Београд : Штампарија "Академска
издања") . – 25 cm

Тромесечно. – Прекид у излажењу
од 1987-1997. године

ISSN 0554-5587 = Пољопривредна техника

COBISS.SR-ID 16398594